

**SYNTHESIS AND CHARACTERIZATION OF  
MESOPOROUS NICKEL OXIDE AND NICKEL  
COBALTITE THIN FILMS**

A THESIS SUBMITTED TO  
THE GRADUATE SCHOOL OF ENGINEERING AND SCIENCE  
OF BILKENT UNIVERSITY  
IN PARTIAL FULFILLMENT OF THE REQUIREMENTS FOR  
THE DEGREE OF  
MASTER OF SCIENCE  
IN  
CHEMISTRY

By

Assel Amirzhanova

September, 2019

SYNTHESIS AND CHARACTERIZATION OF MESOPOROUS NICKEL  
OXIDE AND NICKEL COBALTITE THIN FILMS

By Assel Amirzhanova

September, 2019

We certify that we have read this thesis and that in our opinion it is fully adequate, in scope and in quality, as a thesis for the degree of Master of Science.

---

Ömer Dağ (Advisor)

---

Ceyhan Kayran İşçi

---

Ayşen Yılmaz

---

Ferdi Karadaş

---

Burak Ülgüt

Approved for the Graduate School of Engineering and Science:

---

Ezhan Karaşan  
Director of the Graduate School

# ABSTRACT

## SYNTHESIS AND CHARACTERIZATION OF MESOPOROUS NICKEL OXIDE AND NICKEL COBALTITE THIN FILMS

Assel Amirzhanova

M.Sc. in Chemistry

Advisor : Ömer Dağ

September, 2019

In this thesis work, molten-salt assisted self-assembly (MASA) approach was adopted to synthesize mesoporous nickel oxide (m-NiO) and nickel cobaltite (m-NiCo<sub>2</sub>O<sub>4</sub>) thin films. The m-NiO and m-NiCo<sub>2</sub>O<sub>4</sub> films were obtained by coating clear ethanol solutions of nickel salt and two surfactants (charged, CTAB and neutral, 10-lauryl ether), and nickel and cobalt salts with the same surfactants, respectively, followed by calcination at different temperatures (between 250 and 500 °C). The method has been established in a very broad range of salt concentrations in the lyotropic liquid crystalline (LLC) mesophase that can be calcined to produce mesoporous thin films.

Both Ni(II) and Ni(II)/Co(II) systems form stable and oriented LLC mesophases in a broad range of salt concentrations (salt surfactant mole ratio of 2-8) upon evaporation of ethanol from the media. This can be achieved by either spin coating of the clear solutions (this ensure immediate evaporation of ethanol, leaving the LLC gel phase as thin film) or drop casting and evaporation of ethanol (the gelation process takes more time). At higher salt concentrations (10-30 salt/surfactant mole ratios), the mesophase is disordered and leach out salt crystals. However, those compositions can still be used for the synthesis of mesoporous metal oxides, if the samples are calcined immediately after the gelation step. The mesophase is 2D

hexagonal at low salt concentrations and disordered or cubic at higher salt concentrations.

The calcined films were characterized by recording x-ray diffraction (XRD), N<sub>2</sub> adsorption-desorption measurements, imaging (SEM, TEM, and POM) and spectroscopic (UV-Vis, XPS, EDX, and ATR-FTIR) techniques. The N<sub>2</sub> adsorption-desorption isotherms are type IV and characteristic for mesoporous materials. The XRD data show that the crystalline m-NiO and m-NiCo<sub>2</sub>O<sub>4</sub> form at around 300 and 250 °C, respectively, with a pore-wall thickness of around 3-4 nm. The pore-walls grow with increasing the calcination/annealing temperature up to 20 nm at around 500 °C. It accords well with the BET surface area that decreases with increasing calcinations temperature; it is 223 m<sup>2</sup>/g at 300 °C and drops to 20 m<sup>2</sup>/g at 500°C in mesoporous nickel oxide, and 223 m<sup>2</sup>/g at 250 °C and drops to 31 m<sup>2</sup>/g at 500 °C in mesoporous nickel cobaltite. The observed diffraction patterns can be indexed to rock salt cubic structure of NiO and cubic spinel structure of NiCo<sub>2</sub>O<sub>4</sub>. The diffraction lines gradually become sharper indicating crystallization and growth of the pore-walls that accord well with the reduction on the surface area. The m-NiO and m-NiCo<sub>2</sub>O<sub>4</sub> films can be coated over FTO glass to use as an electrochromic electrode (oxidation dark-reduction clear) and electrode for water oxidation reactions (WOR) and WOR, respectively. In nickel oxide case, during cyclic voltammograms cycling, water oxidation process, and electrochromic switching, a few atomic layer of nanocrystalline NiO pore-wall is converted to NiOOH in oxidation and Ni(OH)<sub>2</sub> upon reduction processes; initially formed nanocrystalline NiO (after calcination) pore-walls become NiO coated Ni(OH)<sub>2</sub> (core-shell structure) upon electrochemical treatments. Both NiO and NiCo<sub>2</sub>O<sub>4</sub> having high surface area and electrochemical stability show promising capacitive properties and can be used as electrocatalysts. From the Tafel slope analysis, it has been shown that nickel cobaltite can oxidize water at low overpotentials and therefore can be used as a promising water splitting catalyst.

*Keywords:* mesoporous materials, lyotropic liquid crystal, molten salt assisted self-assembly, soft template, hard template, nickel oxide, nickel cobaltite.

# ÖZET

## MEZOGÖZENEKLİ NİKEL OKSİT VE NİKEL KOBALT OKSİT İNCE FİLMLEİN SENTEZİ VE KARAKTERİZASYONU

Assel Amirzhanova

Kimya, Yüksek Lisans

Tez Danışmanı : Ömer Dağ

Eylül, 2019

Bu tezde, eriyik tuz yardımcı kendiliğinden oluşma (EYKO) metodu uyarlanarak, mezogözenekli nikel oksit (m-NiO) ve nikel kobalt oksit (m-NiCo<sub>2</sub>O<sub>4</sub>) ince film sentezi gerçekleştirilmiştir. m-NiO ve m-NiCo<sub>2</sub>O<sub>4</sub> filmleri, nikel tuzu ve nikel tuzu ve kobalt tuzu karışımının ve iki yüzey aktifin (yükü, CTAB ve nötr C<sub>12</sub>EO<sub>10</sub>) oluşturduğu saydam etanol çözeltilerinin kaplanması ve deęişik sıcaklıklarda (250-500 °C) yakılması ile elde edilmiştir. Bu metot, mezogözenekli ince filmler üretmek amacıyla, geniş bir tuz konsantrasyonu aralığında oluşturulan liyotropik sıvı kristal (LSK) ara fazların yakılmasıyla test edilmiştir.

Her iki sistem de (Ni(II) ve Ni(II)/Co(II)), geniş bir tuz konsantrasyonu aralığında (tuz/yüzey aktif madde mol oranı 2-8), etanolün ortamdan buharlaşmasıyla, kararlı ve düzenli LSK arafazlarını oluşturur. Bu fazlar, hem saydam çözeltilerin döngülü kaplama yöntemi ile (ki bu yöntem etanolün daha hızlı buharlaşmasını ve LSK jel fazının ince film şeklinde oluşmasını sağlar) hem de damlatma yayma yöntemi ile (jelleşme daha uzun zaman alır) elde edilebilir. Daha yüksek tuz konsantrasyonlarında (10-30 tuz/yüzey aktif madde mol oranlarında), arafaz düzensizdir ve tuz kristalleri atımı gözlemlenir. Fakat, eğer örnekler jelleşme aşamasından hemen sonra yakılırsa, bu yüksek tuz oranlı malzemeler mezogözenekli metal oksit üretimi için yine de kullanılabilirler. Arafazlar düşük tuz oranlarında hegzagonal fazda iken yüksek tuz oranlarında düzensiz kübik arafazındadır.

Yakılmış filmler, x-ray difraktometresi (XRD), N<sub>2</sub>-adsorpsiyon- desorpsiyon, görüntüleme (SEM, TEM ve POM) ve spektroskopi (UV-Vis, XPS, EDX, ATR-FTIR) teknikleri ile karakterize edilmiştir. N<sub>2</sub>-adsorpsiyon- desorpsiyon izotermi, tip IV'e aittir ve bu izoterm mezogözenekli malzemeler için karakteristiktir. XRD verileri gösteriyor ki; m-NiO ve m-NiCo<sub>2</sub>O<sub>4</sub> kristalleri, sırasıyla 300 °C ve 250 °C de 3-4 nm gözenek duvar kalınlığıyla oluşur. Gözenek duvarları, yakma sıcaklığının 500 °C'ye çıkmasıyla 20 nm'ye kadar artmaktadır. Bu sonuçlar, sıcaklığın artmasıyla düşen BET yüzey alanı verileri ile uyumludur; m-NiO için 300 °C'de 223 m<sup>2</sup>/g olan yüzey alanı 500 °C'ye gelindiğinde 20 m<sup>2</sup>/g'a kadar düşerken, m-NiCo<sub>2</sub>O<sub>4</sub> de 300 °C'de 223 m<sup>2</sup>/g olan yüzey alanı 500 °C'ye gelindiğinde 31 m<sup>2</sup>/g'a düşer. Gözlenen difraksiyon grafikleri, NiO için NaCl kübik yapısına ve NiCo<sub>2</sub>O<sub>4</sub> için kübik spinel yapısına indekslenmiştir. Difraksiyonların daha keskin hale gelmesi, kristallenme ve gözenek duvarının büyümesini ve dolayısıyla yüzey alanının küçülmesini göstermektedir.

m-NiO ve m-NiCo<sub>2</sub>O<sub>4</sub> filmleri elektrokromik ve su oksidasyon elektrotları olarak kullanılmak için FTO cam alttaşlar üzerine de kaplanmıştır. NiO malzemesi, dönüşümlü voltamogram, su oksidasyon prosesi ve elektrokromik dönüşümü boyunca, nanokristal NiO gözenek duvarlarının sadece birkaç atomik katmanı yükseltgenme sırasında NiOOH'e ve indirgenme sırasında ise Ni(OH)<sub>2</sub> dönüşmektedir; böylece elektrokimyasal işlem sonucunda başlangıçta saf NiO olan malzeme Ni(OH)<sub>2</sub> kaplı NiO (çekirdek-katman yapısı) formuna dönüşür. Yüksek yüzey alanı ve elektrokimyasal kararlılığa sahip olan ve kapasitif özelliği umut vadeden NiO ve NiCo<sub>2</sub>O<sub>4</sub>, elektrokatalizör olarak kullanılmıştır. Tafel eğrisi analizi ile nikel kobalt oksitler düşük ek potansiyellerde suyu okside edebileceği görülmüştür ve bu malzeme suyu oksijene ve hidrojene ayırma işleminde umut vadeden bir elektrokatalizördür.

*Anahtar kelimeler:* mezogözenekli malzeme, liyotropik sıvı kristal, eriyik tuz yardımcı kendiliğinden oluşma, yumuşak taslak yöntemi, sert taslak yöntemi, nikel oksit, nikel kobalt oksit.

# Acknowledgement

First of all, I would like to express my gratitude and respect to my supervisor professor Ömer Dağ for always being supportive, helpful and patient during my research. I am very thankful for the amount of knowledge and experience that I've got during my studies. His encouragement and support helped me to overcome difficulties that I faced in my research and courses work.

Also, I would like to acknowledge former members of Dag research group: Doruk Ergöçmen, for being incredibly helpful and loyal to me in the beginning of my study when I didn't have any experience in the research; Muamer Yusuf Yaman, for his kindness and friendship, Tuluhan Olçayto Çolak for teaching me things that I would never think I learn.

I would like to mention my friends Isil Uzunok and Irmak Karakaya, that in these two years became more than just lab colleagues to me. My deep gratitude also goes to Ezgi Yılmaz-Topuzlu, Nüveyre Canbolat, Nesibe Akmanşen, Mete Turgut, Guvanch Gurbandurdyev and Isik Tunçay for their help and making lab environment friendly and warm. I would like to acknowledge Irmak Karakaya, Can Berk Uzundal and Gözde Karaoğlu for helping me with electrochromism experiments.

My life in Bilkent would not be full of joy and happiness without my friends Koray Yavuz, Ulviyya Guliyeva, Eliza Sopubekova, Youssef Tekriti, Mehdi Ramezani and Mohammad Fathi.

I am incredibly thankful for my best friends in Kazakhstan: Dinara Alikhanova, Nazerke Ualiveva and Kuandyk Klimenov, that are miles apart from me but still I feel their support and friendship.

Finally yet importantly, I am grateful for my beloved mother Karlygash Kalguzhina, father Amangeldy Kalguzhin, uncle Yestay Kalguzhin and my siblings Amira, Amina for their love and precious support in any my decision. Separately, I want to thank my best friend, twin and soul sister Assem, for being such an inspiration and role model for me, without whose support I would not be here.

*"so, here you are  
too foreign for home  
too foreign for here.  
never enough for both."*

*~Ijeoma Umebinyuo, "Diaspora Blues"*

# Contents

1.	INTRODUCTION .....	1
1.1.	General methods of synthesis of mesoporous metal oxides.....	1
1.2.	Synthesis of mesoporous metal oxides using soft templates .....	2
1.3.	Synthesis of mesoporous metal oxides using hard templating method .....	4
1.4.	Lyotropic liquid crystal templating (SLCT) and Molten Salt Assisted Self Assembly (MASA) .....	6
1.5.	Mesoporous Nickel Oxide and Nickel Oxide Nanoparticles. ....	11
1.6.	Mesoporous Nickel Cobaltite and Nickel Cobaltite Nanoparticles .....	13
2.	EXPERIMENTAL PROCEDURE .....	16
2.1.	Materials.....	16
2.2.	Preparation of Ni(II) Solutions .....	16
2.3.	Preparation of Mesoporous NiO Films .....	17
2.4.	Preparation of Ni(II) and Co(II) Mixed Solutions .....	18
2.5.	Synthesis of Mesoporous NiCo <sub>2</sub> O <sub>4</sub> Films .....	19
2.6.	Preparation of the Electrodes and Electrochemistry Setup .....	20
2.7.	Instrumentation .....	22
2.7.1.	Powder x-Ray Diffraction (PXRD) .....	22
2.7.2.	Polarized Optical Microscopy (POM) .....	22
2.7.3.	N <sub>2</sub> Adsorption Desorption Measurements .....	22
2.7.4.	Scanning Electron Microscopy (SEM) .....	22

2.7.5.	Transmission Electron Microscopy (TEM) .....	22
2.7.6.	UV-vis Absorption Spectroscopy .....	23
2.7.7.	X-ray Photoelectron Spectroscopy (XPS) .....	23
3.	RESULTS AND DISCUSSION .....	24
3.1.	Freshly Prepared Ni(II)/C <sub>12</sub> E <sub>10</sub> Film Characterization .....	24
3.2.	Optimization of Coating Method .....	27
3.3.	Optimization of Salt to Surfactant Ratio .....	29
3.4.	Optimization of Calcination Temperature .....	36
3.5.	Stability of Ni(II)/C <sub>12</sub> E <sub>10</sub> Solutions .....	44
3.6.	Electrochemical Characterization of Mesoporous Nickel Oxide .	47
3.7.	Capacitance of Nickel Oxide Thin Films and Effect of Calcination Temperature .....	56
3.8.	Characterization of Nickel Hydroxide .....	56
3.9.	Optical Properties of Nickel Oxide Thin Films .....	58
3.10.	Electrochromic Behavior of Mesoporous Nickel Oxide Thin Film .....	60
3.11.	Freshly Prepared (Ni(II)+Co(II))/C <sub>12</sub> E <sub>10</sub> Film Characterization. .	62
3.12.	Optimization of Salt to Surfactant Ratio .....	64
3.13.	Optimization of Calcination Temperature .....	68
3.14.	Electrochemical Characterization of NiCo <sub>2</sub> O <sub>4</sub> Thin Films .....	72
4.	CONCLUSION .....	77
5.	FUTURE WORK .....	79
5.1	Synthesis and Characterization of Mesoporous Nickel Oxide on Silica Template .....	79
	BIBLIOGRAPHY .....	83

# List of figures

Figure 1. Schematics representation of EISA method. ....	3
Figure 2. Synthesis route for the hard templating to produce porous mesostructures. 5	
Figure 3. Illustration of orientational order in solids, liquid crystals and liquids. ....	7
Figure 4. Photographs and schematic representations of the preparation of Ni(II) solutions and calcination products. ....	18
Figure 5. Photographs of the clear solutions with varying Ni(II)/C <sub>12</sub> E <sub>10</sub> mole ratios, as shown on the vials. ....	18
Figure 6. Photographs and schematic representations of the preparation of the Co(II) and Ni(II) mixed solutions and calcination products. ....	20
Figure 7. Photographs of the freshly prepared mesoporous nickel oxide electrodes on the FTO glass. ....	21
Figure 8. Electrochemical cell and components in a 1 M KOH solution. ....	21
Figure 9. XRD patterns of #Ni(II)/C <sub>12</sub> E <sub>10</sub> , where the # is (a) 2 and (b) 4 over time, immediately after coating, 1 hr, and 8 hrs. Insets are POM images of 1-day aged samples. ....	24
Figure 10. XRD patterns of #Ni(II)/C <sub>12</sub> E <sub>10</sub> , where the # is (a) 6 and (b) 8 over time, immediately after coating and 1 week of aging. The insets are POM images of 1-week aged samples. ....	25
Figure 11. XRD patterns of #Ni(II)/C <sub>12</sub> E <sub>10</sub> , where the # is (a) 10 and (b) 12 over time, immediately after coating, 5, 10, 15 and 20 minutes. Insets are POM images of 1-hour aged samples. ....	26
Figure 12. XRD patterns of #Ni(II)/C <sub>12</sub> E <sub>10</sub> , where the # is (a) 15, (b) 20 (c) 25, and (d) 30 over time, immediately after coating, 5, 10, and 20 minutes. ....	27

Figure 13. SEM images of (left) thin film and (right) drop-cast film of m-NiO. ....	28
Figure 14. XRD patterns of the calcined samples of spin coated (bottom) and drop casted (top) m-NiO at 300 °C.....	29
Figure 15. Photos of the clear solutions at various concentrations and corresponding thin films obtained after calcination at 300°C starting from 2 to 30 salt/surfactant mole ratio (left to right).....	30
Figure 16. XRD patterns (top to bottom) of m-NiO-#-300, where # is (a) 2, 4, 6, and 8 and (b) 10, 12, 15, 20, 25, and 30.....	31
Figure 17. SEM images of (left) m-Ni(OH) <sub>2</sub> -2-300 and (right) m-NiO-15-300.....	32
Figure 18. XRD patterns of the calcined samples at 350°C (bottom to top) m-NiO-2, m-NiO-4, m-NiO-6, and m-NiO-8. ....	33
Figure 19. (a) N <sub>2</sub> (77 K) adsorption desorption isotherms of m-NiO-2-350, m-NiO-4-350, m-NiO-6-350, m-NiO-8-350, and m-NiO-10-300 and (b) pore size distribution plots (obtained from the desorption branches) of m-NiO-2-350, m-NiO-4-350, m-NiO-6-350, m-NiO-8-350, and m-NiO-10-300. ....	34
Figure 20. (a) N <sub>2</sub> (77 K) adsorption desorption isotherms of m-NiO-12-300, m-NiO-15-300, m-NiO-20-300, m-NiO-25-300, and m-NiO-30-300 and (b) pore size distribution plots (obtained from the desorption branches) of m-NiO-12-300, m-NiO-15-300, m-NiO-20-300, m-NiO-25-300, and m-NiO-30-300.....	35
Figure 21. Photos of the m-NiO-10 thin films obtained after calcination at different temperatures starting from 250 to 500°C (left to right).....	37
Figure 22. XRD patterns of the m-Ni-10-250, m-NiO-10-300, m-NiO-10-350, m-NiO-10-400, m-NiO-10-450, and m-NiO-10-500, bottom to top.....	38
Figure 23. (a) N <sub>2</sub> (77 K) adsorption desorption isotherms and (b) pore size distribution of (I) m-NiO-10-300, (II) m-NiO-10-350, (III) m-NiO-10-400, (IV) m-NiO-10-450, and (V) m-NiO-10-500.....	40

Figure 24. Correlation of BET surface area and particle size: (a) surface area change with temperature and (b) particle size change with temperature. ....	41
Figure 25. SEM images of m-Ni-10-250 at different magnifications, scale bars are (left) 40 $\mu\text{m}$ and (right) 20 $\mu\text{m}$ . ....	42
Figure 26. SEM images of m-NiO-10-300 at different magnifications, scale bars are (a) 40 $\mu\text{m}$ , (b) 5 $\mu\text{m}$ and (c) 2 $\mu\text{m}$ . ....	42
Figure 27. SEM images of (a) m-NiO-10-350 (scale bar is 20 $\mu\text{m}$ ), (b) m-NiO-10-350 (scale bar is 500 nm), (c) m-NiO-10-400 (scale bar is 10 $\mu\text{m}$ ), (d) m-NiO-10-400 (scale bar is 500 nm), (e) m-NiO-10-450 (scale bar is 20 $\mu\text{m}$ ), (f) m-NiO-10-450 (scale bar is 500 nm), (g) m-NiO-10-500 (scale bar is 40 $\mu\text{m}$ ), and (h) m-NiO-10-500 (scale bar is 500 nm). ....	43
Figure 28. TEM images of (a) m-NiO-10-300 (scale bar is 50 nm), (b) m-NiO-10-300 (scale bar is 10 nm), (c) m-NiO-10-400 (scale bar is 50 nm), (d) m-NiO-10-400 (scale bar is 10 nm), (e) m-NiO-10-500 (scale bar is 50 nm), and (f) m-NiO-10-500 (scale bar is 5 nm). ....	44
Figure 29. XRD patterns of the m-NiO-10-300 from (a) aged gel and (b) aged solution. ....	45
Figure 30. (a) $\text{N}_2(77\text{ K})$ adsorption desorption isotherms and (b) pore size distribution of m-NiO-10-300 from aged mesophase and m-NiO-10-300 from aged solution. ....	46
Figure 31. (a) 2 <sup>nd</sup> CV and (b) 600 <sup>th</sup> CV of m-NiO-10 electrodes calcined at (I) 300, (II) 350, (III) 400, (IV) 450 and (V) 500 $^\circ\text{C}$ . ....	48
Figure 32. Overall change in peak current at around 0.6 V over cycling of electrodes prepared at (I) 300, (II) 350, (III) 400, (IV) 450 and (V) 500 $^\circ\text{C}$ . ....	49
Figure 33. CVs of the m-NiO-10-400 (I) 1 <sup>st</sup> and (II) 50 <sup>th</sup> , and (III) 1 <sup>st</sup> cycle after recalcination of (II). ....	51

Figure 34. CV of Ni(OH) <sub>2</sub> prepared at 250 °C.....	52
Figure 35. Schematic representation of the mesoporous NiO before and after oxidation-reduction cycles with surface composition: (I) NiO surface before cycling, (II) NiO with NiOOH on the surface (black color), (III) NiO with Ni(OH) <sub>2</sub> on the surface (green color), (I) Schematic representation of electrochemical cell with NiO electrode before and after CV. ....	53
Figure 36. 220 XRD line of m-NiO-10-400 (I) before and (II) after 1000 CVs.....	54
Figure 37. XPS spectra of m-NiO (a) before and (b) after CV (1000 cycle).....	55
Figure 38. XRD patterns of (I) α-Ni(OH) <sub>2</sub> just after calcination at 250 °C, and (II) β-Ni(OH) <sub>2</sub> after aging (I) in base for 10 minutes.....	57
Figure 39. Photos of m-NiO thin films obtained at 300 °C(I) right after calcination, (II) after oxidation cycle, (III) after reduction cycle. ....	58
Figure 40. UV-Vis spectra of m-NiO calcined at 300 °C, (I) fresh sample, (II) the same sample treated with NaBH <sub>4</sub> solution and (II) to (III) washed and aged under ambient condition for bottom to top 5, 10, 25, 45, 60, and 300 min.....	59
Figure 41. Electrochromic behavior of (I) m-10-NiO-300, (II) m-10-NiO-400, (III) m-10-NiO-500, absorbance versus time plot of voltage intervals of -400 to 600 mV at different wavelength of 585 nm (black), and 886 nm (red). ....	60
Figure 42. Electrochromic behavior of m-NiO-10-300, absorbance versus normalized time plot of voltage intervals of (I) -500 to 500 mV, (II) -500 to 400mV, (III) -500 to 345mV, (IV) -500 to 150 mV. And (V) 150 to 500 mV.....	62
Figure 43. XRD patterns of (a) 6(Ni(II)+Co(II))/C <sub>12</sub> E <sub>10</sub> mole ratio mesophase over time, immediately after coating, 10 and 30 minutes and (b) 25(Ni(II)+Co(II))/C <sub>12</sub> E <sub>10</sub> mole ratio mesophase immediately after coating, 5 and 15 minutes. Insets are POM images of (a) fresh (b) 15 minutes aged samples.....	63

Figure 44. XRD patterns (bottom to top) of m-NiCo <sub>2</sub> O <sub>4</sub> -#-250, where # is 6, 8, 10, 12, 15, 20, and 25.....	65
Figure 45. SEM images of (a) m-NiCo <sub>2</sub> O <sub>4</sub> -6, (b) m-NiCo <sub>2</sub> O <sub>4</sub> -15 (c) and m-NiCo <sub>2</sub> O <sub>4</sub> -25, scale bars are 10 μm.....	66
Figure 46. N <sub>2</sub> (77 K) adsorption desorption isotherms of (a) m-NiCo <sub>2</sub> O <sub>4</sub> -6-250, m-NiCo <sub>2</sub> O <sub>4</sub> -8-250, and m-NiCo <sub>2</sub> O <sub>4</sub> -10-250 and (b) m-NiCo <sub>2</sub> O <sub>4</sub> -12-250, m-NiCo <sub>2</sub> O <sub>4</sub> -15-250, m-NiCo <sub>2</sub> O <sub>4</sub> -20-250, and m-NiCo <sub>2</sub> O <sub>4</sub> -25-250, and pore size distribution plots (obtained from the desorption branches) of (c) m-NiCo <sub>2</sub> O <sub>4</sub> -6-250, m-NiCo <sub>2</sub> O <sub>4</sub> -8-250, and m-NiCo <sub>2</sub> O <sub>4</sub> -10-250 and (d) m-NiCo <sub>2</sub> O <sub>4</sub> -12-250, m-NiCo <sub>2</sub> O <sub>4</sub> -15-250, m-NiCo <sub>2</sub> O <sub>4</sub> -20-250, and m-NiCo <sub>2</sub> O <sub>4</sub> -25-250.....	67
Figure 47. XRD patterns (subtracted background) of the m-NiCo <sub>2</sub> O <sub>4</sub> -10-250, m-NiCo <sub>2</sub> O <sub>4</sub> -10-300, m-NiCo <sub>2</sub> O <sub>4</sub> -10-350, m-NiCo <sub>2</sub> O <sub>4</sub> -10-400, m-NiCo <sub>2</sub> O <sub>4</sub> -10-450, and m-NiCo <sub>2</sub> O <sub>4</sub> -10-500 (bottom to top). ....	69
Figure 48. (a) N <sub>2</sub> (77 K) adsorption desorption isotherms and (b) pore size distribution of (I) m-NiCo <sub>2</sub> O <sub>4</sub> -10-250, (II) m-NiCo <sub>2</sub> O <sub>4</sub> -10-300, (III) m-NiCo <sub>2</sub> O <sub>4</sub> -10-350, (IV) m-NiCo <sub>2</sub> O <sub>4</sub> -10-400, (V) m-NiCo <sub>2</sub> O <sub>4</sub> -10-450, and (VI) m-NiCo <sub>2</sub> O <sub>4</sub> -10-500. ....	70
Figure 49. SEM images of (a) m-NiCo <sub>2</sub> O <sub>4</sub> -10-250 at 5 μm, (b) m-NiCo <sub>2</sub> O <sub>4</sub> -10-250 at 1 μm; (c) m-NiCo <sub>2</sub> O <sub>4</sub> -10-350 at 5 μm, (d) m-NiCo <sub>2</sub> O <sub>4</sub> -10-350 at 1 μm; (e) m-NiCo <sub>2</sub> O <sub>4</sub> -10-450 at 5 μm, (f) m-NiCo <sub>2</sub> O <sub>4</sub> -10-450 at 1 μm.....	72
Figure 50. 5 <sup>th</sup> CV of m-NiCo <sub>2</sub> O <sub>4</sub> -10 electrodes calcined at 250, 300, 350, 400, 450, and 500 °C.....	73
Figure 51. Tafel slope of m-NiCo <sub>2</sub> O <sub>4</sub> -10 electrodes, calcined at 250, 300, 350, 400, 450, and 500 °C.....	74
Figure 52. (a) (I) 5 <sup>th</sup> and (II) 100 <sup>th</sup> CVs of m-NiCo <sub>2</sub> O <sub>4</sub> -10-250; (b) (I) 5 <sup>th</sup> and (II) 100 <sup>th</sup> CVs of m-NiCo <sub>2</sub> O <sub>4</sub> -10-350 electrodes. (c) Tafel slopes of m-NiCo <sub>2</sub> O <sub>4</sub> -10 electrodes calcined at 250 and 350 °C after 100 cycles. ....	75

Figure 53. XRD pattern of m-NiO on silica template at 450 °C.....	80
Figure 54. (a) N <sub>2</sub> (77 K) adsorption-desorption isotherms and (b) pore size distribution of m-NiO on silica at 450 °C. ....	81
Figure 55. SEM images of (a) m-NiO-350 (scale bar is 10 μm) and (b) m-NiO/SiO <sub>2</sub> -350 (scale bar is 500 nm). ....	81

# List of Tables

Table 1. Composition of the clear solutions used for the preparations of mesoporous NiO films.....	17
Table 2. Composition of the clear solutions used for the preparations of mesoporous NiCo <sub>2</sub> O <sub>4</sub> films. ....	19
Table 3. N <sub>2</sub> (77K) adsorption-desorption data of m-NiO-#-XXX samples (# is Ni/C <sub>12</sub> E <sub>10</sub> mole ratio and XXX is calcination/annealing temperature in Celsius). ....	36
Table 4. Particle size of m-NiO-#-XXX samples (XXX is calcination/annealing temperature in Celsius). ....	39
Table 5. N <sub>2</sub> (77K) adsorption-desorption data of m-NiO-#-XXX samples (XXX is calcination/annealing temperature in Celsius). ....	39
Table 6. N <sub>2</sub> (77K) adsorption-desorption data of m-NiO-10-300 from aged mesophase and aged solution.....	47
Table 7. Temperature dependent capacitance of m-NiO-10-XXX electrodes, where XXX calcination temperature. ....	56
Table 8. N <sub>2</sub> (77K) adsorption-desorption data of m-NiCo <sub>2</sub> O <sub>4</sub> --XXX samples (# is Ni+Co/C <sub>12</sub> E <sub>10</sub> mole ratio and XXX is calcination/annealing temperature in Celsius). ...	68
Table 9. N <sub>2</sub> (77K) adsorption-desorption data of m-NiCo <sub>2</sub> O <sub>4</sub> -10-XXX samples (XXX is calcination/annealing temperature in Celsius).....	71
Table 10. Composition of the clear solutions used for the preparations of mesoporous NiO/SiO <sub>2</sub> films.....	79

# List of Abbreviations

LC	: Liquid Crystal
LLC	: Lyotropic Liquid Crystal
EISA	: Evaporation Induced Self Assembly
MASA	: Molten salt Assisted Self Assembly
XRD	: X-ray Diffraction
POM	: Polarized Optical Microscopy
SEM	: Scanning Electron Microscopy
TEM	: Transmission Electron Microscopy
XPS	: X-ray Photoelectron Spectroscopy
BET	: Brunauer, Emmett and Teller
JCPDS	: Joint Committee on Powder Diffraction Standards
PDF	: Powder Diffraction File
WE	: Working Electrode
RE	: Reference Electrode
CE	: Counter Electrode
FTO	: Fluorine doped Tin Oxide
NHE	: Normal Hydrogen Electrode
CV	: Cyclic Voltammetry

# CHAPTER 1

## 1.INTRODUCTION

### 1.1.General methods of synthesis of mesoporous metal oxides

A lot of attention has been devoted on porous inorganic materials towards controlling their pore sizes, pore's architecture and various applications, like catalysis, drug delivery, energy storage etc. [1]. Mesoporous materials are the inorganic materials that have pore sizes between 2 and to 50 nm[2]. Kresge et al. discovered M41S family of mesoporous silica for the first time[3]. Presence of pores, channels and cavities provide these materials high surface area and applicability in various fields[1]. By playing with the composition and pH of the synthesis media, different structures of mesoporous silica have been fabricated: hexagonal, cubic and lamellar. A charged cationic surfactant, cetyltrimethyl ammonium bromide (CTAB), and tetraethylorthosilicate (TEOS) were used. The pore size has been controlled between 2 and 5 nm with a typical surface area of around 1000 m<sup>2</sup>/g[3][4].

Another method for the synthesis of mesoporous silica molecular sieves, using a different nonionic surfactants (pluronics, EO<sub>n</sub>PO<sub>m</sub>EO<sub>n</sub>, where EO is ethylene oxide and PO is propylene oxide), was discovered by Bagshaw et al.[5]. Resulted mesoporous silica had disordered channel structures with uniform pores ranging from 2.0 to 5.8 nm[5]. It was one of the first attempts to use liquid crystalline templating to synthesize mesoporous silica[5][6].

However, the mesoporous silica materials have their own limitations. They are not chemically active and pore walls are amorphous which limit their applications[7]. So there was a need to produce non-silica mesoporous materials, namely mesoporous transition metal oxides, which might have wider applications[8].

So later, the method was expanded for synthesis of metal oxides and mixed metal oxides, such as  $\text{TiO}_2$ ,  $\text{ZrO}_2$ ,  $\text{Ta}_2\text{O}_5$ ,  $\text{SiAlO}_3$ ,  $\text{SiTiO}_4$  [9]. This was the first example of using P123 ( $\text{EO}_{20}\text{PO}_{70}\text{EO}_{20}$ ) as a template. Corresponding metal alkoxides ( $\text{M}(\text{OR})_4$ ) were used as the metal precursors. The resulted mesoporous metal oxides had high surface area with large pores. Later, this process was adopted to carry in a non-aqueous media, since the presence of water makes the hydrolysis and condensation of these precursors much faster that makes the metal oxide particle large and difficult to assemble with surfactant/micelles. As a result, mesoporous solids with large pores and thick walls have been synthesized. These studies opened paths for future possibilities for the synthesis of other mesoporous metal oxides and sulfides [10].

Another well-known method to produce mesoporous transition metal oxide is thermal decomposition of an oxalate precursor. Variety of metal oxides, such as  $\text{Fe}_2\text{O}_3$ ,  $\text{CoFe}_2\text{O}_4$ ,  $\text{NiFe}_2\text{O}_4$ ,  $\text{Mn}_x\text{O}_y$ , and  $\text{NiO}$  were fabricated by simply calcining corresponding metal oxalate crystal to obtain mesoporous transition metal oxide[11]. This method is quite popular as it is environmentally friendly and has a low cost[11]. However, the pores of these materials are non-uniform in shape and size that may limit their applications.

Everything so far mentioned above was the first and general attempts to synthesis mesoporous materials and metal oxides. Generally, there are two main synthesis pathways to produce ordered mesoporous materials, soft templating and hard templating. The pros and cons of both and recent synthesis methods will be explicitly reviewed in the following chapters.

## **1.2. Synthesis of mesoporous metal oxides using soft templates**

Soft templating method of synthesis mesoporous metal oxides is one of the earliest attempts to fabricate mesoporous materials. Mostly, cationic or anionic surfactants were used like alkyltrimethylammonium halides and  $\text{C}_{16}\text{H}_{33}\text{SO}_3\text{Na}$ [10],[11]. The major drawback of this method is that the structure of the porous material is not stable to calcination.

Many metal oxides, like  $\text{TiO}_2$  and  $\text{Nb}_2\text{O}_5$ , have been successfully synthesized by soft templating route and the surfactant was removed by calcination. In addition to above methods, ligand assisted method has also been used for the synthesis of mesoporous

metal oxides[13][14][8]. Hexagonal  $\text{TiO}_2$  was first mesoporous transition metal oxide that has been synthesized by using sol gel method. A mixture of titanium alkoxide and phosphate surfactants was used as a precursor solution, and acetylacetone was used for hydrolysis of titanium alkoxide[14][8]. Later that method was called ligand-assisted method, and was applied to produce mesoporous oxides like tantalum pentoxide and zirconium dioxide[15][16].

Ordered semicrystalline mesoporous metal oxides were also fabricated by using soft templating method, namely evaporation induced self-assembly (EISA) process [17]. The EISA method allows production of ordered mesoporous transition metal oxides films and powders. Initial stage of the EISA process is a self-assembly process of surfactant and inorganic ingredients into an ordered mesostructures. The self-assembly means self-organization of materials through different types of interactions like Vander Waals forces, hydrogen bonding etc.[17]. In that process, organic surfactants molecules, such as poly(ethylene oxide)-b-polystyrene copolymer, that have hydrophobic and hydrophilic ends and assemble into micelles in solvent media (water, ethanol or another polar solvent)[18]. These micelles possess different structures like spherical or cylindrical. For shape of the micelles, concentration of the surfactant is very critical, as, once particular concentration of micelles in the precursor solution is reached, micelles, upon evaporation of solvent, self-assemble into different types of mesophases, like hexagonal, lamellar or cubic. By playing with concentration of inorganic precursor and organic surfactant, different types of mesophases could be obtained[17]. Evaporation of solvent can be achieved by spin coating, drop casting, dip coating or spray coating[6], [19]–[22],

The schematics of EISA process is represented in the Figure 1.

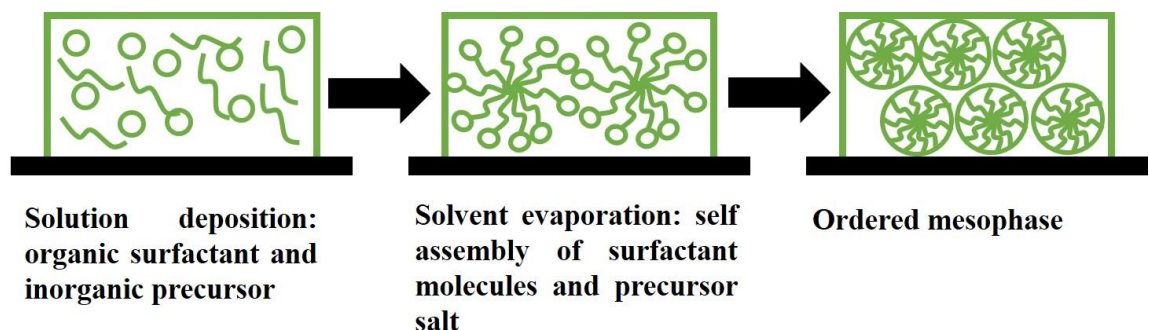


**Figure 1.** Schematics representation of EISA method.

Many mesoporous metal oxides like  $\text{TiO}_2$ ,  $\text{Al}_2\text{O}_3$ ,  $\text{SnO}_2$ ,  $\text{WO}_3$ ,  $\text{HfO}_2$ ,  $\text{SiAlO}_y$ , and  $\text{ZrTiO}_y$  were synthesized via EISA method using poly(alkylene oxide) block copolymers as template[9], [10]. However, the EISA pathway has some limitations, as it is hard to control condensation process because some metal precursors are too reactive and obtained material is not mesoporous. Usually, for many transition metal salts, the hydrolysis and condensation processes are very slow that also makes it hard to use EISA method. The surface area of these metal oxides, produced from this method, is not always high enough that limits their applicability [23][24].

To sum up, the advantage of soft templating is that the templates are not expensive and commercially available. The pore sizes, pore-walls-thickness, -crystallinity, and -composition, and surface area can be easily controlled, as they depend on the nature of the used template and its chemical composition. However, mostly the synthesis in the sol gel process proceeds through hydrolysis and condensation reaction and it is sometimes difficult to control the synthesis steps that may require high temperature treatments. The reaction temperature and humidity could be an issue to assemble the growing inorganic units into mesostructures, especially in the synthesis of transition metal oxides[8]. In those cases, a hard-templating method may be more advantages.

### **1.3.Synthesis of mesoporous metal oxides using hard templating method**

Large variety of highly ordered mesoporous materials were fabricated using hard templating method, also known as nano-casting[25], [26]. In soft templating method, the self-assembly of surfactant molecules played critical role, in nano-casting, precursor solution just replicates the shape of the mesoporous template. In this method, the hard template e.g. mesoporous silica or carbon, is pre-synthesized. Then the inorganic precursor solution is infiltrated into the mesoporous structure of the template. After that, the material is calcined and washed to remove the hard template to obtain the desired mesoporous material[27].

The schematics of the hard templating method is provided in the Figure 2[28].

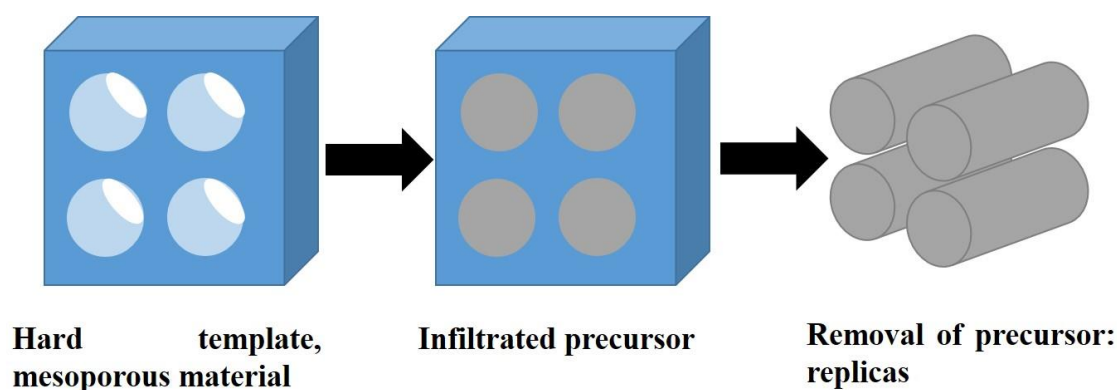


**Figure 2.** Synthesis route for the hard templating to produce porous mesostructures.

One of the first templates used was mesoporous aluminum oxide prepared by anodic oxidation[29]. Packed nanowires of metals have been produced in the pores of around 100 nm. This opened a room to fabrication of other nanomaterials[29]. Later, the method was applied to synthesize mesoporous carbon CMK-1 by using mesoporous silica as the hard template[27]. It was the first example of ordered mesoporous carbon synthesized using hard templating. That carbon possessed uniform pore size distribution with pore size of 3 nm[27]. Removal of the silica template is done by etching it with NaOH or HF solutions, which resulted mesoporous carbon replicates of the structure of the template[8]. However, the synthesized nanowires are always connected with small channels as all hard templates have some disordered pores to make sure that replicated nanoarrays are connected with each other to have a stable structure[8][30].

Che et al. fabricated the first mesoporous transition metal oxides using hard template mesoporous silica, SBA-15[31][32]. Chromium oxide nanowires were obtained by infiltration of  $K_2Cr_2O_7$  into a mesoporous silica template that was removed by HF solution. The obtained oxide had an ordered three dimensional structure with pore size of 3.4 nm[32]. Later same group synthesized ordered three dimensional hexagonal mesoporous tungsten oxide using the same template and method[33].

Another hard template is mesoporous carbon aerogel to make mesoporous metal oxide that was introduced by Li et al. in 2004. The precursor solution is usually made up of a magnesium nitrate salt. Incorporation of metal ions species, followed by a calcination at 600 °C produces mesoporous magnesium oxide with a 3D pore structure and a surface area of 150 m<sup>2</sup>/g[34].

The method has been expanded to produce many mesoporous metal oxides[35], [36]. Two different templates, KIT-6 and SBA-15, were compared and for the first time used in synthesis of mesoporous SnO<sub>2</sub>. This system produced nanowires with a diameter of 6 nm and showed a good capacitance properties[37]. Mesoporous Co<sub>3</sub>O<sub>4</sub> was also attempted to synthesize using the same templates, mentioned above. A highly ordered mesoporous structure was obtained with a pore size of 3 nm. After that, the method became universal and opened many possibilities for the synthesis of many other metal oxides using mesoporous silica as hard template[38].

Later, Shopsowitz et al. introduced a new class of mesoporous materials with a chiral pore structures, templated by a lyotropic liquid-crystalline phase of nanocrystalline cellulose (NCC). The cellulose is condensed on a silica template. Then, TiO<sub>2</sub> was formed on the silica template with a chiral orderings, and the porosity of obtained on titanium dioxide is determined by the porosity of silica template[39].

The main advantages of hard templating or nano-casting is that it is possible to control the mesostructure of the desired material by choosing a right hard template with a desired mesostructure. Also, the temperature resistance of most of the silica templates makes them desirable for producing more crystalline material with a high surface area. However, to remove the templates, HF or NaOH must be used, so the metal oxide must be stable to those reagents. This limits the choice of metal oxides that one can synthesize. Silica might also react with the precursor solution or later in the calcination to produce metal silicates, so this method cannot be applicable to all transition metal oxides (ZnO, Al<sub>2</sub>O<sub>3</sub>) [8]. And, more importantly, unfortunately hard templating is not a one step process and it is usually an expensive method to apply[8]. Therefore, new methods are required to synthesize metal oxides.

#### **1.4. Lyotropic liquid crystal templating (SLCT) and Molten Salt Assisted Self Assembly (MASA)**

There are two types of liquid crystals: thermotropic liquid crystal (TLC) and lyotropic liquid crystal (LLC) [40]. TLC type of structure can be formed by different types organic molecules and their formation depends on the heat, that is why they are called thermotropic[41]. Thermotropic liquid crystals appear at a particular temperature range and usually observed in certain organic compounds with a specific

structure. However, we will not discuss thermotropic LCs any further. Because, it is out of scope of this thesis.

The LLC structures are usually formed by amphiphilic molecules, that have hydrophilic and hydrophobic ends. These molecules are also known as surfactants. Depending on the structure and concentration of the surfactant, they can form lyotropic liquid crystal. The LLC mesophases consist of at least two components, usually a solvent molecule and surfactant together assembles into LLC phases. In the LLC phase, the surfactant molecules are aggregated into micelles like structure with one end residing in the core and the other segment is interacting with the solvent, depending on the polarity of the solvent. As it was already mentioned, surfactants are compounds that have both polar and nonpolar components. [42]. The amount of solvent in the structure of LLC is also critical. Solvent can be water, ionic liquid or hydrated transition metal salt[43], [44].Therefore, the LLC mesophase is very dynamic and depends on concentration of surfactant and temperature. At a specific surfactant to solvent ratio, the LLC mesophase forms [44].

Before going into details, there is a need to give a little insight on the concept of liquid crystals (LC). The LC is a state of matter that has both properties of solid and liquid. Usually liquid crystals have specific defect structure and orientation that can be characterized by a polarized optical microscope if it is an anisotropic phase. However, the LC may also have isotropic phases, such as cubic and disordered phase that can be detected by small angle XRD measurements.

The difference of liquid crystal from solids and liquid is schematically presented in Figure 3.

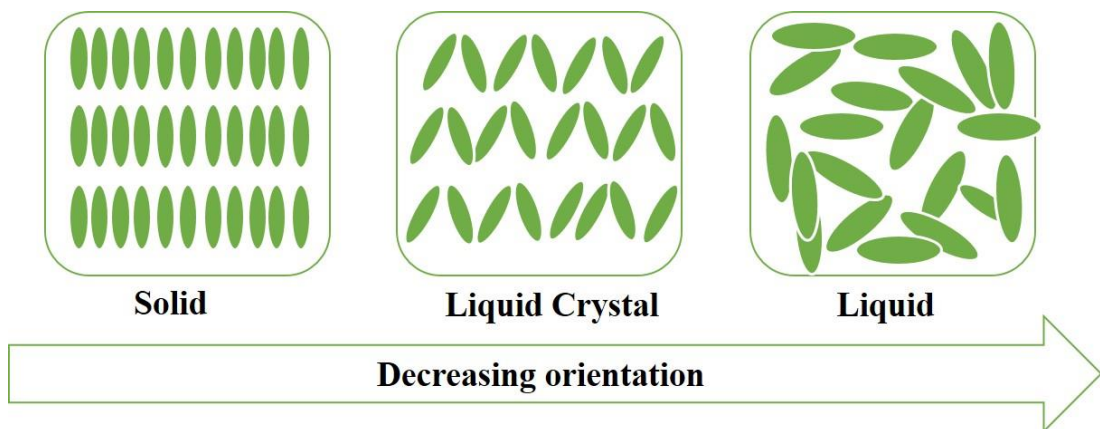


**Figure 3.** Illustration of orientational order in solids, liquid crystals and liquids.

Certain organic molecules or aggregates of surfactants (micelle) have some order in the LC phase. This makes the LC phase like a solid, however it is also fluidic that is similar to a liquid.

Lytotropic liquid crystalline (LLC) templating was introduced by Attard et al. in 1995 by synthesizing mesoporous silica monolith in liquid crystalline mesophase[6]. TEOS was used as a silica precursor and oligoethylene oxide  $C_{12}EO_8$  as a non-ionic surfactant[6]. They demonstrated for the first time that the mesostructure of the LLC can be transformed to a solid. The method has been introduced as true liquid crystalline templating (TLCT). The material obtained was highly ordered mesoporous silica with pore size of around 3 nm [6]. Later, TLC has been employed to produce first examples of mesostructured metals and metal sulfides by Attard's groups and others. For example, later in 1997 mesostructured platinum was synthesized using LLC approach by the same group[45]. The surface area was around  $20 \text{ m}^2/\text{g}$  with a pore size varying from 1.7 to 10 nm[45]. Similarly, ordered mesoporous tin and Pt/Ru alloy were fabricated using the same method. Pore diameter was around 5 nm in both cases[45], [46]. Along with metals and metal alloys, variety of metal oxides and sulfides were also fabricated via LCC approach[9][47], [48]. Hexagonal and lamellar structures of CdS and ZnS have been synthesized with pore sizes ranging from 7 to 10 nm[47]. Mesoporous metal oxides, including  $TiO_2$ ,  $ZrO_2$ ,  $Al_2O_3$ ,  $Nb_2O_5$ ,  $Ta_2O_5$ ,  $WO_3$ ,  $HfO_2$ ,  $SnO_2$ , and mixed oxides  $SiAlO_{3.5}$ ,  $SiTiO_4$ ,  $ZrTiO_4$ ,  $Al_2TiO_5$  and  $ZrW_2O_8$  have been synthesized using lyotropic liquid crystal templating and well characterized[9]. The obtained materials had ordered structures with pore diameters of around 14 nm, and were thermally stable[9]. The main advantages of LLC approach are that the original synthesized mesoporous material replicates the structure and symmetry of the fresh mesophase, which allows to control pore size distribution and pore diameters by playing with surfactant and precursor concentration. The mesostructured solid is the replica of the LLC mesophase. However, the TLCT process has its own limitations, such as transition metal salts as inorganic precursors in large amounts don't participate in the self-assembly process which allows to use only little amount of salt, and it makes complicated to form film or monolith structure. Also, upon evaporation of solvent,

the mesophase is becoming not stable. So new approaches were needed to fabricate mesoporous metal oxides.

A new lyotropic liquid crystalline mesophase was introduced by Dag's research group in 2001[49]. The new mesophase consist of just a salt and surfactant. The salts could be many first row transition metal nitrates ( $[\text{Co}(\text{H}_2\text{O})_6](\text{NO}_3)_2$ ,  $[\text{Ni}(\text{H}_2\text{O})_6](\text{NO}_3)_2$ ,  $[\text{Zn}(\text{H}_2\text{O})_6](\text{NO}_3)_2$ , and  $[\text{Cd}(\text{H}_2\text{O})_4](\text{NO}_3)_2$ ) and the surfactant is an oligo(ethylene oxide). The LLC phases that were formed between non-ionic oligo(ethylene oxides) surfactants and transition metal aqua complexes salts have been investigated by changing the salt to surfactant ratio, salt and surfactant type[49]. Salt species play important roles and act as a second component (solvent) of the LCC phase. The coordinated water molecules enforces the assembly of surfactant molecules into micelle structure that come together to form hexagonal and cubic mesophases[49]. Different nonionic surfactants, pluronics (L64, P65, and P123) were used to form transition metal salt lyotropic liquid crystal mesophases[50]. It has been established that the amount of free water and coordinated water in transition metal nitrates plays role in formation of stable mesophase[50]. However, not only nitrate salts were used as precursors. Along with the different surfactants, effect of counter ion of inorganic precursor salt has been investigated. It was established that ion density is important in the formation of mesophase[51].

It has been established that solubility of surfactant in water depends on the ion salt present in the system (Hofmeister Series)[52]. So, the stability of the LC mesophase depends on hydrophilicity of nonionic surfactant, which depends on anions and coordination of anions to a metal ion [51]. The effect of anions and cations to the salt-surfactant LLC mesophases have been investigated in many studies in our group[51][52].

However, as it was already mentioned, the LLC mesophases are very sensitive to anions, and unfortunately do not hold enough salt species in the structure, so, a charged surfactant, CTAB, was introduced to enhance the hydrophobicity of the core and hydrophilicity of the EO shell so mesophase can keep high salt concentrations in the mesophase[53]. The mixture of two surfactants, a non-ionic and a cationic( $\text{C}_{12}\text{EO}_{10}$ -CTAB and  $\text{C}_{12}\text{EO}_{10}$ -SDS), and  $[\text{Zn}(\text{H}_2\text{O})_6](\text{NO}_3)_2$  formed lyotropic liquid mesophase, and the salt to surfactant ratio was increased up to 8 salt/surfactant

mole ratio, which is quite high compared to other LLC mesophase compositions investigated before[49]. The charged surfactant interacts with the non-ionic surfactant and assemble together to form stable mesophase at such high salt concentrations without leaching out salt crystals after free water evaporates. The stability of mesophase can be controlled by increasing amount of CTAB or SDS in the media[53].

Based on this knowledge, it was found out that, confining salt species into a nano-space decreases the melting point of salt and prevents crystallization of salt out of the mesophase, even though salt concentration is very high[54]. That is how the molten salt assisted self-assembly (MASA) has been introduced to synthesize mesoporous metal titanates ( $\text{Li}_4\text{Ti}_5\text{O}_{12}$ ,  $\text{MnTiO}_3$ ,  $\text{CoTiO}_3$ ,  $\text{CdTiO}_3$ ,  $\text{Zn}_2\text{TiO}_4$ , etc.)[55]. In the MASA process, two surfactants,(a charged and nonionic) and two solvents (salt and a volatile solvent) are needed. In the synthesis of mesoporous titanates, the titania source undergoes hydrolysis and condensation reactions in the LLC mesophase of salt-surfactant at low temperatures to form a mesostructured solid that can be heat treated to form the mesoporous titanates. Prior to calcination, the mesostructure is very stable and holds the salt species in their molten phase [55], [56]. In one of the recent work, a mesoporous  $\text{LiCoO}_2$  and  $\text{LiMn}_2\text{O}_4$  have been synthesized using MASA approach[57]. In that study, the MASA method has been modified by replacing CTAB that undergoes reaction with salt species to form  $(\text{CTA})_2[\text{MBr}_4]$  crystals with CTAN (N stands for nitrate) to avoid  $\text{MBr}_2$  impurities[57] in the final product. The formation and phase separation of  $(\text{CTA})_2[\text{MBr}_4]$  crystals produce first  $\text{MBr}_2$  crystals at low temperatures and at higher temperatures metal oxides in their bulk form in the calcination process and contaminates the product with low surface area materials. Therefore, the  $(\text{CTA})_2[\text{MBr}_4]$  formation must be avoided. CTAN, as a charge surfactant, has been used to avoid these formations to produce a more homogenous mesoporous material. However, CTAN require a tedious and expensive synthesis procedure [57]. Fortunately, these formations in the nickel case were limited and did not affect the process; therefore, CTAB was used as a charge surfactant throughout this thesis work.

Considering all the mentioned details of the process, the MASA process is one of the advantageous methods to produce mesoporous materials and it is quite flexible such

that it can easily be adopted to other metal oxides. Here, in this thesis we introduce two of those materials, namely mesoporous nickel oxide and nickel cobaltite. It allows playing with composition of a precursor solution, and correspondingly changing the structure of the resulting mesoporous material. Since large amounts of salt is accommodated into a mesophase, it makes possible to produce mesoporous thin films and monoliths[54], [56]. Also, it is a one pot synthesis method and does not require any sophisticated fabrication routes.

### **1.5. Mesoporous Nickel Oxide and Nickel Oxide Nanoparticles.**

Recently, mesoporous and also nanoparticles of metal oxides attracted a lot of attention in variety of applications due to their optical, catalytic, and electrochemical properties, such as supercapacitors, electrochromic devices, solar cells, gas sensors, batteries etc.[58], [59]. Nickel oxide being a p-type semiconductor, and depending on synthesis route can possess high surface area is used as electrochromic device, supercapacitor, electrode, catalyst and in photovoltaic devices[60], [61].

As it was already mentioned, in this thesis, the MASA approach was employed to synthesize mesoporous nickel oxide. Let us also briefly mention some other synthesize routes of NiO thin films and nanoparticles. One of the most familiar methods to fabricate NiO is a sol-gel method[62]. Spherical nanoparticles of NiO were produced by using nickel nitrate hexahydrate precursor solution of, [62]. The surface area of the nickel oxide synthesized by sol-gel route was  $322 \text{ m}^2/\text{g}$ [63]. Another well-known route is a wet-chemical synthesis method to produce nickel oxide nanoparticles using nickel chloride hexahydrate solution and sodium hydroxide as a precipitating agent[64]. A very high surface area of  $377 \text{ m}^2/\text{g}$  for NiO nanosheets with a nanosheet thickness of around 2 nm was achieved by this method[63]. Nanorods, nanosheets, spherical nanoparticles of 96 nm of NiO particles have also been fabricated using a hydrothermal method[65], [66]. This method has been conducted in aqueous solution under a high temperature and high pressure. By varying those parameters the morphology of the nickel oxide can be controlled[67]. Method, like microwave heating, has been employed as well by Meher et al. to fabricate highly porous nickel oxide spheres. This method was very fastquick and efficient compared to other above mentioned methods[68]. Nano-flowers of nickel

oxide with a 5 nm thickness have been fabricated by microwave method with a surface area of 125 m<sup>2</sup>/g[68].

To summarize, generally the synthesis method dictates on the morphology of nickel oxide and accordingly nickel oxide can possess different properties for different applications. For instance, smaller particle size and high surface area ensures that nickel oxide can be used as a supercapacitor as capacitance depends on the dielectric layer and dielectric layer depends on surface area[69]. Electrical and optical properties of NiO also depends on the particle size[70], [71]. Band gap of NiO depends on the calcination temperature and it decreases with increasing calcination temperature[72].

Electrochemical behavior of the NiO electrode was investigated by cyclic voltammetry technique using a three-electrode cell, consisting of a reference electrode, working electrode and counter electrode in a basic electrolyte solution. Working electrode is usually the analyzed material, reference electrode calibrates the applied voltage and counter electrode ensures the other half-reaction and completes the circuit[73]. Capacitance can be calculated from the cyclic voltammograms using the following formula:

$$C = \frac{i}{Sm}$$

Where, C – capacity of working electrode, S – scan rate, i – average current, and m - mass of electrode[74].

Depending on the synthesis route and morphology, nickel oxide showed different capacitance values. For example, NiO nanoflakes synthesized by wet chemical synthesis method showed a specific capacitance of around 600 F/g, which is considered to be very high[75]. Xing et al. did temperature dependent capacitance measurement and it was established that with increasing calcination temperature, the capacitance of NiO nanospheres fabricated by hydrothermal route is increasing[76]. The maximum specific capacitance reached was 960 F/g from nickel oxide nanotubes, fabricated by microwave method[77].

Apart from being good electrode material, NiO can also be used in other applications, like electrochromism[78]. Nickel oxide turns dark brown (almost black) upon oxidation to NiOOH (Ni<sup>3+</sup>) and colorless (bleached) upon complete reduction

back to  $\text{Ni}^{2+}$ [79]. Electrochromism is a reversible change of optical properties under a potential window. Electrochromic windows have been fabricated and used as smart windows[80]. Plenty of research has been done in this area using nickel oxide. One of the earliest works on electrochromic nickel oxide was done by Carpenter *et. al* [81] using an electrodeposited film on FTO substrate with a thickness of less than 100 nm. The potential window was between 0.0 and 0.6 V. Contrast between bleached and colored state was measured using absorption spectroscopy and displayed almost 0.8 absorbance. However, cycling the film deteriorated and the contrast was significantly reduced[81].

Garcia-Miquel *et al.* attempted to synthesize a NiO film by sol-gel method for electrochromic application[82]. A homogenous thin film on ITO substrate with a thickness 100 nm was produced and showed good contrast even after 100<sup>th</sup> in a voltage range of 0.2 to 1.0 V. The film was quite reversible but after 100<sup>th</sup> cycle, the contrast was reduced, as the film was not stable in the solution[82]. Another method to produce nickel oxide film for electrochromic application is a chemical vapor deposition, where the film thickness can be varied between 500 and 1000 nm[83]. The applied voltage range was from -0.5 to 1.7 V vs SCE. The film was exposed to 1000 bleaching/darkening cycles, and showed a good reversibility[83]. Another NiO film with a thickness of 500 nm was fabricated over a ITO surface by magnetic sputtering method[84]. Electrochromic measurement was conducted at a voltage range of 0.5 to 0.65 V vs Ag/AgCl in KOH. Considerable contrast was observed even after 1000<sup>th</sup> cycle telling that the film quality did not change upon cycling[84]. In this thesis work, cyclic voltammetry and electrochromic measurements will be used as characterization techniques to better understand electrochemical properties of mesoporous nickel oxide fabricated by MASA process.

### **1.6. Mesoporous Nickel Cobaltite and Nickel Cobaltite Nanoparticles**

Spinel  $\text{NiCo}_2\text{O}_4$  is generally known as a good supercapacitor[85]. There are many investigations on this material in the literature over the years.

To fabricate nickel cobaltite thin film or nanoparticles, variety of methods have been developed: such as sol-gel [86], hard-templating[87], electrodeposition[88], and hydrothermal methods[89].

As in the case of nickel oxide, a desired morphology is dictated by the synthesis method, and for the supercapacitors three-dimensional structure is more desired that it provides larger surface area[85].

Wei et al. prepared nickel cobaltite at 200 °C with a high specific surface area and a pore size of around 4 nm, using simple sol gel method, with a specific capacitance of 1400 F/g[90]. That capacitance was considered to be extremely high[90]. A higher specific capacitance of 1128 F/g was reported by another group[91]. This material had a pore size of around 11 nm and surface area of 32 m<sup>2</sup>/g, as the calcination temperature reached to 300 °C [91]. Xiong et al. fabricated NiCo<sub>2</sub>O<sub>4</sub> nanotubes with a high specific capacitance of 1696 F/g, using hard templating method [92]. The structure of the obtained material is highly ordered and 3-dimensional, that ensured a high specific capacitance. Shem et al. attempted to use self-template method to fabricate hollow spheres of nickel cobaltite[93] that had a specific capacitance of 917 F/g[93]. Electrospinning method produced 2 dimensional nickel cobaltite with a capacitance of 1647 F/g[94]. These nanotubes had a high surface area with an average pore size of 89 nm with an ordered porous structure[94]. Electrodeposition method produced NiCo<sub>2</sub>O<sub>4</sub> with very high specific capacitance of around 2500 F/g[88]. The ultrathin morphology of oxide and 3D structure of nickel foam substrate provided this material with that outstanding super capacitive performance[88].

In one of the most recent works, Yang et al. produced nickel cobaltite nanosheets on metal-organic framework-derived mesoporous carbon nanofibers with specific capacitance of 1632 F/g[95]. As NiCo<sub>2</sub>O<sub>4</sub> was coated on the surface of conductive substrate, it provided this material with high capacitance and long cycling durability[95].

To sum up the differences between all these methods, it can be concluded that, templating method is the best method to produce NiCo<sub>2</sub>O<sub>4</sub> for supercapacitor applications as it makes 2D and 3D structured material. Sol gel method is less desirable as it produces nanoparticles and makes the electrode fabrication complicated[85].

Apart from being good supercapacitor, nickel cobaltite can also be used in other applications. Zhang et al. investigated mesoporous NiCo<sub>2</sub>O<sub>4</sub> as counter electrode for dye-sensitized solar cells[96]. Electrospinning synthesis method was used and

honeycomb structured oxide showed a better performance than nanotube ones due to a higher surface area. The performance of the electrode was as good as standard platinum counter electrode with a 7.09 % solar efficiency[96].

Electrochemical catalytic performance of  $\text{NiCo}_2\text{O}_4$  was investigated as well by Shi et al[97]. Nanoneedles and nanosheets of nickel cobaltite were fabricated and compared in performance. Oxygen evolution reaction was more efficient on nanoneedle structured electrode, as it was richer in Co element and ensured a better surface contact with electrolyte[97]. Li et al. have analyzed the property of nickel cobaltite to separate water from oil[98]. The  $\text{NiCo}_2\text{O}_4$  was coated on the nickel foam. Different structures showed different ability to separate water from oil, and nanoflakes coated nickel foam showed a better performance. Considering also that  $\text{NiCo}_2\text{O}_4$  is a reusable material it has future possibilities in eco-friendly technologies[98]. As  $\text{NiCo}_2\text{O}_4$  showed excellent capacitive performance, it could also be used as an anode material for Li-ion batteries[99]. Solvothermal method was used to synthesize nickel cobaltite microspheres with a surface area of  $41 \text{ m}^2/\text{g}$  and pore size of 14.5 nm. The uniform pore size distribution allowed a fast Li ion transfer and showed excellent electrochemical performance and stability[99].

Prathap et al. investigated electrocatalytic performance of nickel cobaltite on oxidation of methanol[100]. The hydrothermal route was used to fabricate electrodes, and results were compared with NiO and  $\text{Co}_3\text{O}_4$ . Even though NiO showed higher surface area, the electrocatalytic performance of  $\text{NiCo}_2\text{O}_4$  was better[100].

In this thesis, the MASA approach was developed to synthesize mesoporous  $\text{NiCo}_2\text{O}_4$ . Electrochemical and other characterization techniques were used to show water oxidation and electrochemical performance of nickel cobaltite electrodes.

# CHAPTER 2

## 2.EXPERIMENTAL PROCEDURE

### 2.1. Materials

Nickel nitrate hexahydrate ( $[\text{Ni}(\text{H}_2\text{O})_6](\text{NO}_3)_2$ ) and cobalt nitrate hexahydrate ( $[\text{Co}(\text{H}_2\text{O})_6](\text{NO}_3)_2$ ) was used as a non-volatile solvent(s) and Ni(II) and Co(II) precursors, respectively. Cetyltrimethylammonium bromide ( $[(\text{C}_{16}\text{H}_{33})\text{N}(\text{CH}_3)_3]\text{Br}$ , denoted as CTAB) was used as a charged surfactant in the media to accommodate high salt concentration and structure directing agent together with nonionic surfactant, 10 lauryl ether ( $\text{CH}_3(\text{CH}_2)_{11}(\text{OCH}_2\text{CH}_2)_{10}\text{OH}$ , denoted as  $\text{C}_{12}\text{E}_{10}$ ). All chemicals were purchased from Sigma-Aldrich and used without further purification.

### 2.2. Preparation of Ni(II) Solutions

Solutions were prepared with different salt to surfactant mole ratios (from 2 to 30  $[\text{Ni}(\text{OH}_2)_6](\text{NO}_3)_2/\text{C}_{12}\text{E}_{10}$  mole ratio). Concentration of CTAB and  $\text{C}_{12}\text{E}_{10}$  were kept constant (1:1 in all solutions) by changing the  $[\text{Ni}(\text{OH}_2)_6](\text{NO}_3)_2/\text{C}_{12}\text{E}_{10}$  mole ratio. In all solutions, the amount of CTAB and  $\text{C}_{12}\text{E}_{10}$  were 0.291 and 0.500 g, respectively. A more detailed composition information is provided below in Table 1. Ethanol was used as a primary solvent to homogenize the solutions, in which the ethanol amount was 5 ml in 2 to 12 salt/surfactant ratios to 10 ml in the 15 to 30 mole ratios.

In a typical solution preparation, the following procedure has been used: first add the the desired amount of Ni(II) salt, 0.291 g CTAB, and 5 ml ethanol into a vial and stir the mixture for 15 min using magnetic stirrer to obtain a clear solution. Then, add

0.500 g of the non-ionic surfactant (C<sub>12</sub>E<sub>10</sub>) to the clear solution and stir for another 30 mins.

### 2.3. Preparation of Mesoporous NiO Films

Above clear solutions were spread on glass slides via spin coating or drop casting methods to obtain fresh LLC mesophases. Drop casting produces thicker films. In contrast, the spin coated samples are thin films, and the thickness can be adjusted by controlling the spin rate or by the amount of ethanol in the solutions. Spin coating was done at a spin rate of 2000 rpm for 10 seconds that ensures an immediate evaporation of ethanol and gelation. Drop casting was employed by spreading a few drops of the above solution over the glass substrate. Then, it was kept 2-3 minutes under ambient conditions to fully evaporate the volatile solvent (ethanol) before inserting them into an oven for further heat treatment. Finally, the films were calcined at various temperatures (at 250, 300, 350, 400, 450, and 500 °C) to produce mesoporous nickel oxide (m-NiO) films. Calcination time was 1 hour at each temperature. Detailed schematic representation of the synthesis is given in Figures 4 and 5.

**Table 1.** Composition of the clear solutions used for the preparations of mesoporous NiO films.

Ni(II)/C <sub>12</sub> E <sub>10</sub> Mole Ratio	Amount of [Ni(OH <sub>2</sub> ) <sub>6</sub> ](NO <sub>3</sub> ) <sub>2</sub> (g)	Amount of CTAB (g)	Amount of C <sub>12</sub> E <sub>10</sub> (g)	Amount of Ethanol (ml)
2:1	0.437	0.291	0.500	5
4:1	0.928	0.291	0.500	5
6:1	1.392	0.291	0.500	5
8:1	1.856	0.291	0.500	5
10:1	2.321	0.291	0.500	5
12:1	2.753	0.291	0.500	5
15:1	3.481	0.291	0.500	10
20:1	4.641	0.291	0.500	10
25:1	5.801	0.291	0.500	10
30:1	6.962	0.291	0.500	10

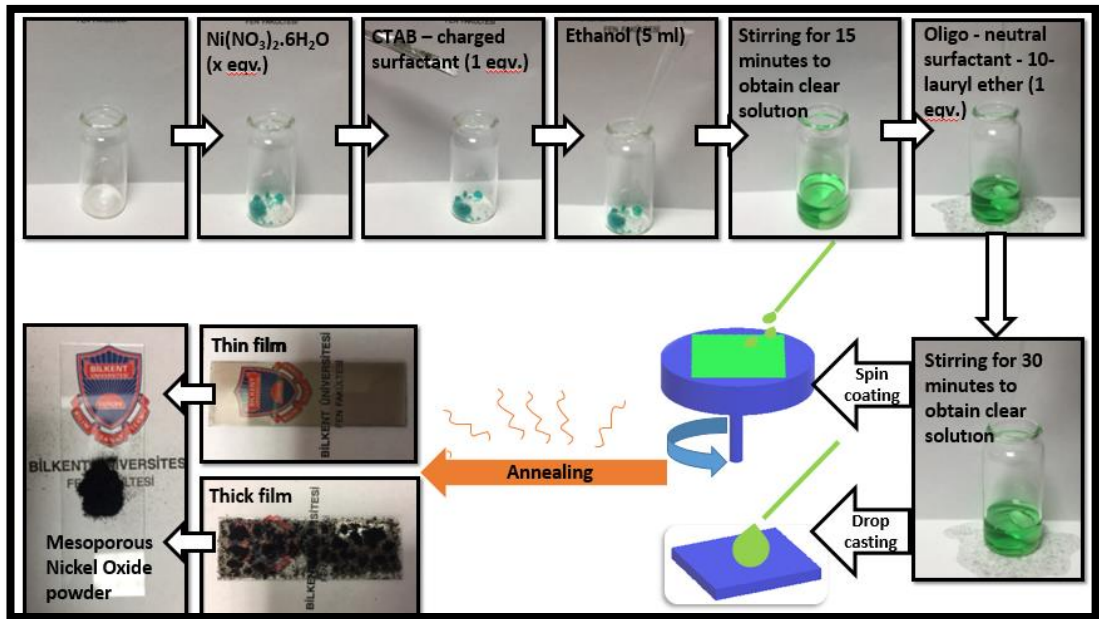


**Figure 4.** Photographs and schematic representations of the preparation of Ni(II) solutions and calcination products.

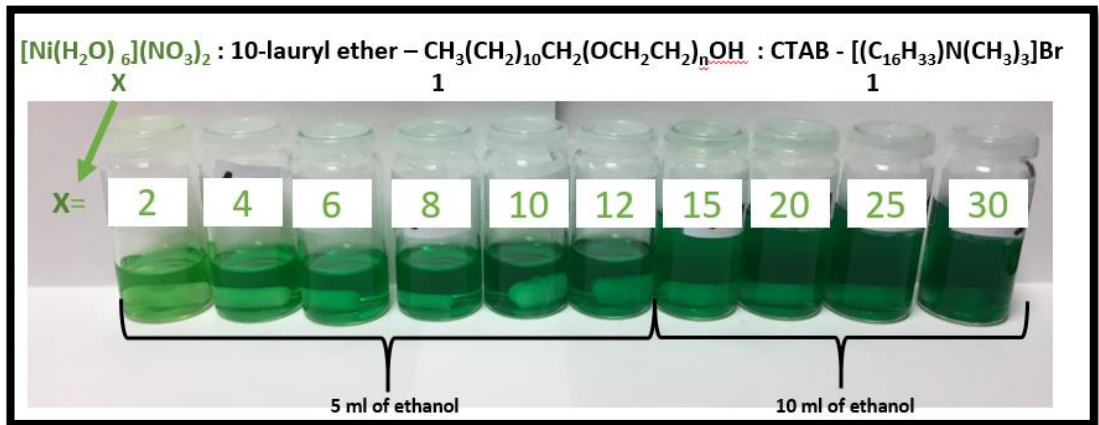


**Figure 5.** Photographs of the clear solutions with varying Ni(II)/ $\text{C}_{12}\text{E}_{10}$  mole ratios, as shown on the vials.

#### 2.4. Preparation of Ni(II) and Co(II) Mixed Solutions

Solutions were prepared with different total salt (Ni(II) and Co(II)) to surfactant mole ratios (from 6 to 25). The nickel to cobalt salt ratio was kept 1:2 to make sure the calcination product is a spinel structure of  $\text{NiCo}_2\text{O}_4$ . Concentration of CTAB and  $\text{C}_{12}\text{E}_{10}$  were kept constant at 1:1 ratio in all solutions and were used at amounts of

0.291 and 0.500 g, respectively. A more detailed composition information is given below in Table 2.

Ethanol was used as a primary solvent to homogenize the mixtures. As in the case of the nickel solution preparation, higher salt ratios required more ethanol to obtain clear solutions. Thus, from 6 to 12 salt to surfactant mole ratios, the amount of ethanol to homogenize the mixtures was 5 ml, and from 15 to 25 10 ml of ethanol was used. The typical solution preparation is not different from the Ni(II) solution preparation: for example for 6 mole ratio, first add 0.464 g Ni(II) and 0.929 g Co(II) salts, 0.291 g CTAB, , and 5 ml ethanol into a vial and stir for 15 min using magnetic stirrer to obtain clear solution. Then, add 0.500 g non-ionic surfactant (C<sub>12</sub>E<sub>10</sub>) to the clear solution and stir for another 30 mins to obtain clear and homogeneous solutions. Accordingly, change the amount of Ni(II) and Co(II) amounts, as listed in Table 2, for the other solutions.

**Table 2.** Composition of the clear solutions used for the preparations of mesoporous NiCo<sub>2</sub>O<sub>4</sub> films.

Co(II)+Ni(II)/C <sub>12</sub> E <sub>10</sub> Mole Ratio	Amount of [Co(OH <sub>2</sub> ) <sub>6</sub> ](NO <sub>3</sub> ) <sub>2</sub> (g)	Amount of [Ni(OH <sub>2</sub> ) <sub>6</sub> ](NO <sub>3</sub> ) <sub>2</sub> (g)	Amount of CTAB (g)	Amount of C <sub>12</sub> E <sub>10</sub> (g)	Amount of Ethanol (ml)
6:1	0.929	0.464	0.2908	0.500	5
8:1	1.239	0.619	0.2908	0.500	5
10:1	1.548	0.774	0.2908	0.500	5
12:1	1.858	0.928	0.2908	0.500	5
15:1	2.322	1.160	0.2908	0.500	10
20:1	3.097	1.547	0.2908	0.500	10
25:1	3.871	1.934	0.2908	0.500	10

### 2.5. Synthesis of Mesoporous NiCo<sub>2</sub>O<sub>4</sub> Films

Above clear solutions were spread on glass slides via either spin coating or drop casting methods to obtain fresh LLC films or thicker gels, respectively. Thickness of the films can be varied by spin rate or by controlling the ethanol amounts in the solutions. The spin coating was done at a spin rate of 2000 rpm for 10 seconds. This ensures an immediate ethanol evaporation and gelation. Drop casting is employed by spreading a few drops of the solution over glass substrate. The drop cast coated samples must be kept for 2-3 min under laboratory condition before inserting them

into a preheated oven. This ensures the evaporation of ethanol from the media to form the gel mesophase. Then the films were calcined at various temperatures (at 250, 300, 350, 400, 450, and 500°C) to produce mesoporous nickel cobaltate (m-NiCo<sub>2</sub>O<sub>4</sub>) films. Annealing time was 1 hour at each temperature. Detailed schematics of the synthesis is shown in Figure 6.

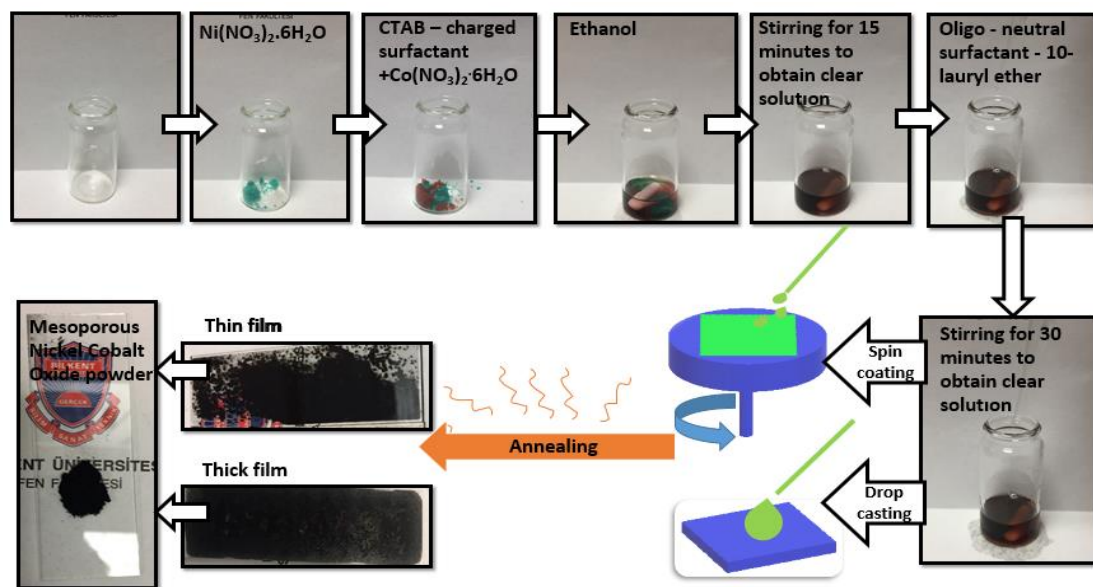


**Figure 6.** Photographs and schematic representations of the preparation of the Co(II) and Ni(II) mixed solutions and calcination products.

## 2.6. Preparation of the Electrodes and Electrochemistry Setup

Calcined nickel oxide and nickel cobaltate samples were analyzed using the following procedure. Fluorine doped tin oxide (FTO) glass was coated using the fresh Ni(II) or mixed Ni(II) and Co(II) solution using spin coating method at 2000 rpm. Then the freshly prepared sample was calcined at various temperatures starting from 250 °C to 500 °C. The prepared electrodes were further used for electrochemical characterization. The photographs of a set of electrodes, calcined at different temperatures are shown in Figure 7.

The electrochemical cell components are: working electrode (WE) – NiO or NiCo<sub>2</sub>O<sub>4</sub> coated FTO, reference electrode (RE) – Ag/AgCl, and a counter electrode (CE) –Pt wire, its schematic representation is shown in Figure 8.

Cyclic Voltammetry measurements were performed at a potential window of -0.4 V to 1.2 V with 50 mV/s scan rate (or at various scan rates, depending on question, see latter in the results and discussion section) using Gammry 750 (PCI4G750-49046).

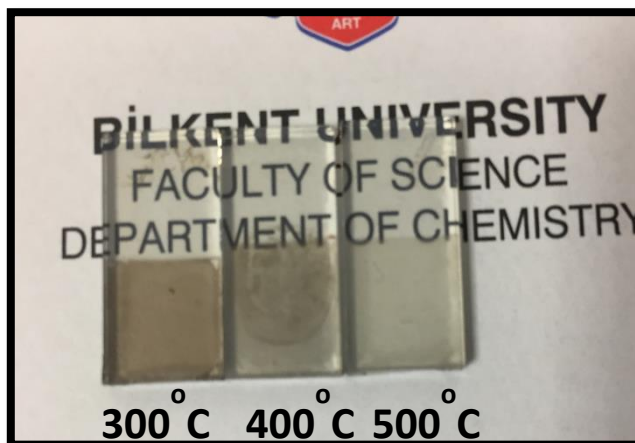


**Figure 7.** Photographs of the freshly prepared mesoporous nickel oxide electrodes on the FTO glass.

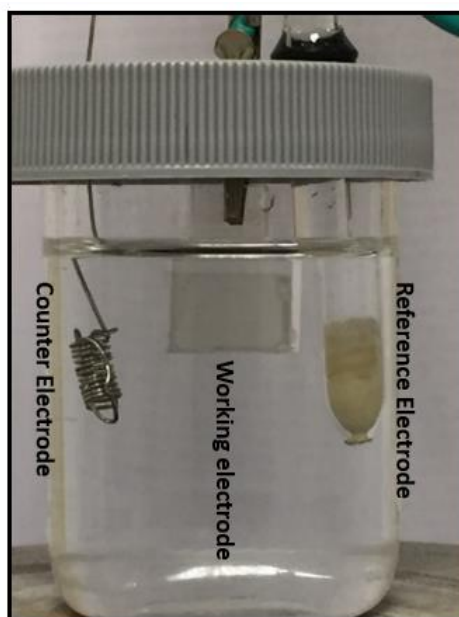


**Figure 8.** Electrochemical cell and components in a 1 M KOH solution.

The spectroelectrochemical measurements were conducted in a standard quartz cuvette. A fiber optic Gamry Instruments SPECTRO-115E spectrometer fitted with a Gamry Instruments Tungsten/Deuterium source was used to collect the UV-Vis spectra.

## **2.7. Instrumentation**

### **2.7.1. Powder x-Ray Diffraction (PXRD)**

Powder x-ray diffraction (XRD) patterns from the drop cast coated and calcined samples (wide angle region) and spin coated fresh samples (small angle region) were collected using Rigaku Miniflex diffractometer, equipped with a Cu K $\alpha$  ( $\lambda=1.54056$  Å) x-rays source, operating at 30 kV/15 mA and a Scintillator NaI (T1) detector with a Be window and Pananalytical X'Pertpro Multipurpose x-ray diffractometer, equipped with a Cu K $\alpha$  ( $\lambda = 1.5405$  Å) x-rays source, operating at 45 kV/40 mA.

### **2.7.2. Polarized Optical Microscopy (POM)**

POM images of the fresh and aged gel phases were recorded using ZEISS Axio Scope A1 polarizing optical microscope.

### **2.7.3. N<sub>2</sub> Adsorption Desorption Measurements**

N<sub>2</sub> adsorption-desorption isotherms were collected using Micromeritics Tristar 3000 automated gas adsorption analyzer in the range of 0.01 to 0.99 P/P<sub>0</sub>. The calcined samples were scraped from the glass substrate with razor blade, grinded to a powder, then dehydrated under a vacuum of 35-40 mtorrs at 200 °C for 2 hours prior to measurements to remove adsorbed water and other volatile species from the pores. The surface areas of the different samples measured were calculated in the range 0.05 to 0.3 atm relative pressure with 5 points.

### **2.7.4. Scanning Electron Microscopy (SEM)**

The SEM images were recorded using FEI Quanta 200 F scanning electron microscope on aluminum sample holders. Samples were scratched from the glass slides and tiny amount of powder was put to conductive carbon tape, that was attached to aluminum sample holder.

### **2.7.5. Transmission Electron Microscopy (TEM)**

The TEM images were recorded on a FEI Technai G2 F30 at an operating voltage of 200 kV. The samples (spin coated at 5000 rpm and calcined at various temperatures for 1 hr) were scraped from glass slides. The collected powder was ground in a mortar and dispersed in 5 ml ethanol for 10 mins using a sonicator to make sure homogeneous particle dispersion. Then, a few drops of the above mixture were put on a TEM grid and dried for 15 min under a powerful light source.

#### **2.7.6. UV-vis Absorption Spectroscopy**

The UV-vis absorption spectra of the thin films coated over quartz slides were recorded using Varian Carry 300 UV-vis double beam spectrophotometer at a 600 nm/min scan rate and 1 nm data interval over a wavelength range of 200 to 800 nm.

#### **2.7.7. X-ray Photoelectron Spectroscopy (XPS)**

The XPS spectra were collected using Thermo Scientific K-alpha x-ray photoelectron spectrometer with an Al  $K_{\alpha}$  micro-focused monochromatic source (1486.6 eV and 400  $\mu$ m spot size) along with a flood gun for charge neutralization. The scraped powder samples from FTO electrodes (coated with nickel oxide before and after exposed to 1000 cyclic voltammogram (CV) cycles at a potential range of -0.4 V to 1.2 V with a scan rate of 200 mV/s) were put on a copper tape for XPS analysis.

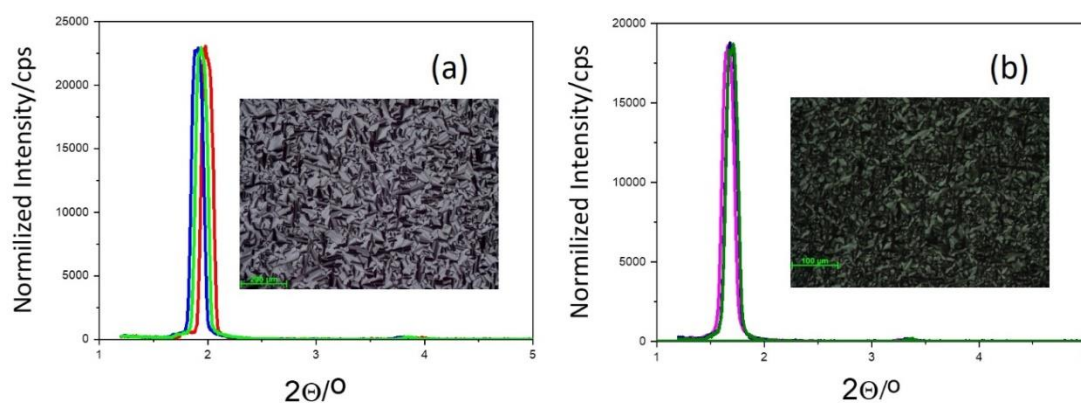
# CHAPTER 3

## 3.RESULTS AND DISCUSSION

### 3.1. Freshly Prepared Ni(II)/C<sub>12</sub>E<sub>10</sub> Film Characterization

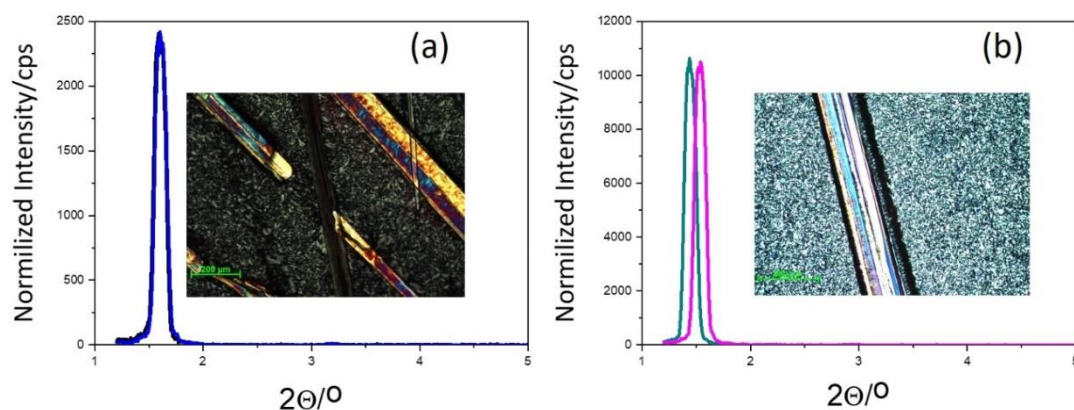
The first step of the synthesis process is preparation of a precursor solution, which was explicitly described in experimental part. All solutions contain the same amount of CTAB and C<sub>12</sub>E<sub>10</sub> but varying amount of Ni(II) salt in ethanol and used as prepared in further steps of the process. The next step is to obtain a gel phase by two methods of coating: drop casting and spin coating. This is simply an evaporation of the volatile component (ethanol) from the solution. This process ensures to obtain a lyotropic liquid crystalline (LLC) mesophase as a thick (in case of drop casting) and thin (in the spin coating) gel films. The gel phase has been characterized by using small angle x-ray diffraction (XRD) and polarized optical microscope (POM) imaging techniques.

The fresh gel films, obtained by spin coating, were investigated in a wide range of salt to surfactant ratio, starting from 2 to 30 mole ratio. The mesophases of the fresh films were decoded as #Ni(II)/C<sub>12</sub>E<sub>10</sub> where # is the Ni(II)/C<sub>12</sub>E<sub>10</sub> mole ratio (e. g. 2Ni(II)/C<sub>12</sub>E<sub>10</sub>).



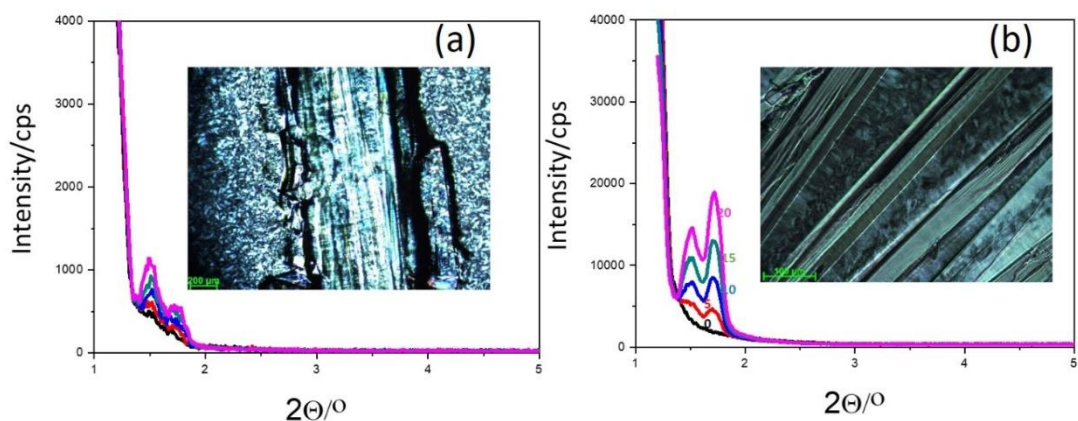
**Figure 9.** XRD patterns of #Ni(II)/C<sub>12</sub>E<sub>10</sub>, where the # is (a) 2 and (b) 4 over time, immediately after coating, 1 hr, and 8 hrs. Insets are POM images of 1-day aged samples.

Figure 9 shows a set small angle XRD pattern of the samples prepared using Ni(II)/C<sub>12</sub>E<sub>10</sub> mole ratio of 2 and 4 over time. The diffraction lines shift towards higher angles with aging the samples, indicating a shrinking of the mesophase due to further solvent evaporation (ethanol and extra water). It is difficult to identify the structure of the mesophase from a single XRD line, but the POM images clearly show that both samples have a 2D hexagonal phase. The POM image displays a fan-texture that is characteristic for the hexagonal mesophase. Therefore, the XRD line corresponds to (100) plane of 2D hexagonal mesophase. Considering that the salt to surfactant ratio is very low, no salt crystal was observed after one-day aging of the gel sample. So, the stability of this sample was confirmed by those observations under the optical microscope.



**Figure 10.** XRD patterns of #Ni(II)/C<sub>12</sub>E<sub>10</sub>, where the # is (a) 6 and (b) 8 over time, immediately after coating and 1 week of aging. The insets are POM images of 1-week aged samples.

The same analysis was done for the other salt ratios. The samples, 6Ni(II)/C<sub>12</sub>E<sub>10</sub> and 8Ni(II)/C<sub>12</sub>E<sub>10</sub>, were spin coated and analyzed accordingly, see Figure 10. Aging of these samples was monitored over time, during the solvent evaporation process some salt leached out and the small angle diffraction line shifted to a higher angle. As the 6Ni(II)/C<sub>12</sub>E<sub>10</sub> and 8Ni(II)/C<sub>12</sub>E<sub>10</sub> have relatively high salt to surfactant ratio, the salt crystals were observed after 1 week aging of those gel phases along with fan textures in their POM images.



**Figure 11.** XRD patterns of #Ni(II)/C<sub>12</sub>E<sub>10</sub>, where the # is (a) 10 and (b) 12 over time, immediately after coating, 5, 10, 15 and 20 minutes. Insets are POM images of 1-hour aged samples.

The 10Ni(II)/C<sub>12</sub>E<sub>10</sub> and 12Ni(II)/C<sub>12</sub>E<sub>10</sub> freshly coated samples didn't show any diffraction lines in their XRD patterns (see Figure 11). After 5 minutes, a diffraction line appears, indicating the mesophase formation. These samples with high Ni(II) concentration are not very stable and leach out salt very quickly. However, this mesophase is cubic as the sample appears dark between the cross polarizers under POM. Moreover, some salt crystals appear on the surface of the gel phase over time. The crystallization could be detected by an optical microscope, as the mesophase is slowly releasing the salt crystals the phase changes from cubic to hexagonal mesophase. As a result, a fan texture is observed under POM. Notice also that one can observe two diffraction lines at 1.5 and 1.7°, 2 $\Theta$ , due to the mesophase with high salt content (smaller angle line) and a small amount of salt crystals leach out and reduce the Ni(II)/C<sub>12</sub>E<sub>10</sub> to those compositions that the diffract line appear at high angles. Therefore, the salt leaching could also be monitored by XRD over time.

Much higher salt to surfactant ratio samples were also prepared and analyzed, however these samples have stability for a shorter duration, therefore the amount of ethanol was doubled to prevent quick salt crystallization. Although, the freshly prepared samples didn't diffract at small angles, after 5 minutes aging, the diffraction lines become visible, indicating the formation of a cubic and quite a disordered mesophase (see Figure 12). A similar trend has been observed with increasing the

salt amount in the mesophase with a much faster salt crystallization. Therefore, one must be very careful with the samples with a high salt content, typically above 12.

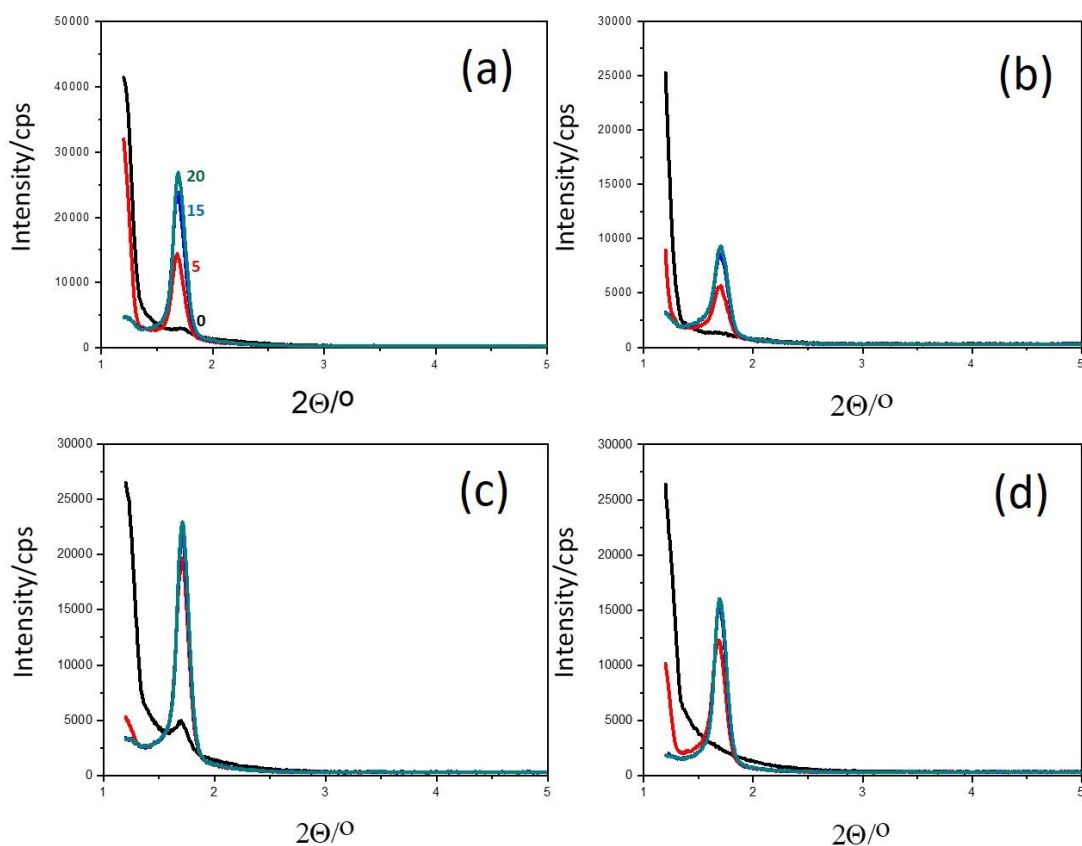


**Figure 12.** XRD patterns of #Ni(II)/C<sub>12</sub>E<sub>10</sub>, where the # is (a) 15, (b) 20 (c) 25, and (d) 30 over time, immediately after coating, 5, 10, and 20 minutes.

### 3.2. Optimization of Coating Method

For further sample characterization, there was a need to determine what method of coating to choose, drop casting or spin coating. In drop casting method, after calcination step, resulted a monolithic film that cracks, however in spin coating method film is very thin and very adhesive to a glass surface, which could be useful for making electrodes. Also spin coating methods allow us to play with film thickness by changing spin rate or diluting/concentrating the precursor solution.

Two films, prepared by two different coating methods, have been analyzed separately. One composition was chosen and separately spin coated and drop casted

on the glass slides and calcined at 300 °C for 1 hour to obtain mesoporous NiO (denoted as m-NiO).

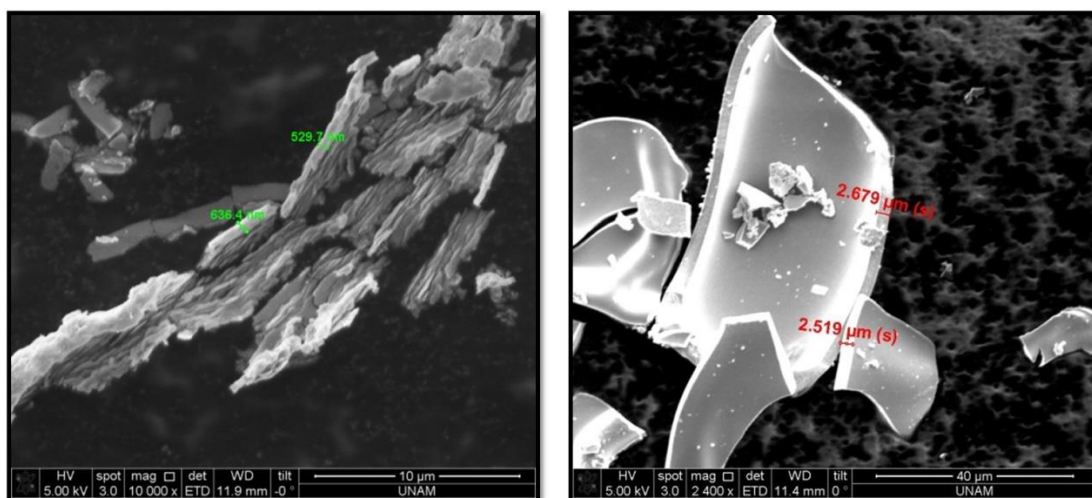


**Figure 13.** SEM images of (left) thin film and (right) drop-cast film of m-NiO.

Figure 13 shows the SEM images of those two samples. The SEM images of both samples show uniform films from both processes. However, the thickness of the spin coated sample is around 400-500 nm while the drop casted sample produces a much thicker monolithic film with a thickness of around 2.5 μm.

Figure 14 shows the XRD pattern of the same two samples. Both samples provide identical XRD patterns that could be indexed to rock-salt NiO structure with similar linewidths, indicating the particle sizes or pore-wall thickness are similar. The patterns were indexed using ICDD data base (PDF card number- 00-044-1159). Accordingly, the lines at 37, 43, 63, 75. And 79°, 2θ, have been indexed to (111), (200), (220), (311), and (222) planes, respectively, of face centered cubic rock-salt structure of NiO.

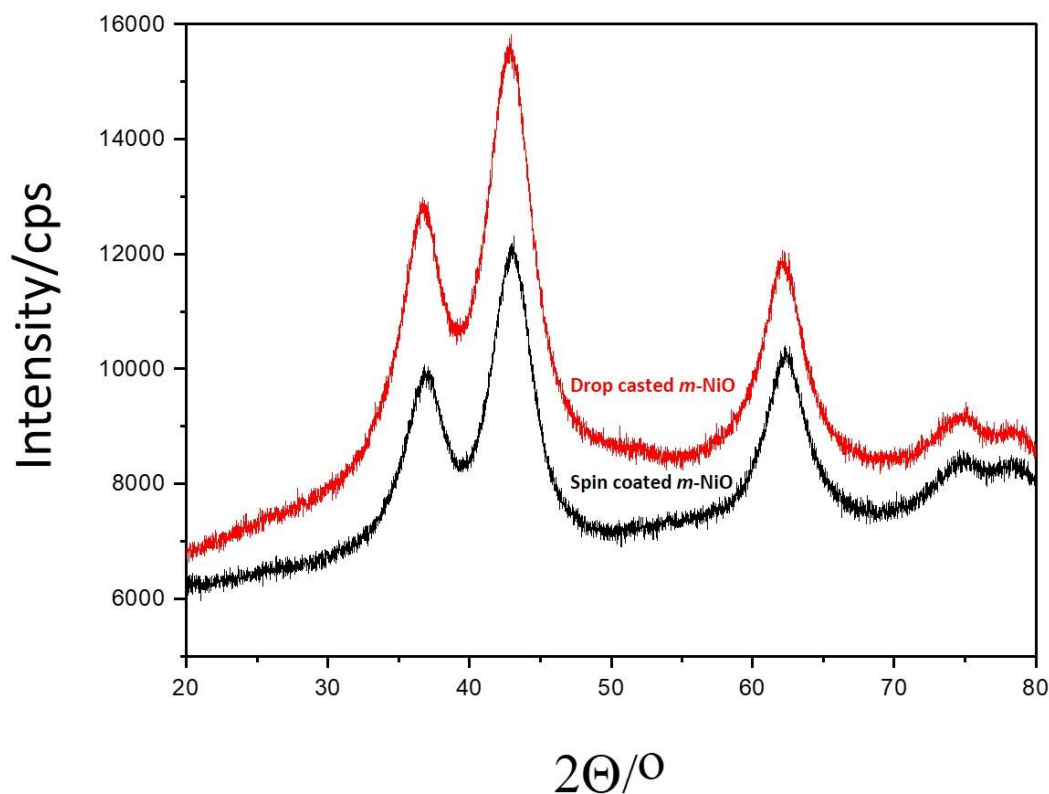


**Figure 14.** XRD patterns of the calcined samples of spin coated (bottom) and drop casted (top) m-NiO at 300 °C.

There is no difference between the two end products, other than the thickness of the films. The method of choice for further characterization has been chosen to be drop casting method as it produces more samples that make the further analysis easy. However, for electrochemical and electrochromic characterizations, the spin coated samples were used, because of better adhesive property to FTO surface (see latter) and proper film thickness. The spin coated film over FTO glass provides a good electrode quality that is important for those electrochemical applications.

### 3.3. Optimization of Salt to Surfactant Ratio

After establishing coating methods for characterization, the optimization of salt ratio is needed to pick the most suitable sample for further analysis. Each sample, starting from 2 to 30 salt to surfactant ratio, was calcined at 300 °C for 1 hour and analyzed separately using XRD and N<sub>2</sub>-adsorption desorption techniques. The calcined films

were labelled as m-NiO-#-XXX, where m stands for mesoporous, # is Ni(II)/C<sub>12</sub>E<sub>10</sub> mole ratio in the precursor solutions, and XXX is the calcination temperature in Celsius. As shown in Figure 15, the color and thickness of the calcined films were different and accord with the salt to surfactant ratio. With increasing salt ratio, the color of the film gets darker as the thickness of the resulted film gets thicker.

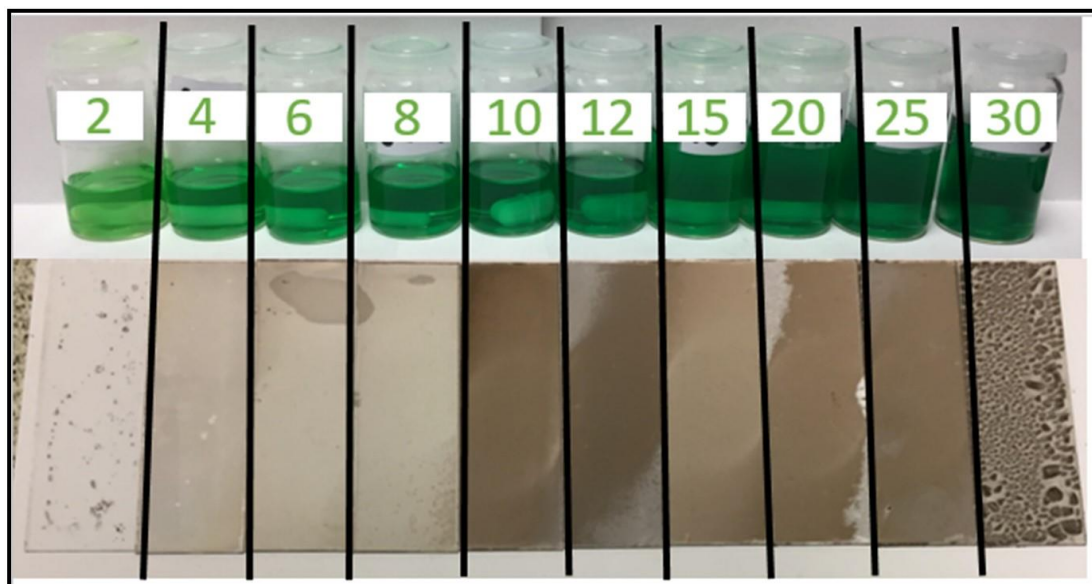


**Figure 15.** Photos of the clear solutions at various concentrations and corresponding thin films obtained after calcination at 300°C starting from 2 to 30 salt/surfactant mole ratio (left to right).

The calcined samples were first analyzed by using PXRD to determine the composition. The samples were scraped from the glass surface by using another piece of microscope glass slide. The XRD patterns of the samples are shown in Figure 16.

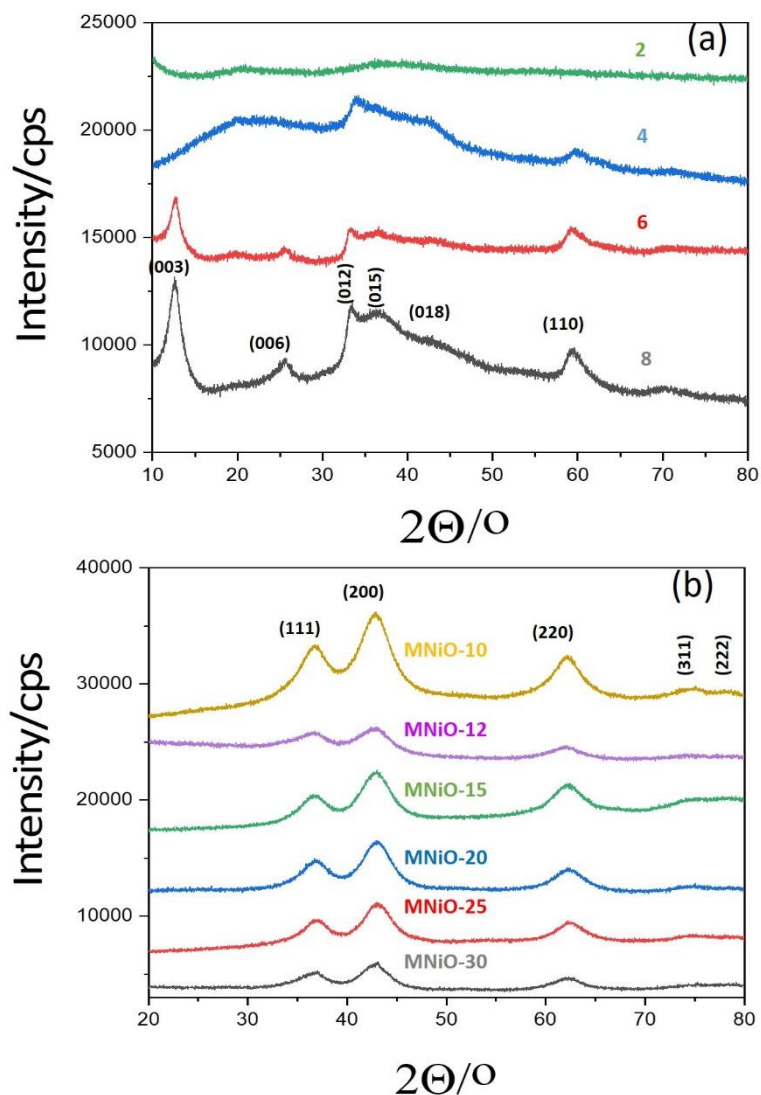


**Figure 16.** XRD patterns (top to bottom) of m-NiO-#-300, where # is (a) 2, 4, 6, and 8 and (b) 10, 12, 15, 20, 25, and 30.

The XRD patterns show that the samples with low salt concentrations (such as Ni(II)-2, Ni(II)-4, Ni(II)-6, and Ni(II)-8) didn't burn effectively at 300 °C to produce a desired product - mesoporous nickel oxide (see Figure 16a). The obtained diffraction lines can be indexed to an  $\alpha$ -Ni(OH)<sub>2</sub> (PDF card 003-038-0715). As noticed, the diffraction lines become more visible with increasing salt ratio, which supports the fact that high amount of surfactant inhibits effective calcination. However, once the salt ratio reaches to 10, the calcination product at 300 °C is mesoporous nickel oxide, see Figure 16(b). The XRD patterns can be indexed to

rock-salt NiO (PDF card -00-044-1159). All the salt ratios starting from 10 to 30, calcination at 300 °C produced the m-NiO (decoded as m-NiO-#, # is the Ni(II)/C<sub>12</sub>E<sub>10</sub> mole ratio).

In terms of morphology, both nickel hydroxide and nickel oxide showed uniform film formation. It means that morphology doesn't reflect the compositional information in the resulting films. Figure 17 shows the SEM images obtained from the mesoporous films upon calcination of Ni(II)-2 and Ni(II)-15. Both films are uniform and smooth.

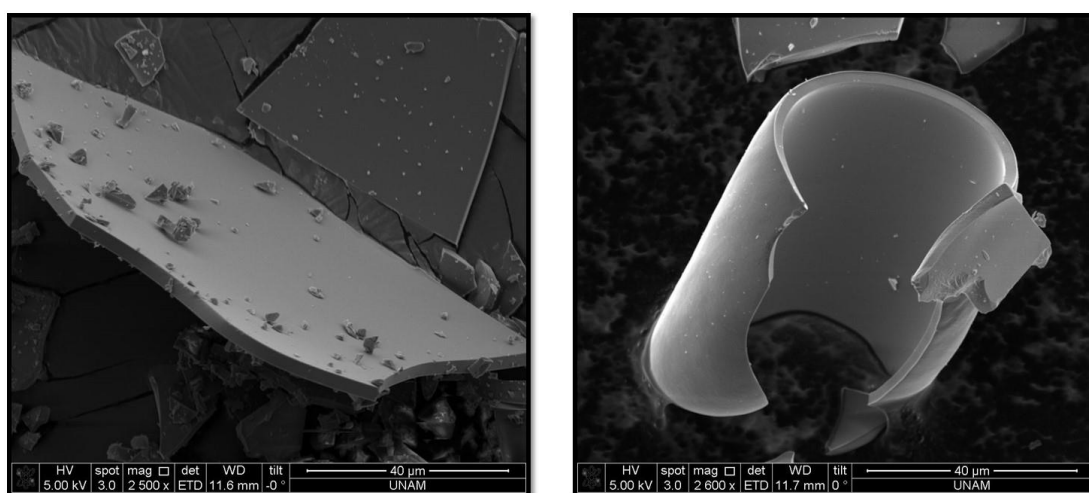


**Figure 17.** SEM images of (left) m-Ni(OH)<sub>2</sub>-2-300 and (right) m-NiO-15-300.

Since the calcination of low salt concentration samples (Ni(II)-2, Ni(II)-4, Ni(II)-6, and Ni(II)-8) at 300°C didn't produce mesoporous nickel oxide, the calcination temperature was increased to 350 °C for only those compositions to obtain the desired m-NiO. The XRD patterns of those samples are shown in Figure 18. Clearly, the calcination products are pure nanocrystalline NiO at 350 °C.

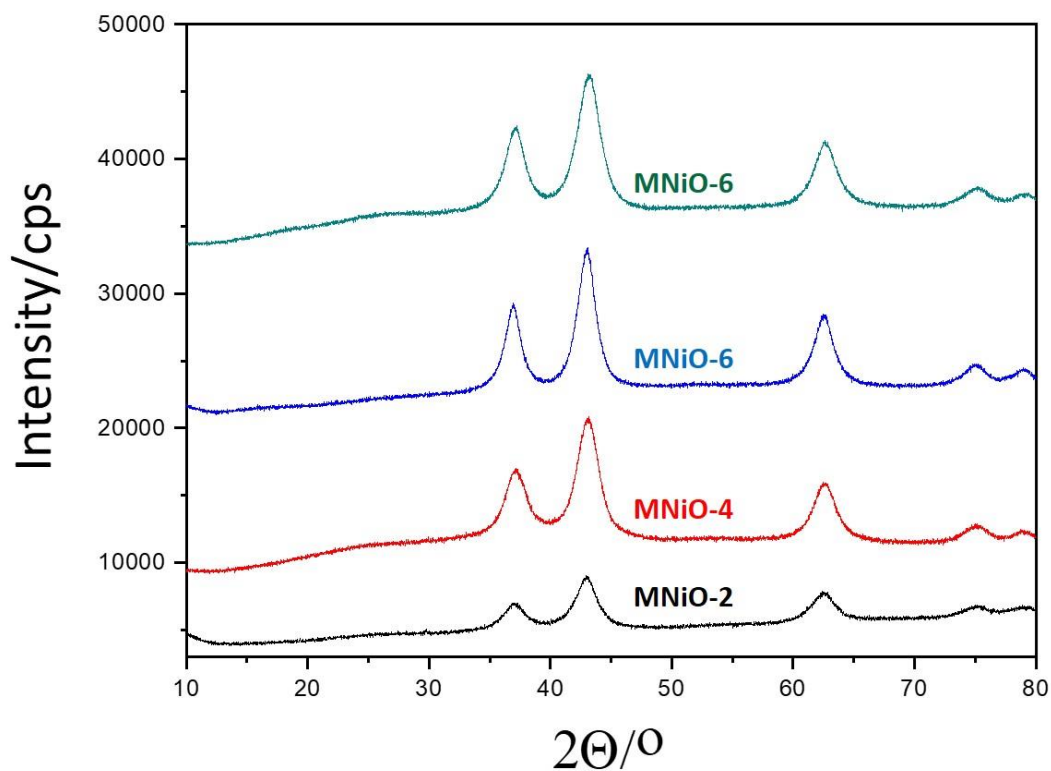


**Figure 18.** XRD patterns of the calcined samples at 350°C (bottom to top) m-NiO-2, m-NiO-4, m-NiO-6, and m-NiO-8.

Once the nickel oxide is formed, the surface area of all samples was measured using N<sub>2</sub> adsorption-desorption technique. The N<sub>2</sub>-adsorption desorption isotherms and pore size distribution plots are given in Figures 19 and 20.

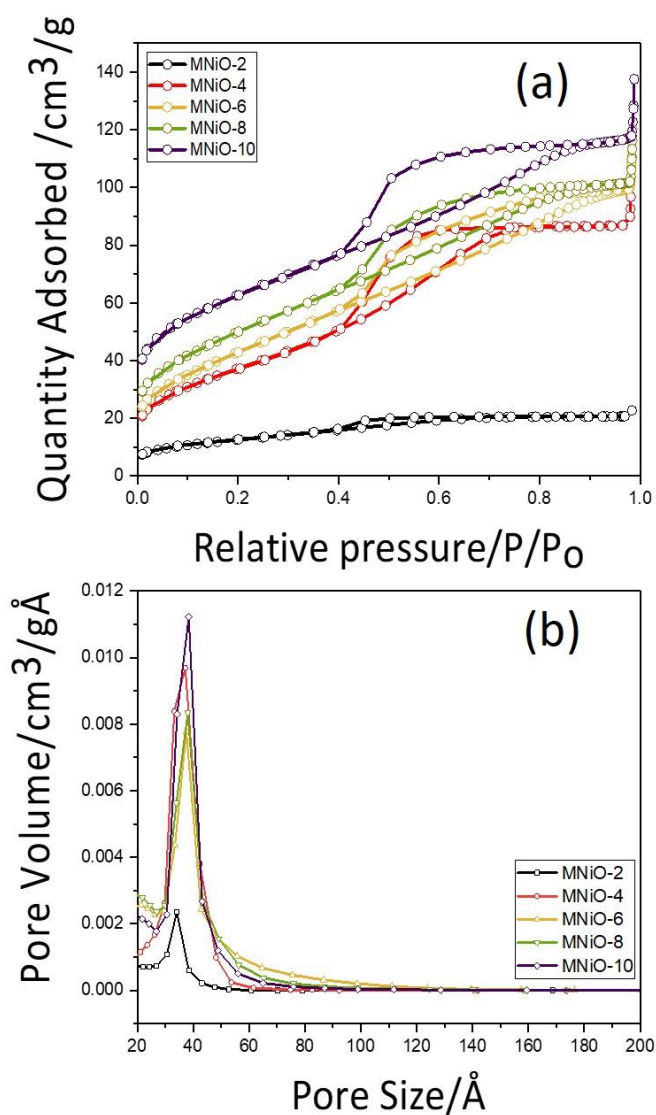


**Figure 19.** (a)  $N_2$ (77 K) adsorption desorption isotherms of m-NiO-2-350, m-NiO-4-350, m-NiO-6-350, m-NiO-8-350, and m-NiO-10-300 and (b) pore size distribution plots (obtained from the desorption branches) of m-NiO-2-350, m-NiO-4-350, m-NiO-6-350, m-NiO-8-350, and m-NiO-10-300.

Figure 19 shows the  $N_2$  adsorption-desorption isotherms and pore-size distribution plots of -NiO-2, m-NiO-4, m-NiO-6, m-NiO-8 at 350 °C, m-NiO-10, calcined at 300 °C. The isotherms are type IV and characteristic for mesoporous materials.

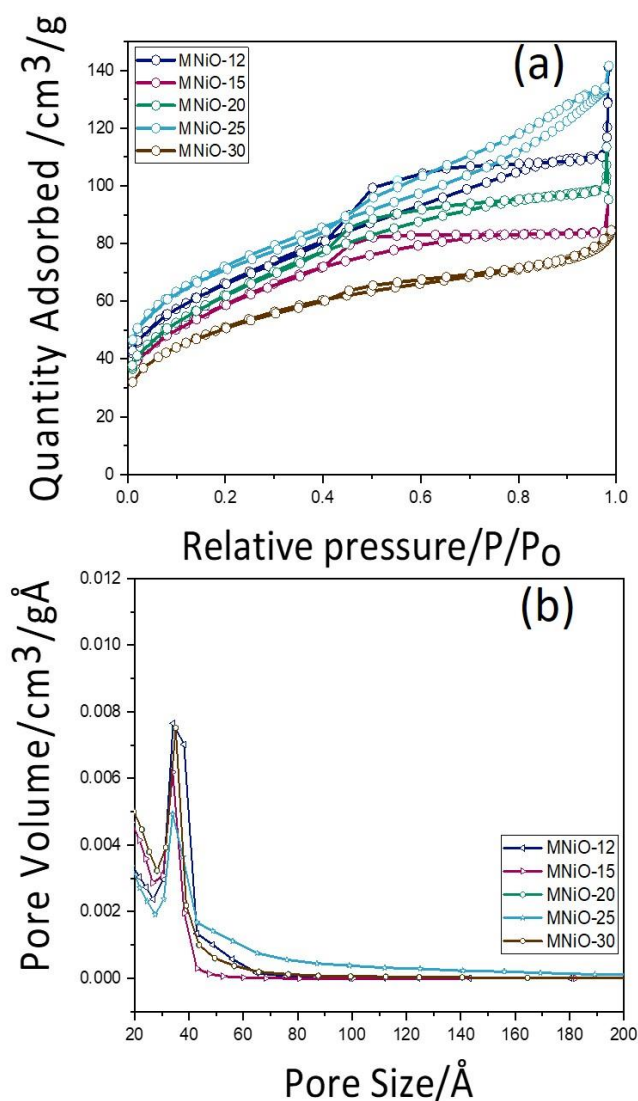


**Figure 20.** (a)  $N_2$ (77 K) adsorption desorption isotherms of m-NiO-12-300, m-NiO-15-300, m-NiO-20-300, m-NiO-25-300, and m-NiO-30-300 and (b) pore size distribution plots (obtained from the desorption branches) of m-NiO-12-300, m-NiO-15-300, m-NiO-20-300, m-NiO-25-300, and m-NiO-30-300.

Figure 20 shows the  $N_2$  adsorption-desorption isotherms and pore-size distribution plots of m-NiO-12, m-NiO-15, m-NiO-20, m-NiO-25, and m-NiO-30, calcined at 300 °C. All the samples showed typical type-IV isotherms of the mesoporous materials. Among all analyzed samples, the m-NiO-2 showed least uniform pore size distribution. As the surfactant to salt ratio is quite high in this case, the surfactant might not be burned out efficiently and the pores are likely partially blocked by unburned surfactant species. All the other samples displayed quite uniform pore size

distributions. All the surface area, pore size, and pore volume data are listed in Table 3.

The m-NiO-2-350 has the lowest surface area of 45 m<sup>2</sup>/g among all analyzed samples. The highest salt ratio sample, m-NiO-25-300, displayed the highest surface area of 257 m<sup>2</sup>/g. However, to pick the most suitable sample for further analysis not only surface area has to be considered but also the pore volume and pore size distribution needs to be considered. Accordingly, the m-NiO-10-300 showed a quite high surface area of 223 m<sup>2</sup>/g and the most uniform pore size distribution compared to the other compositions. In addition, the pore volume of m-NiO-10 is the largest with a pore size of 3.6 nm at 300 °C. So that the 10-mole ratio sample is considered to be the optimum composition.

**Table 3.** N<sub>2</sub> (77K) adsorption-desorption data of m-NiO-#-XXX samples (# is Ni/C<sub>12</sub>E<sub>10</sub> mole ratio and XXX is calcination/annealing temperature in Celsius).

Sample	BET Surface Area (m <sup>2</sup> /g)	BJH Pore Volume (cm <sup>3</sup> /g)	BJH Pore Size (nm)
m-NiO-2-350	45	0.022	3.4
m-NiO-4-350	136	0.146	3.5
m-NiO-6-350	158	0.180	3.7
m-NiO-8-350	182	0.167	3.7
m-NiO-10-300	223	0.182	3.6
m-NiO-12-300	237	0.178	3.6
m-NiO-15-300	213	0.091	3.4
m-NiO-20-300	225	0.145	3.5
m-NiO-25-300	257	0.155	3.5
m-NiO-30-300	183	0.091	4.1

### 3.4. Optimization of Calcination Temperature

Once the salt concentration is optimized, the m-NiO-10 has been chosen to be characterized further. The effect of calcination temperature on the composition, surface area, and particle size must be investigated. Photos of the calcined samples at different temperatures starting from 250 to 500 °C are shown in Figure 21

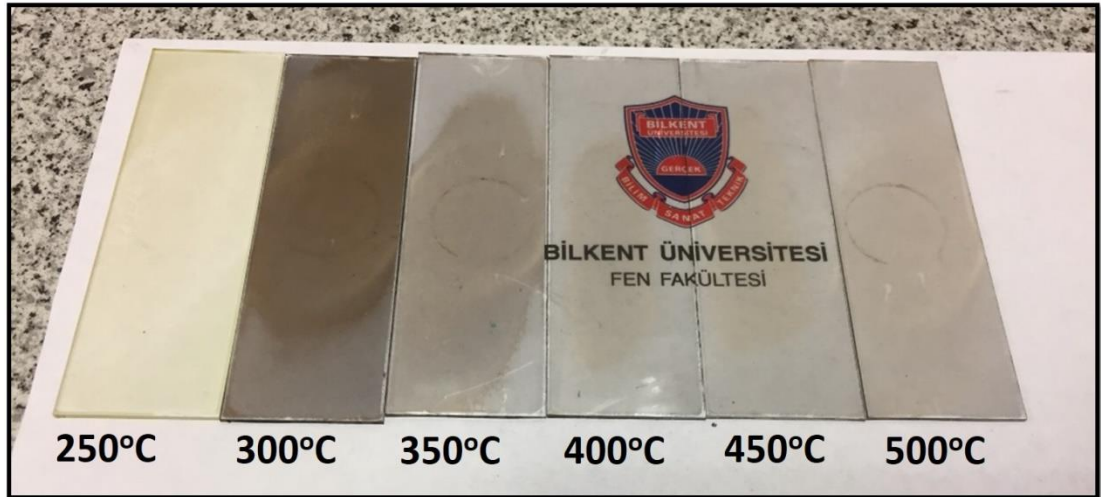


**Figure 21.** Photos of the m-NiO-10 thin films obtained after calcination at different temperatures starting from 250 to 500°C (left to right).

Colors of the resulting film are changing at each step of annealing temperature, which indicate the change in the composition or morphology of the materials. The PXRD patterns, obtained at different temperatures are shown in Figure 22.

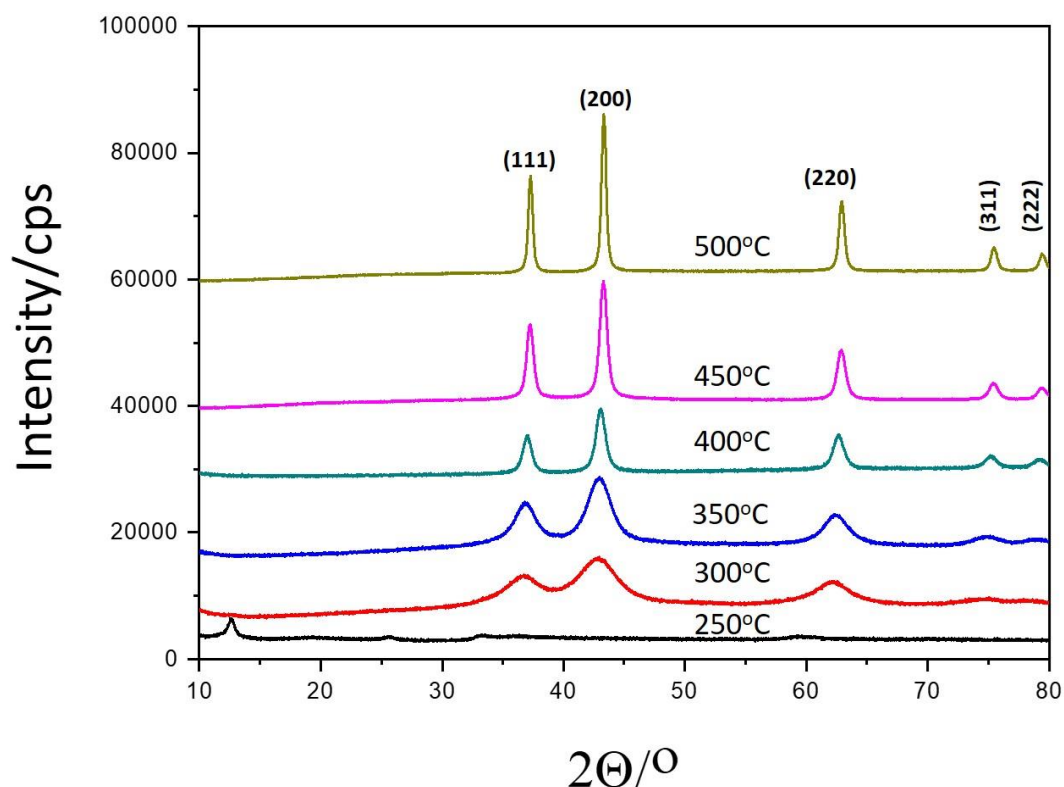


**Figure 22.** XRD patterns of the m-Ni-10-250, m-NiO-10-300, m-NiO-10-350, m-NiO-10-400, m-NiO-10-450, and m-NiO-10-500, bottom to top.

As shown in Figure 22, at 250 °C, the nickel oxide didn't form. These lines have been indexed in previous sections and assigned to  $\alpha$ -Ni(OH)<sub>2</sub>. Once the calcination temperature reaches to 300 °C, the mesoporous nickel oxide forms. Then the all diffraction lines are indexed and belong to the rock salt NiO. The mesoporosity of the m-NiO-10-300 was confirmed by using N<sub>2</sub>-adsorption desorption technique in previous section. All the diffraction lines are quite broad, indicating that the particles are nanocrystalline and/or pore-walls are made up of small crystallites. With increasing calcination temperature, the diffractions lines get sharper, it means that the crystals are growing. Particle size could be calculated from the (220) line, using Scheerer formula [101] for particle size calculation:  $D = (0.94x\lambda)/(\beta x \cos\theta)$  where, D - average crystallite size,  $\beta$  - full width half maximum of the diffraction line in radians,  $\theta$  - Bragg's angle,  $\lambda$  - x-ray wavelength (1.54056 Å). The data for temperature dependent particle size is summarized in Table 4.

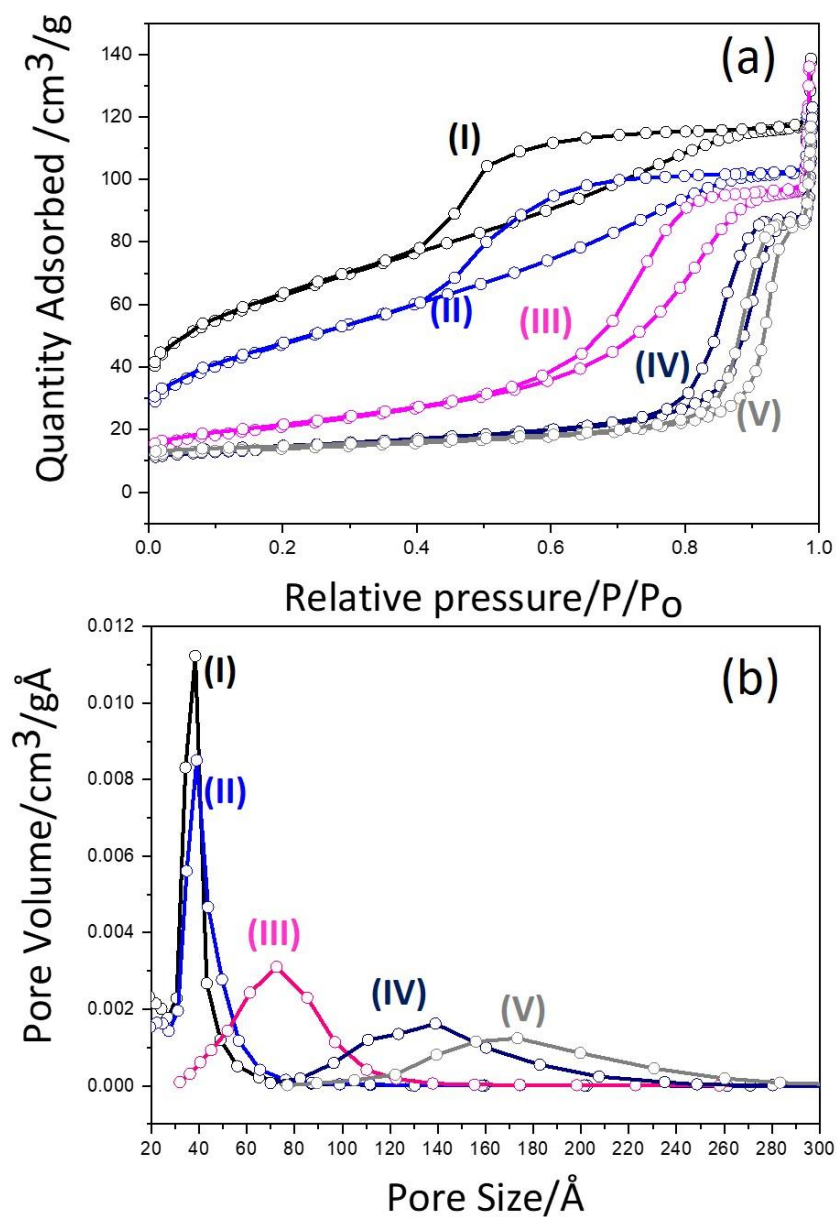
**Table 4.** Particle size of m-NiO-#-XXX samples (XXX is calcination/annealing temperature in Celsius).

Sample	Particle size (nm)
m-NiO-10-300	2.9
m-NiO-10-350	4.5
m-NiO-10-400	11.4
m-NiO-10-450	15.1
m-NiO-10-500	27.2

As tabulated in Table 4, the particle size at 300 °C is 2.9 nm, and when the calcination temperature increased to 500 °C the particle size increases almost ten times and reaches to 27.2 nm.

**Table 5.** N<sub>2</sub>(77K) adsorption-desorption data of m-NiO-#-XXX samples (XXX is calcination/annealing temperature in Celsius).

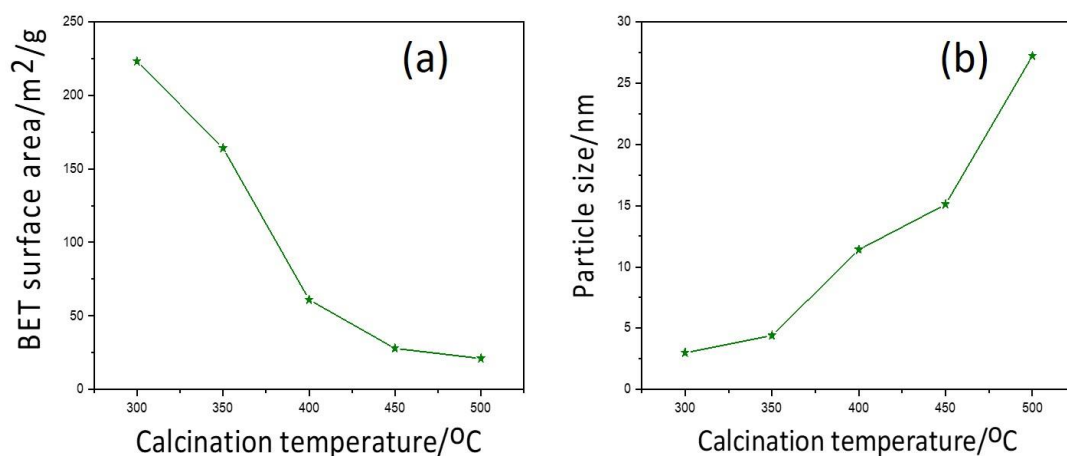
Sample	BET Surface Area (m <sup>2</sup> /g)	BJH Pore Volume (cm <sup>3</sup> /g)	BJH Pore Size (nm)
m-NiO-10-300	223	0.182	3.6
m-NiO-10-350	164	0.176	4.1
m-NiO-10-400	61	0.204	7.2
m-NiO-10-450	28	0.180	13.4
m-NiO-10-500	21	0.167	16.9



**Figure 23.** (a) N<sub>2</sub>(77 K) adsorption-desorption isotherms and (b) pore size distribution of (I) m-NiO-10-300, (II) m-NiO-10-350, (III) m-NiO-10-400, (IV) m-NiO-10-450, and (V) m-NiO-10-500.

The crystallite size data were supported by temperature dependent N<sub>2</sub>-adsorption-desorption data. The temperature dependent N<sub>2</sub> adsorption-desorption isotherms and pore size distribution plots for m-NiO-10 are shown in Figure 23. The surface area and pore size information are presented in Table 5. The N<sub>2</sub> adsorption-desorption

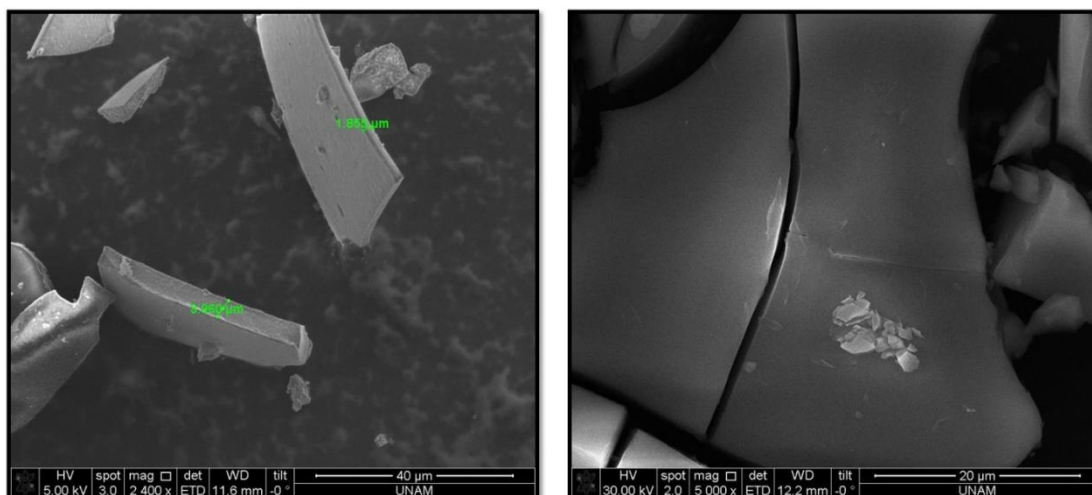
isotherms are type-IV, characteristic for mesoporous materials at all calcination temperatures. It is clear from the pore size distribution plots that as the pore size expands due to temperature increase, the pores become less uniform. The surface area drops from 223 m<sup>2</sup>/g at 300 °C to 23 m<sup>2</sup>/g at 500 °C. The surface area decreased almost ten times, which is in good agreement with the particle size obtained from the XRD data. The pore size also changed accordingly from 3.6 nm at lowest calcination temperature to 16.9 nm at highest calcination temperature.



**Figure 24.** Correlation of BET surface area and particle size: (a) surface area change with temperature and (b) particle size change with temperature.

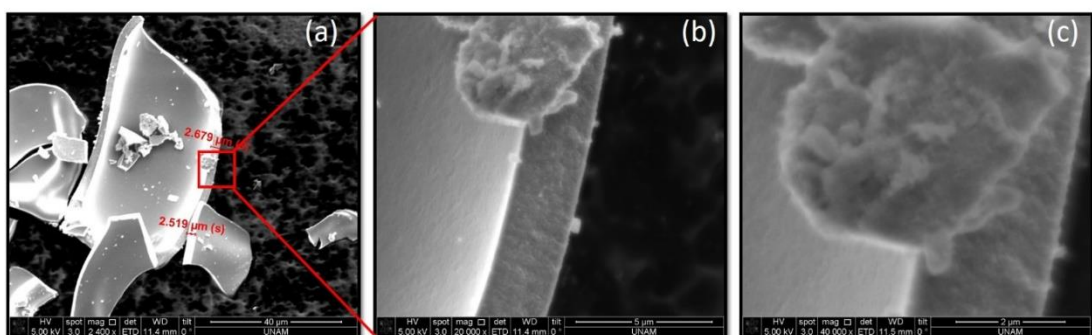
With increasing of the annealing temperature, the pore-walls grow, and the pores expand, as a result the particle-size increases with decreasing surface area. This correlation is summarized in Figure 24, where the temperature dependence of surface area and particle size are shown.

In terms of morphology, every sample showed uniform film formation and even some porosity are visible at higher magnifications in the SEM images. The SEM images of m-Ni-10-250, m-NiO-10-300, m-NiO-10-350, m-NiO-10-400, m-NiO-10-450, and m-NiO-10-500 are shown in Figures 25, 26, and 27.



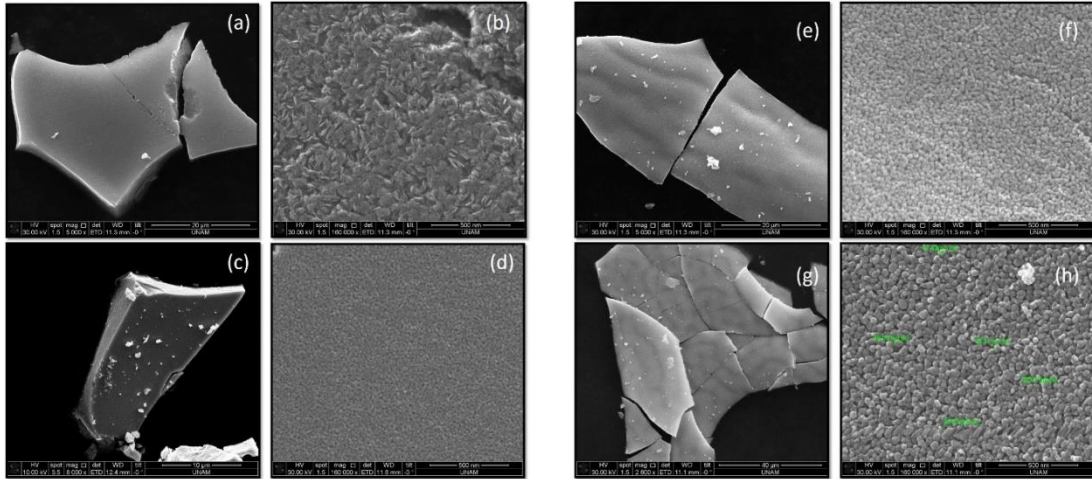
**Figure 25.** SEM images of m-Ni-10-250 at different magnifications, scale bars are (left) 40  $\mu\text{m}$  and (right) 20  $\mu\text{m}$ .

Figure 25 and 26 show the SEM images of m-Ni-10-250 and m-NiO-10-300, respectively, showing that even nickel hydroxide possesses the same film morphology as nickel oxide.



**Figure 26.** SEM images of m-NiO-10-300 at different magnifications, scale bars are (a) 40  $\mu\text{m}$ , (b) 5  $\mu\text{m}$  and (c) 2  $\mu\text{m}$ .

As the calcination temperature is increased, the mesoporous nickel oxide forms. Figure 27 shows a series as SEM images of NiO calcined at different temperature and displays a uniform film morphology at all temperatures. The samples calcined over 450  $^{\circ}\text{C}$  also show uniform pores in the films at high magnifications, see Figure 27.



**Figure 27.** SEM images of (a) m-NiO-10-350 (scale bar is 20  $\mu\text{m}$ ), (b) m-NiO-10-350 (scale bar is 500 nm), (c) m-NiO-10-400 (scale bar is 10  $\mu\text{m}$ ), (d) m-NiO-10-400 (scale bar is 500 nm), (e) m-NiO-10-450 (scale bar is 20  $\mu\text{m}$ ), (f) m-NiO-10-450 (scale bar is 500 nm), (g) m-NiO-10-500 (scale bar is 40  $\mu\text{m}$ ), and (h) m-NiO-10-500 (scale bar is 500 nm).

Figure 27 shows the SEM images of m-NiO-10-350, m-NiO-10-400, m-NiO-10-450, and m-NiO-10-500 at different magnifications. Uniform film morphology is preserved at high calcination temperatures. As shown at a high magnification (scale bar 500 nm), the films are consisting of small uniform nanoparticles with a porosity. It is clear from the images that the grain size grows from 400 to 500  $^{\circ}\text{C}$ , which support the BET and XRD data. For more detailed morphology information and to visualize the porosity, the TEM images were also recorded. The TEM images of the films prepared at different calcination temperatures are shown in Figure 28.

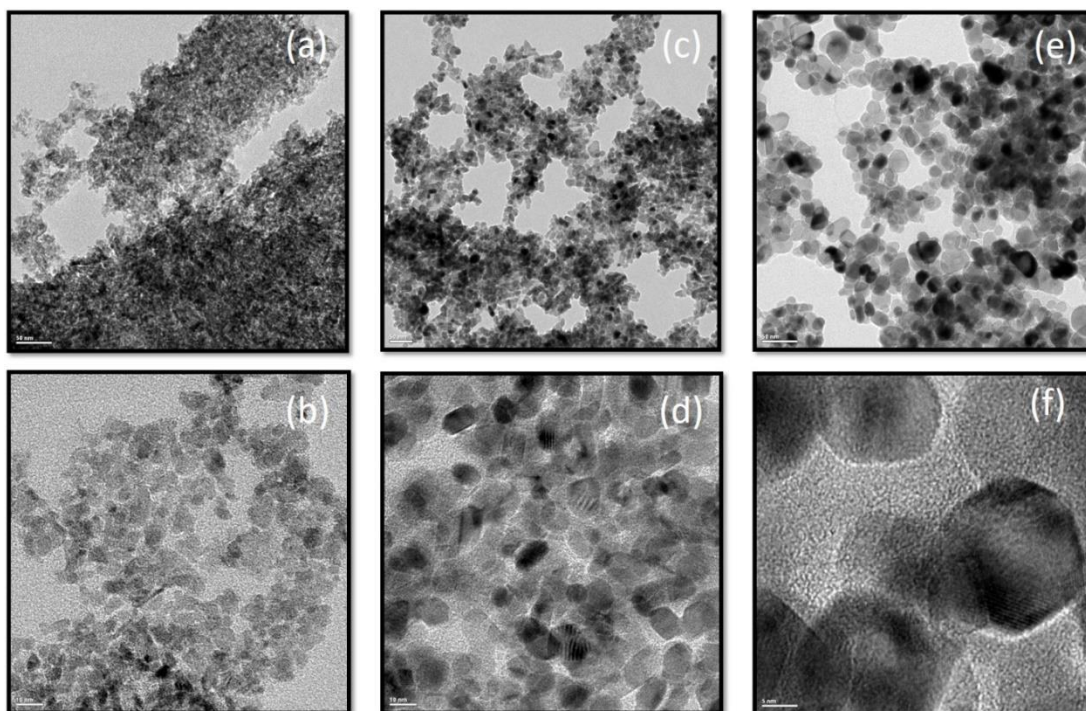


**Figure 28.** TEM images of (a) *m*-NiO-10-300 (scale bar is 50 nm), (b) *m*-NiO-10-300 (scale bar is 10 nm), (c) *m*-NiO-10-400 (scale bar is 50 nm), (d) *m*-NiO-10-400 (scale bar is 10 nm), (e) *m*-NiO-10-500 (scale bar is 50 nm), and (f) *m*-NiO-10-500 (scale bar is 5 nm).

The TEM images of *m*-NiO-10-300, *m*-NiO-10-400, and *m*-NiO-10-500 at different magnifications are shown in Figure 28. It is clear from the images that the samples show porosity and its size can be controlled by the calcination/annealing temperature. In addition, the TEM images also support the BET, XRD and SEM data. However, much thinner sample must be produced to observe the porosity, particle size and uniform film morphology in the TEM images. Note that above images were obtained by grinding thicker films. That is why the images show a loss of film integrity in the samples, see Figure 26.

### 3.5. Stability of Ni(II)/C<sub>12</sub>E<sub>10</sub> Solutions

As the surfactant to nickel salt ratio and calcination temperature were optimized, the stability of precursor solution and stability of gel mesophase are needed to be investigated to show the effect of aging of solution and mesophase on resulted products morphology, surface properties, and crystallinity. Fresh samples were

already calcined, and the corresponding data have been explicitly described in the previous sections.

For this analysis, the precursor solution of  $10\text{Ni(II)/C}_{12}\text{E}_{10}$  was prepared and kept under the constant stirring for one month. Then sample was drop coated on a glass slide and annealed immediately for 1 hour at  $300\text{ }^{\circ}\text{C}$ . Another sample was prepared from fresh precursor solution of  $10\text{Ni(II)/C}_{12}\text{E}_{10}$ , drop coated on a surface of a glass slide and kept for 1 week in the lab conditions in the gel phase. After that, the samples were calcined at  $300\text{ }^{\circ}\text{C}$  for 1 hour. Both samples were analyzed using powder XRD and  $\text{N}_2$  adsorption-desorption techniques. The XRD patterns are shown in Figure 29.

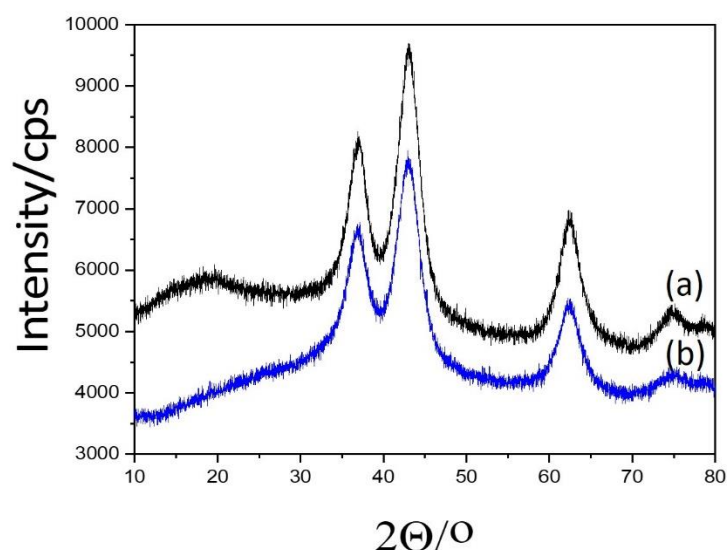


**Figure 29.** XRD patterns of the m-NiO-10-300 from (a) aged gel and (b) aged solution.

As shown in Figure 29, the products that formed are pure nickel oxide. There is no difference in the linewidths in all diffraction lines, indicating that the particle sizes are the same in both samples. To support the XRD data, the  $\text{N}_2$  adsorption-desorption isotherms and pore size distribution plots are shown in Figure 30, and the BET surface areas are given in Table 6.

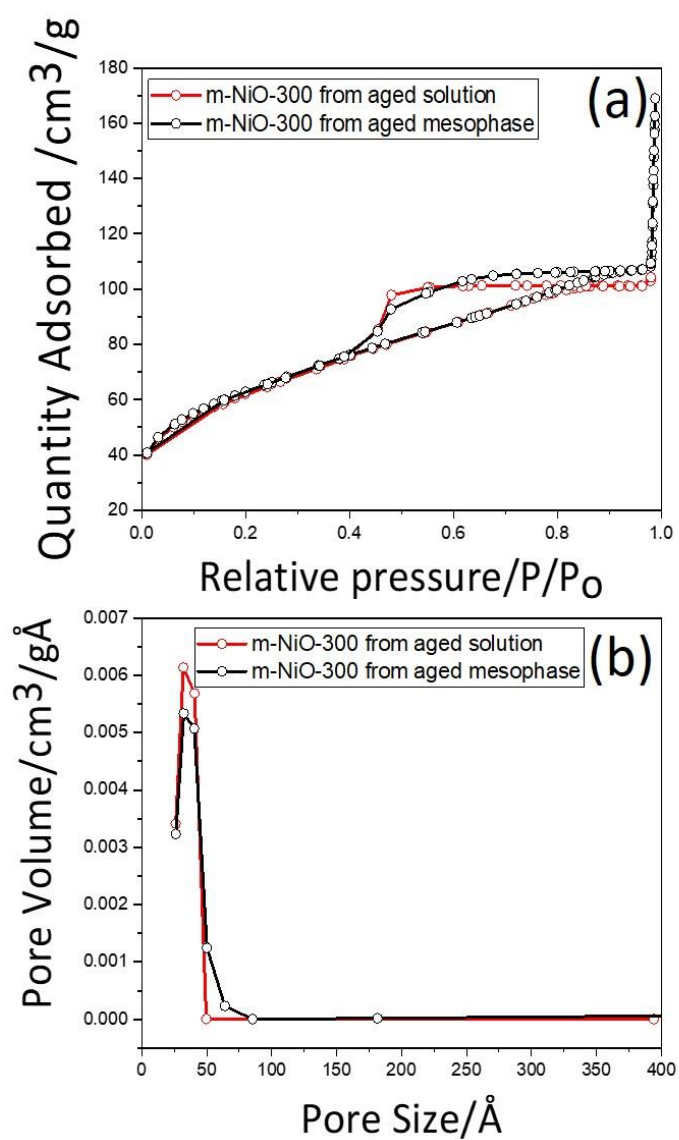


**Figure 30.** (a)  $N_2(77\text{ K})$  adsorption-desorption isotherms and (b) pore size distribution of m-NiO-10-300 from aged mesophase and m-NiO-10-300 from aged solution.

**Table 6.** N<sub>2</sub>(77K) adsorption-desorption data of m-NiO-10-300 from aged mesophase and aged solution.

Sample	BET Surface Area (m <sup>2</sup> /g)	BJH Pore Size (nm)
m-NiO-10-300 from aged mesophase	223	3.6
m-NiO-10-300 from aged solution	221	3.4

As shown in the N<sub>2</sub> adsorption-desorption isotherms above, the given isotherms are type-IV, characteristic for mesoporous materials in both samples. Both samples have almost the same surface area of 223 and 221 m<sup>2</sup>/g and pore sizes of 3.6 and 3.4 nm for *m*-NiO-10-300 from aged mesophase and *m*-NiO-10-300 from aged solution, respectively. The pore size distribution plots also support the given data as both samples have uniform pore size distribution. Therefore, this can be summarized that aging of Ni(II)/C<sub>12</sub>E<sub>10</sub> system in a precursor solution form or in gel mesophase form does not have significant effect on the morphology, porosity, and crystallinity of resulted mesoporous nickel oxide.

### 3.6. Electrochemical Characterization of Mesoporous Nickel Oxide

To better understand properties of the mesoporous nickel oxide, electrochemical characterization was done using *m*-NiO-10 thin films coated over FTO coated glass using cyclic voltammetry (CV) technique in an alkali media (1M KOH aqueous solution).

600 CVs were recorded using the *m*-NiO-10 electrodes, prepared at 300, 350, 400, 450, and 500 °C. 2<sup>nd</sup> and 600<sup>th</sup> cycles of each electrode are shown in Figure 31.

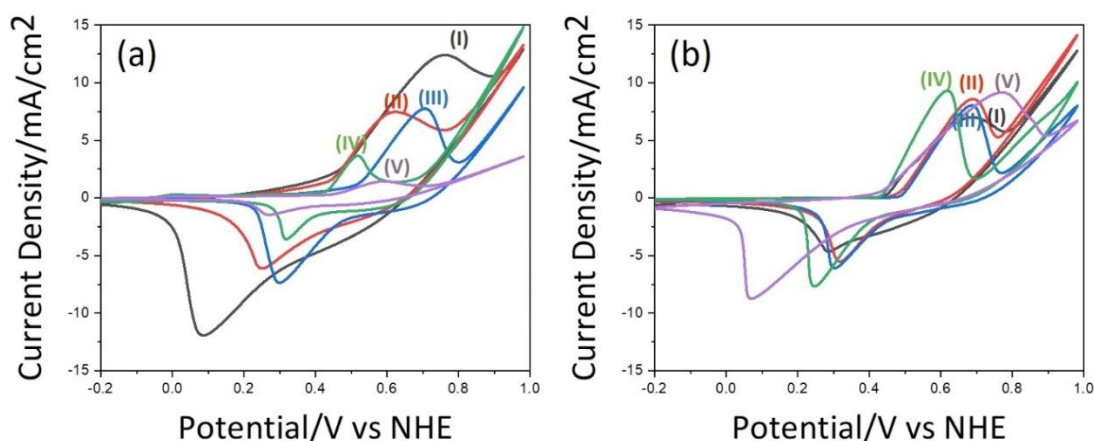


**Figure 31.** (a) 2<sup>nd</sup> CV and (b) 600<sup>th</sup> CV of m-NiO-10 electrodes calcined at (I) 300, (II) 350, (III) 400, (IV) 450 and (V) 500 °C.

-0.2 to 1.0 V potential windows were used in the CV cycles. As shown in Figure 31(a), the 2<sup>nd</sup> CVs of all samples with decreasing calcination temperature, the peak current is also decreasing and shifting to a more negative voltage value. It means that the peak current is sensitive to a change of annealing temperature. The electrode prepared as 300 °C has an oxidation peak current density of around 12 mA/cm<sup>2</sup> and a voltage value of 0.7 V, while the electrode at 500 °C had an oxidation peak current density of about 4 mA/cm<sup>2</sup> and voltage value of 0.5 V. This difference is consistent with the change of the surface areas in these two electrodes with temperature and increased crystallinity. As the high surface area will provide more active sides, its current density should also be much higher.

However, not only the annealing temperature changes electrochemical behavior of these electrodes, also they are changing upon cycling, as shown in Figure 31(b). Upon several hundreds of CV measurements, almost all the samples, calcined at different temperatures, reach the same current densities of around 10 mA/cm<sup>2</sup>, even though voltage values are fluctuating without showing any trend. It means that, the surface of the samples is changing with cycling, even though BET surface area is very different.

To more clearly show the temperature and number of cycle dependence of CVs, the number of scans versus peak current from each electrode was plotted, see Figure 32.

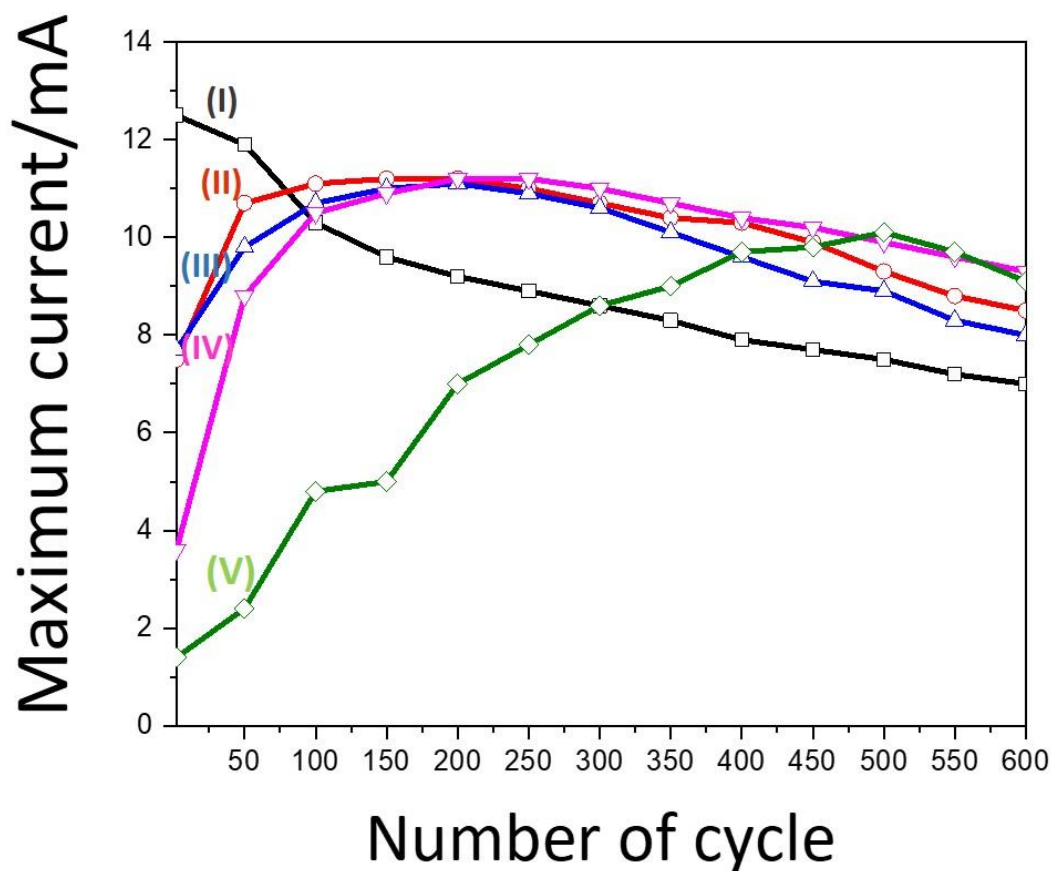


**Figure 32.** Overall change in peak current at around 0.6 V over cycling of electrodes prepared at (I) 300, (II) 350, (III) 400, (IV) 450 and (V) 500 °C.

The electrode prepared at 300 °C, having the highest surface area (see previous sections), shows the highest oxidation peak current in the 2<sup>nd</sup> till 5<sup>th</sup> cycle (around 12 mA/cm<sup>2</sup>), then upon further cycling, activity of this electrode decreases as peak currents dropped to 7 mA/cm<sup>2</sup>. This behavior can be explained by stability of the electrode at 300 °C. Even though, 300 °C is high enough temperature to form nickel oxide, it is not enough to be properly attached to FTO surface, so with time, the electrode is getting destroyed in electrolyte solution, which affects peak current values. If one pays attention to another extreme, the electrode annealed at 500 °C with the least surface area, in the first 50 cycles it has peak current density of around 2 mA/cm<sup>2</sup>, however upon further cycling, the current density shoots up and reaches to a 10 mA/cm<sup>2</sup> at 600<sup>th</sup> cycle. As it was already mentioned above, with cycling the

number of active sites is increasing over time and the surface area doesn't play a huge role. Note also that the electrode annealed at 500 °C is more crystalline sample and has larger pores, which may allow a better electrolyte to contact and better conductivity. As for other electrodes prepared at 350, 400 and 450 °C, being more crystalline compared to the electrode calcined at 300 °C and having more surface area compared to 500°C, all of them display similar behavior having 10, 9 and 7 mA/cm<sup>2</sup>, respectively, in the first 50 cycles and reach to a 10 mA at 600<sup>th</sup> cycle. Even though, at the end of the 600<sup>th</sup> cycle, a clear surface area dependence on the peak current density disappears. With cycling, the electrode surface constantly changes because of the effect of applied voltage and the pH of electrolyte (see later). CVs shown in Figure 33 give a more detailed information about the electrochemical behavior of the m-NiO electrodes.

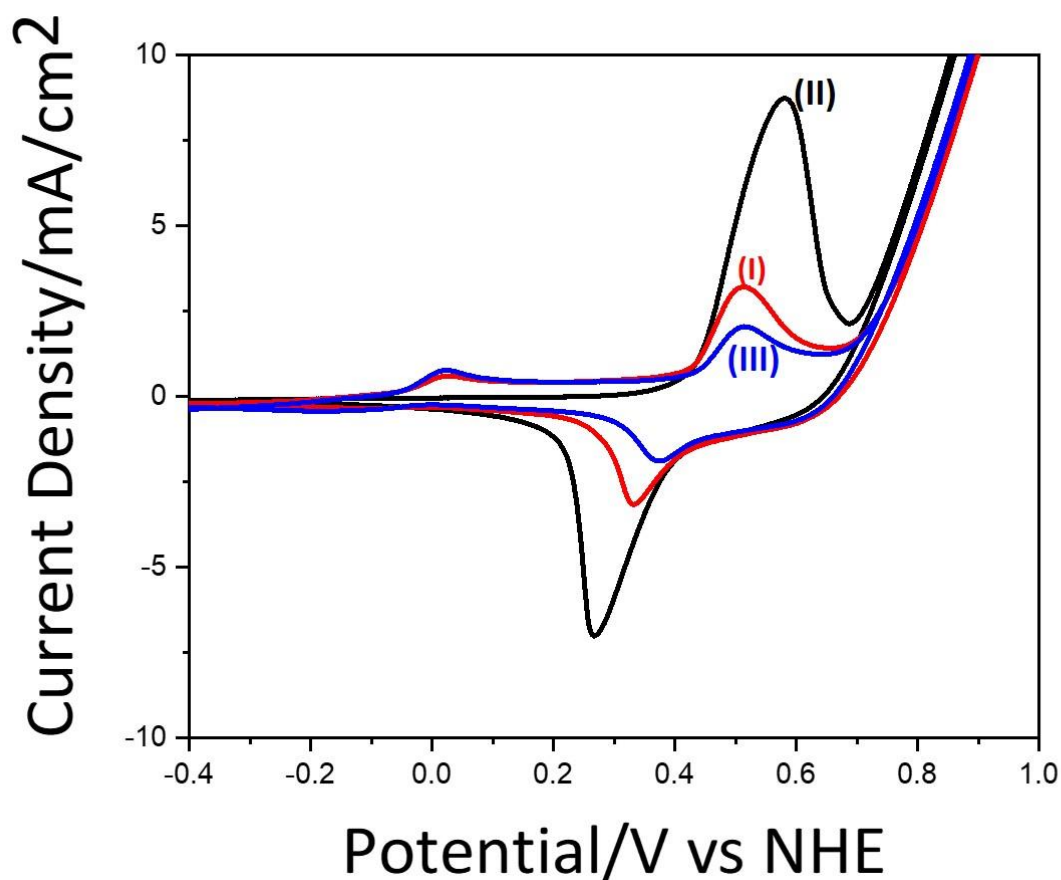


**Figure 33.** CVs of the m-NiO-10-400 (I) 1<sup>st</sup> and (II)50<sup>th</sup>, and (III) 1<sup>st</sup> cycle after recalcination of (II).

The oxidation peak at around 0 V appears right after the calcination of the electrode, however after 50<sup>th</sup> cycles this peak disappears, showing that the surface species are changing with each cycle. However, after recalcining the cycled electrode at its annealing temperature, this peak reappears in the CV with the same or higher intensity, compare CVs in Figure 31. It means that, whatever the chemical change is happening on the electrode surface can be reversed to the initial state by simply annealing it. So, this peak was assigned to oxidation of NiO. There are also weaker signals between 0.0 and 0.4 V, likely due to oxidation of the NiO surface species. As for the oxidation peak around 0.5 V, it shoots up to the highest current density from 4 mA/cm<sup>2</sup> at first cycle to 8 mA/cm<sup>2</sup> at 50<sup>th</sup> cycle, that also supports the fact that electrode is getting more active upon cycling. Based on this observation, this peak

was assigned to oxidation of  $\text{Ni}(\text{OH})_2$ . When the  $\text{NiO}$  surface species are converted into  $\text{Ni}(\text{OH})_2$  species, those species don't reduce back to oxide species but oxidized to  $\text{NiOOH}$  species.

To support this proposal, a CV of  $\text{Ni}(\text{OH})_2$ , prepared at  $250\text{ }^\circ\text{C}$  is also recorded, see Figure 34. Notice that the electrode composition at  $250\text{ }^\circ\text{C}$  is  $\text{Ni}(\text{OH})_2$ .

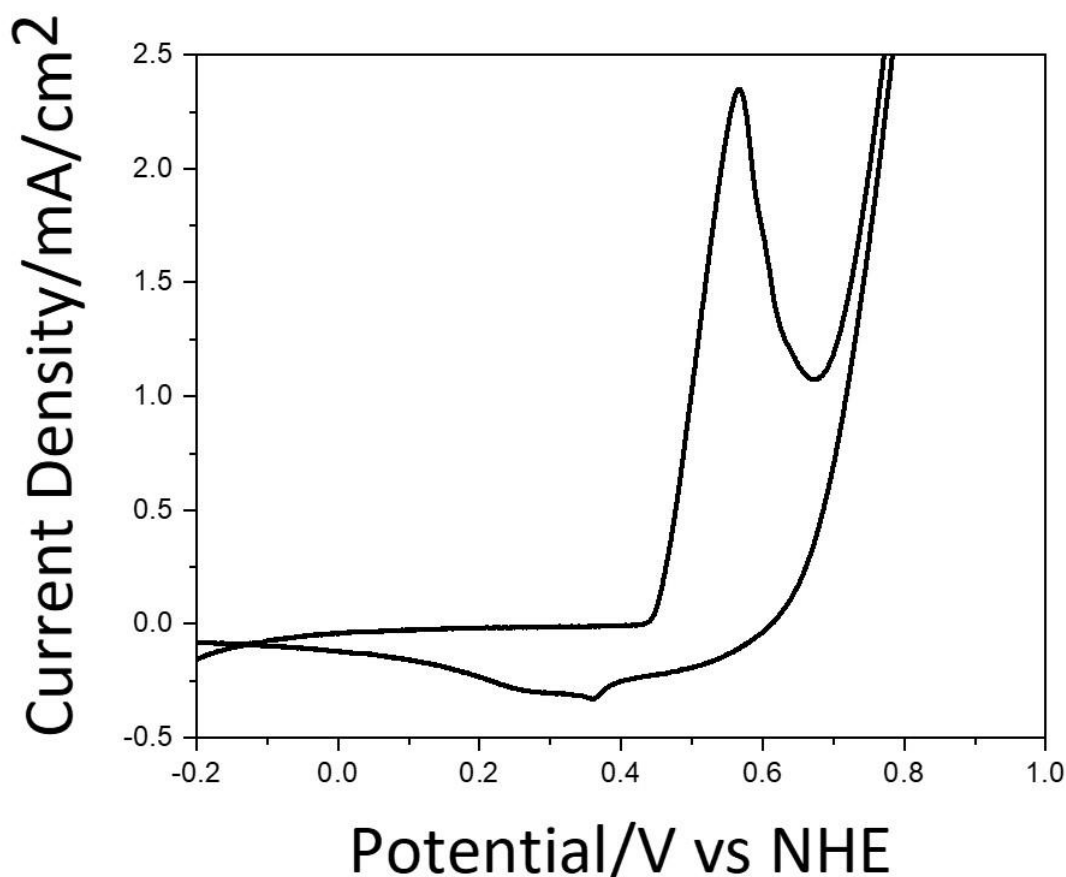


**Figure 34.** CV of  $\text{Ni}(\text{OH})_2$  prepared at  $250\text{ }^\circ\text{C}$ .

There is no oxidation peak at around 0, as that peak belongs to nickel oxide, which supports our above proposal. Clearly, the only oxidation peak is observed at around 0.5 V, which was already assigned to the oxidation of  $\text{Ni}(\text{OH})_2$ . Oxidation and reduction peak separation (see Figure 33) upon cycling can be explained by chemical change of the surface species. After first cycle, the reduced species are no longer

nickel oxide, further cycling takes place between nickel hydroxide and nickel oxyhydroxide species, as schematically shown in Figure 35.

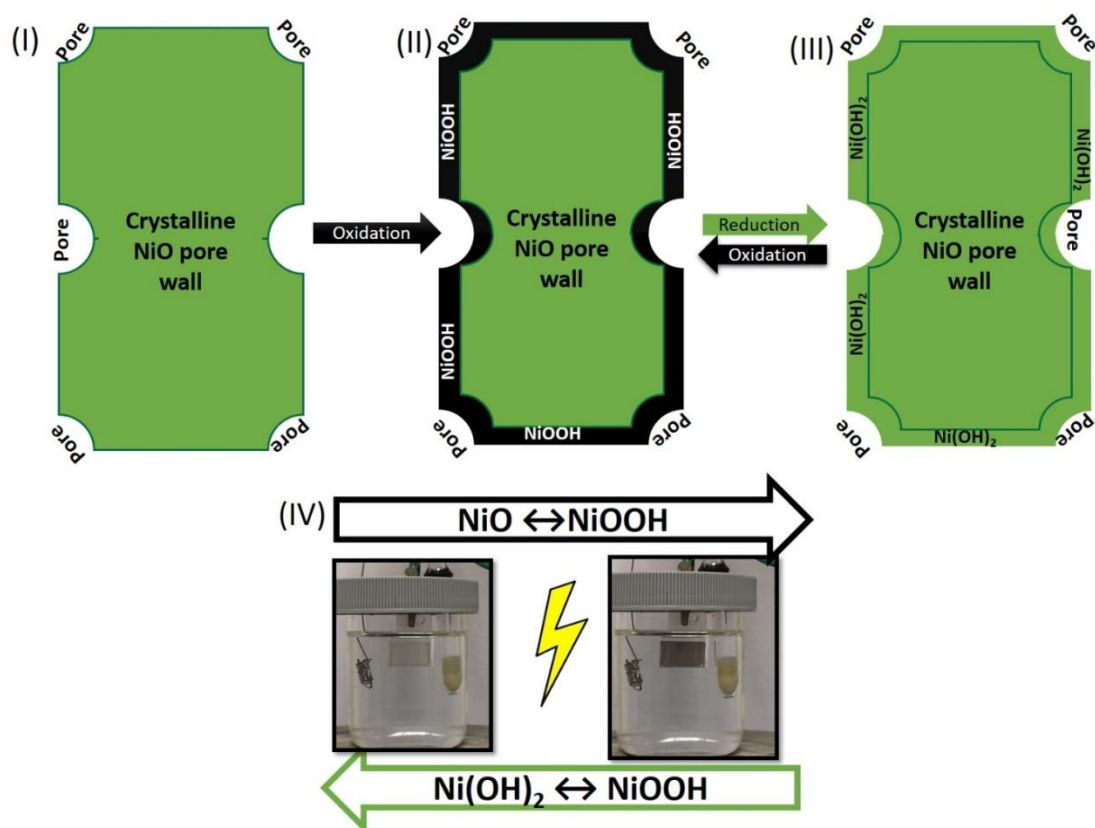


**Figure 35.** Schematic representation of the mesoporous NiO before and after oxidation-reduction cycles with surface composition: (I) NiO surface before cycling, (II) NiO with NiOOH on the surface (black color), (III) NiO with Ni(OH)<sub>2</sub> on the surface (green color), (I) Schematic representation of electrochemical cell with NiO electrode before and after CV.

To further support that all the electrochemical processes are happening only on the surface of the electrode, the powder XRD patterns of a sample annealed at 400 °C were recorded before and after cycling experiment (after 1000 CVs).

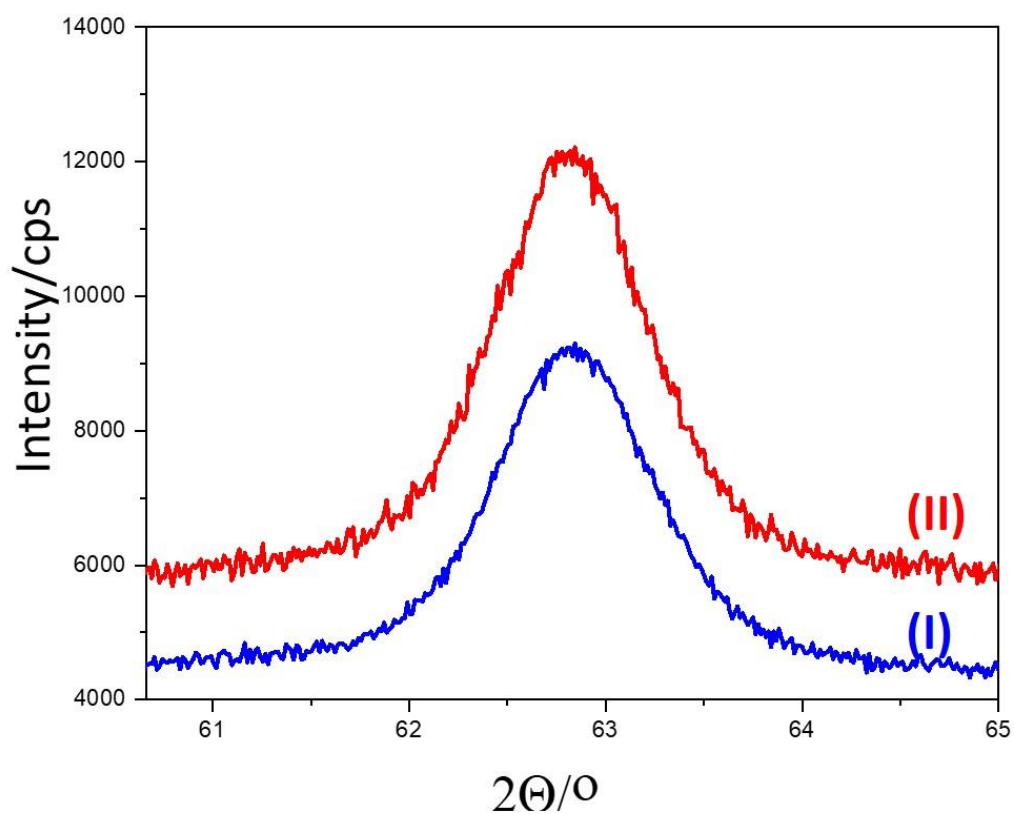


**Figure 36.** 220 XRD line of m-NiO-10-400 (I) before and (II) after 1000 CVs.

Figure 36 clearly shows that no peak broadening occurs after 1000 cycles. This indicates that a transformation from  $\text{Ni}(\text{OH})_2$  is happening only at very top surface of m-NiO and to some extent without etching crystalline pore wall (see Figure 35), or the change cannot be detected by the XRD technique.

So, to identify the surface species, XPS spectra of the samples before and after CV measurements were also recorded, see Figure 37.

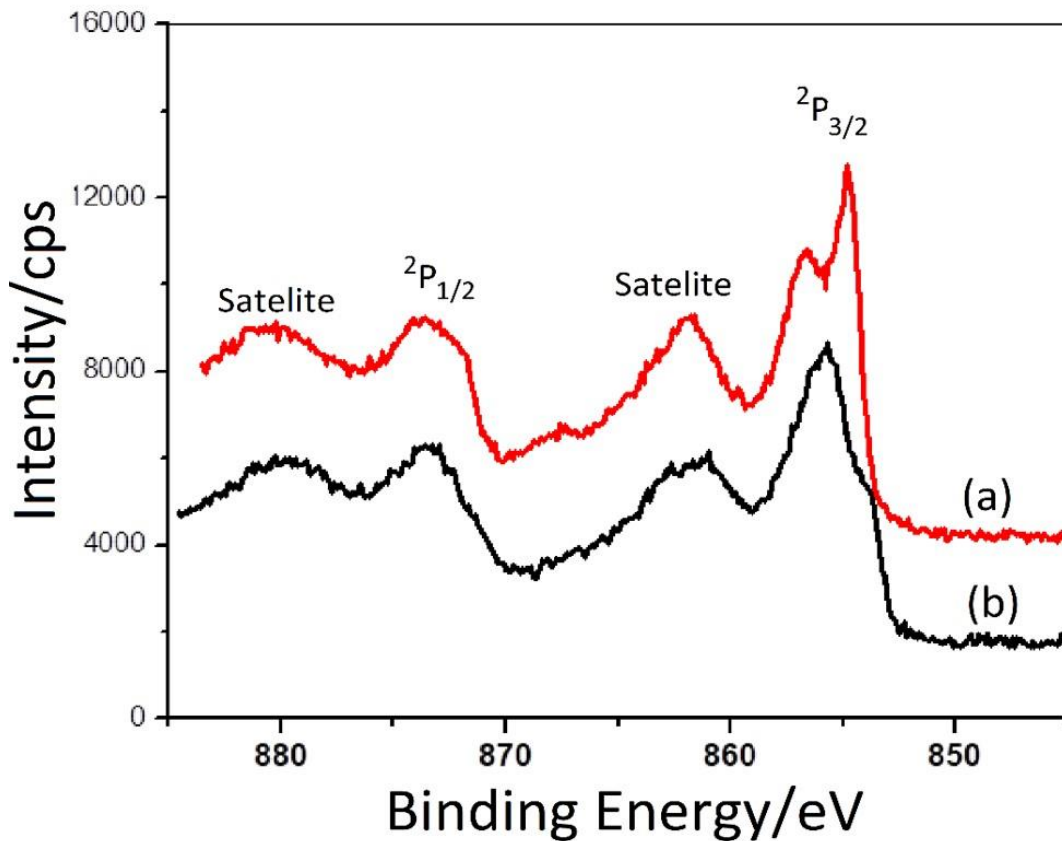


**Figure 37.** XPS spectra of m-NiO (a) before and (b) after CV (1000 cycle).

It is clear from the data that the fresh sample, not exposed to electrocatalytic use, shows 2p ( $2P_{3/2}$  component) peaks at 854 and 856 eV. And they are assigned to different NiO surface species. It is understandable, as this sample was not used yet to form other species apart from nickel oxide. When the electrode is exposed to electrochemical use like 1000 CVs, the surface is clearly changed as that color of the electrode is also changed (see Figure 35), so it is expected that oxidation products form on the surface, and a drastic change is observed in the spectrum after 1000 CVs. New peaks appear at 854 and 855.7 eV. The higher energy peak appears with a higher intensity, so it can be assumed that the new surface species like NiOOH and Ni(OH)<sub>2</sub> formed on the electrode surface. The NiO peak still presents in the spectrum showing that, only a very thin layer of the surface is used upon electrochemical process.

### 3.7. Capacitance of Nickel Oxide Thin Films and Effect of Calcination Temperature

Nickel oxide have promising super capacitive properties[102]. The shape of the CVs taken at scan rate of 50 mV/s are given in Figure 31 (a). The temperature dependent capacitance was calculated from the given CV curves. However, as the amount of NiO on the surface of FTO substrate is not optimized, catalytic load value is going to be ignored and absolute value of capacitance will be given in Farads just to show the temperature dependent capacitance change of.

The capacitance  $CS$  is calculated using the following formula:

$$CS = \frac{1}{2 * m * s * \Delta V} \int i \Delta V,$$

Where  $\Delta V$  is the voltage difference (V),  $s$  is the scan rate (V/s), and  $m$  is the mass of active material or catalytic load (g)[103].

The temperature dependent capacitance of nickel oxide electrodes is given in Table 7.

**Table 7.** Temperature dependent capacitance of m-NiO-10-XXX electrodes, where XXX calcination temperature.

Sample	Capacitance (F)
m-NiO-10-300	0.06042
m-NiO-10-350	0.03144
m-NiO-10-400	0.02537
m-NiO-10-450	0.01244
m-NiO-10-500	0.00624

As can be seen from the Table 7, the capacitance is decreasing with increasing calcination temperature. This can be explained by decreasing the specific surface area of mesoporous nickel oxide with increasing temperature (see previous chapters), as the electric double layer also decreases.

### 3.8. Characterization of Nickel Hydroxide

It can be concluded that even the product is NiO after calcination step, during the electrochemical process it is nickel hydroxide over the NiO pore-walls that does the job. In the literature, it is established that there are two forms of nickel hydroxide  $\alpha$ -Ni(OH)<sub>2</sub> and  $\beta$ -Ni(OH)<sub>2</sub>[104]. It was also discovered that upon base treatment of the

$\alpha$ -Ni(OH)<sub>2</sub> transforms to  $\beta$ -Ni(OH)<sub>2</sub>[104]. As all electrochemical experiments are conducted in a basic media it can be assumed that the layer of nickel hydroxide that is forming on the surface of nickel oxide during electrochemical process is or converted to a  $\beta$ -Ni(OH)<sub>2</sub> phase.

To support that, a powder XRD of the  $\alpha$ -Ni(OH)<sub>2</sub> and  $\beta$ -Ni(OH)<sub>2</sub> are shown in Figure 38.

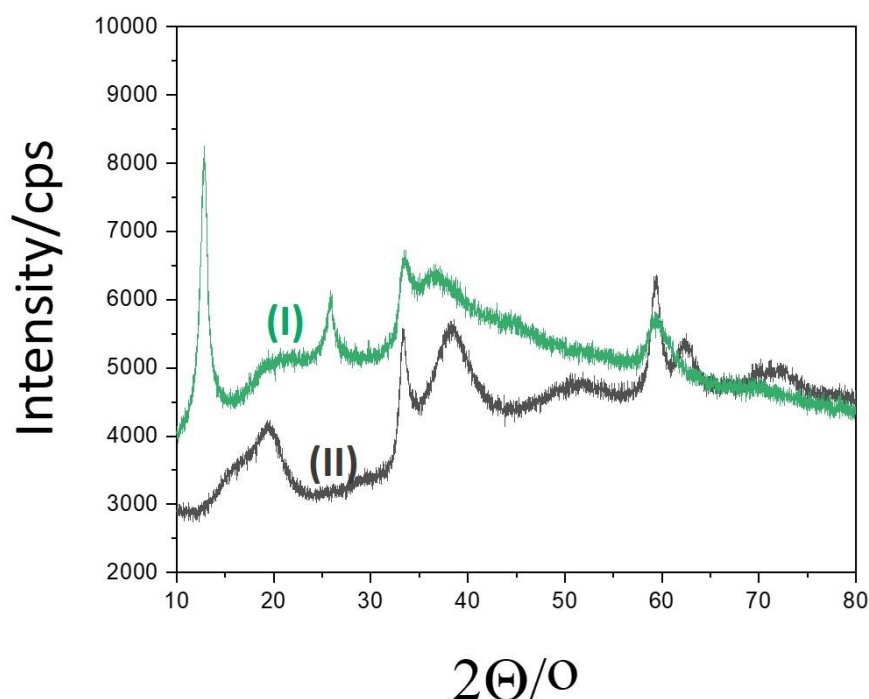


**Figure 38.** XRD patterns of (I)  $\alpha$ -Ni(OH)<sub>2</sub> just after calcination at 250 °C, and (II)  $\beta$ -Ni(OH)<sub>2</sub> after aging (I) in base for 10 minutes.

The  $\alpha$ -Ni(OH)<sub>2</sub> is formed right after calcination at 250 °C (PDF card 00-038-0715). Once the  $\alpha$ -Ni(OH)<sub>2</sub> is kept in an alkaline media for 10 minutes or more, the phase changes that was confirmed by XRD, see Figure 38. The diffraction lines are indexed to the  $\beta$ -Ni(OH)<sub>2</sub> (PDF card 00-059-0462).

Considering the fact that the metal oxide electrodes are used in a basic media, it can be assumed that all the electrochemical reactions happening on the surface of electrode are due to the activity of the  $\beta$ -Ni(OH)<sub>2</sub>.

### 3.9. Optical Properties of Nickel Oxide Thin Films

From the previous chapter, it has been established that during electrochemical process, upon oxidation, NiO turns into NiOOH or Ni<sup>3+</sup> species, and then reduces back to Ni(OH)<sub>2</sub> species. So, darkening of NiO thin film is explained by the presence of Ni<sup>3+</sup> species. When the Ni<sup>3+</sup> reduces to Ni<sup>2+</sup>, the film become transparent (clear). However, right after the calcination, the films are neither dark nor clear. Moreover, the color of the films can be controlled by electrochemical process, so the film can be completely dark upon oxidation and become completely clear at a reverse scan, see Figure 39.

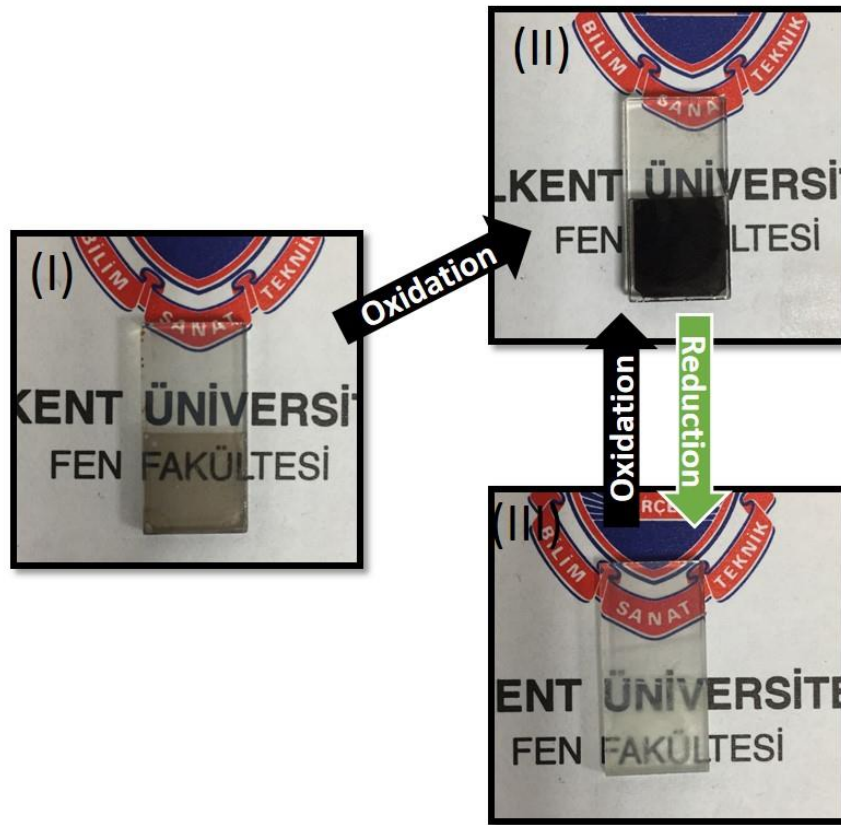


**Figure 39.** Photos of m-NiO thin films obtained at 300 °C(I) right after calcination, (II) after oxidation cycle, (III) after reduction cycle.

However, the color change is not only observed by an electrochemical process. The Ni<sup>3+</sup> species that make the nickel oxide film dark can also be reduced by a strong reducing agent, sodium borohydride (NaBH<sub>4</sub>) to Ni<sup>2+</sup> and make it clear. Also, it

supports the fact that the origin of black color is coming from the  $\text{Ni}^{3+}$  surface species.

Nickel oxide thin film prepared at  $300\text{ }^{\circ}\text{C}$  on a piece of quartz was dipped to a  $\text{NaBH}_4$  solution, washed with distilled water and monitored by using UV-vis spectroscopy. The obtained time dependent spectra are shown in Figure 40.

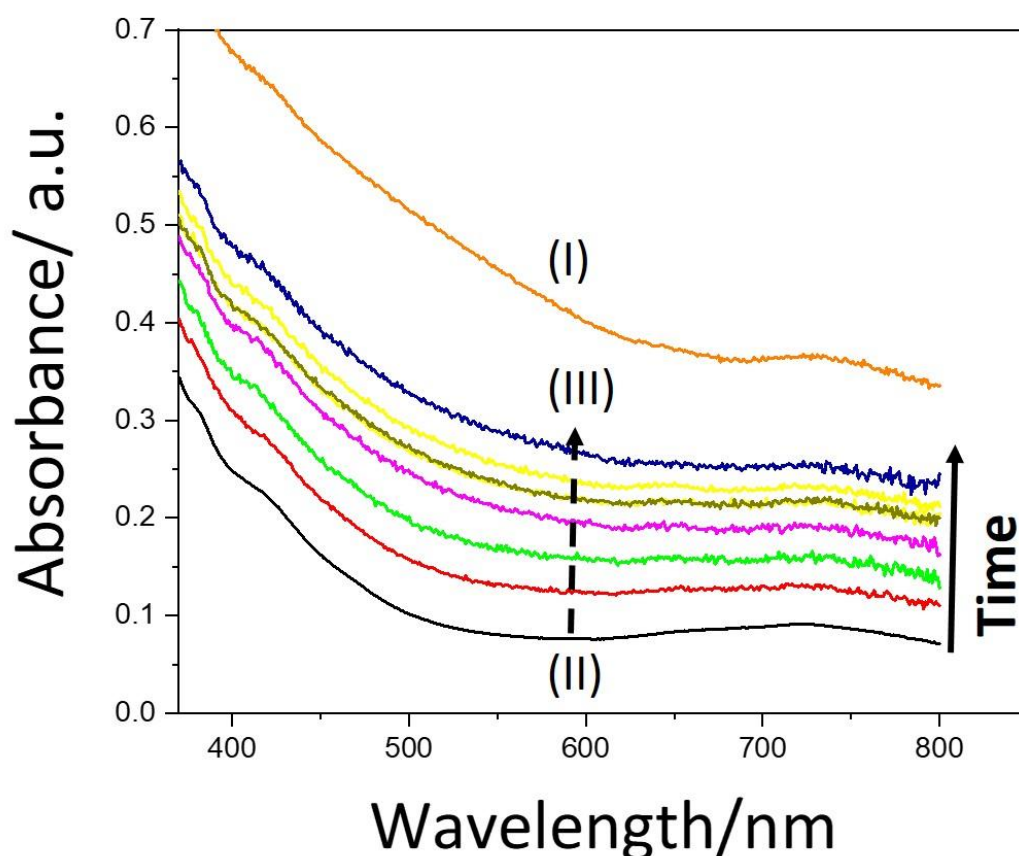


**Figure 40.** UV-Vis spectra of m-NiO calcined at  $300\text{ }^{\circ}\text{C}$ , (I) fresh sample, (II) the same sample treated with  $\text{NaBH}_4$  solution and (II) to (III) washed and aged under ambient condition for bottom to top 5, 10, 25, 45, 60, and 300 min.

From the spectra, the broad feature due to black species disappears right after dipping the sample into  $\text{NaBH}_4$  solution and washing. Once the sample is washed and dried, a lighter black color reappears, indicating that a self-oxidation is taking place on the surface and stops after sometime, see Figure 40.

### 3.10. Electrochromic Behavior of Mesoporous Nickel Oxide Thin Film.

Considering optical properties mentioned in the previous section, electrochromic behavior of mesoporous nickel oxide was further investigated, using a spectroelectrochemistry set up in Dr. Ülğüt's laboratory. Initially m-NiO electrodes at 300, 400 and 500 °C were prepared. Cyclic Voltammograms were collected at potential window of -400 to 600 mV at a scan rate of 20 mV/s. That setup was synchronized with the acquisition of UV-Vis spectra, and the spectra were collected during cycling experiment. Data is shown in Figure 41.

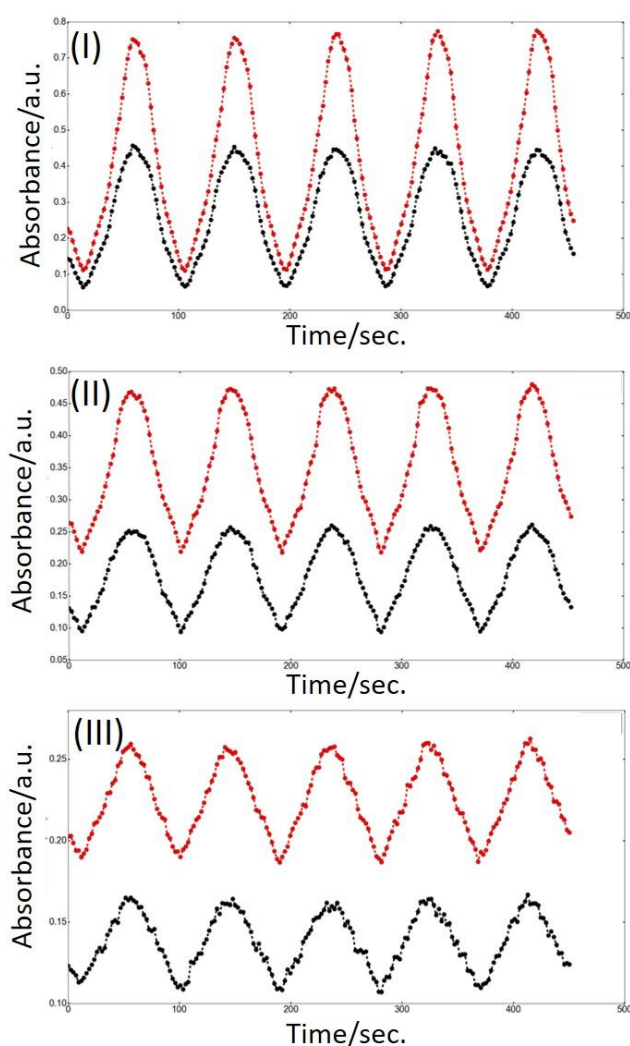


**Figure 41.** Electrochromic behavior of (I) m-10-NiO-300, (II) m-10-NiO-400, (III) m-10-NiO-500, absorbance versus time plot of voltage intervals of -400 to 600 mV at different wavelength of 585 nm (black), and 886 nm (red).

In the previous sections, a general electrochemical behavior was investigated, and applied voltage range was between -400 and 1200 mV. It was also established that if that voltage is applied, a chemical change occurs on the surface of electrode, and new species are forming. To collect spectra represented in the Figure 41 narrower potential window of -400 to 600 mV were used, to observe color change on the surface of NiO, without forming Ni(OH)<sub>2</sub> species. As shown in Figure 41, having the highest surface area, m-NiO-10-300 electrode showed the highest contrast between bleached and dark state. Absorbance values are 0.1 absorbance at a bleached state and 0.75 absorbance at a dark state in a wavelength of 886 nm and the process is reversible. Accordingly, m-NiO-10-500 having lowest surface area, showed the lowest contrast of 0.2 absorbance at a bleached state and 0.25 absorbance at dark state. Obviously, the surface area and concentration of Ni<sup>2+</sup> and Ni<sup>3+</sup> on the surface are the main factors in electrochromic behavior of NiO electrodes.

As the effect of calcination temperature on the electrochromism namely on color change contrast is established, the effect of potential that is applied needs to be investigated.

As m-NiO-10-300 electrode has the highest surface area and accordingly the highest contrast has been observed, this electrode was chosen for further analysis. So electrochromic switching experiment was conducted at several different potential windows. Data is shown in the Figure 42.

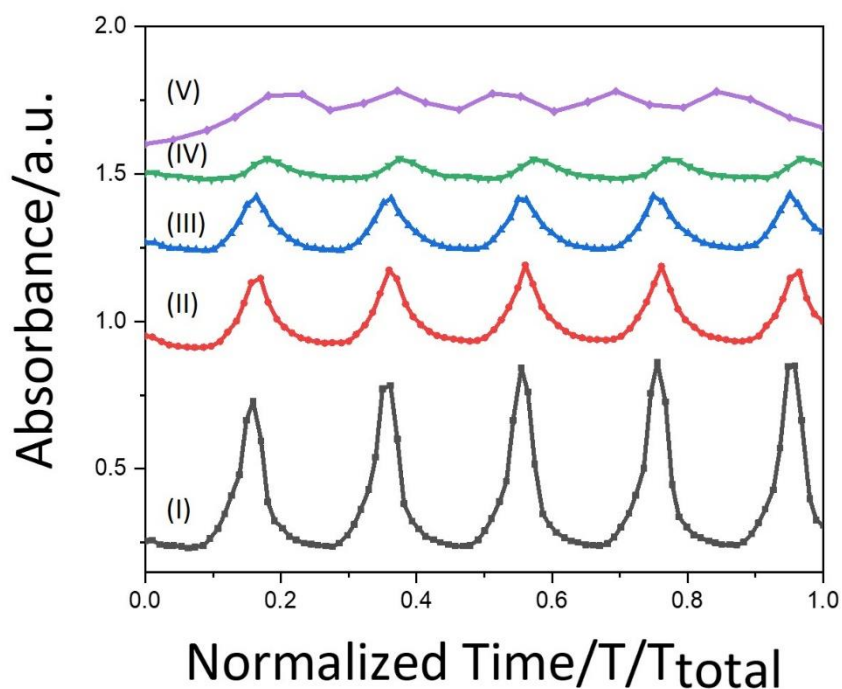


**Figure 42.** Electrochromic behavior of m-NiO-10-300, absorbance versus normalized time plot of voltage intervals of (I) -500 to 500 mV, (II) -500 to 400mV, (III) -500 to 345mV, (IV) -500 to 150 mV. And (V) 150 to 500 mV.

Clearly, each plot shows color change in any of the applied potential window, however the best contrast was shown between, -500 to 500 mV, and least contrast was observed between 150 to 500 mV, see Figure 42.

Considering the data from the previous sections, it can be summarized that the color switch is possible at all potential ranges and all  $\text{Ni}^{2+}$  species contribute to the electrochromic behavior, however the process is only reversible when potential that is applied is less than the potential required for water oxidation. As it leads to formation of other surface species, that make the process irreversible in terms of surface species. It was observed that surface of electrode with cycling changes, and can be reversed only after recalcination (see previous sections).

### 3.11. Freshly Prepared (Ni(II)+Co(II))/C<sub>12</sub>E<sub>10</sub> Film Characterization.

To show the flexibility and generality of the method developed in the previous section, two salts (Ni(II) and Co(II)) system was also investigated to synthesize spinel type mesoporous metal oxides, namely  $\text{NiCo}_2\text{O}_4$  in this section.

The first step of the synthesis process is preparation of the precursor solution, which was explicitly described in the experimental part. All solutions contain the same amount of CTAB and  $C_{12}E_{10}$  but varying amount of Ni(II) and Co(II) salts in ethanol and used as prepared in further steps of the process. The next step is to obtain a gel phase by two methods of coating: drop casting and spin coating. This is simply an evaporation of the volatile component (ethanol) from the solution. This process ensures formation of a lyotropic liquid crystalline (LLC) mesophase as thick (in case of drop casting) and thin (in the spin coating) gel films. The gel phase has been characterized by using small angle x-ray diffraction (XRD) and polarized optical microscope (POM) imaging techniques.

The fresh gel films, obtained by spin coating, were investigated in a wide range of both salts to surfactant ratio, starting from 6 to 25 mole ratio. Nickel to cobalt salt ratio was kept 1:2 making sure the calcination product is a spinel structure of  $NiCo_2O_4$ . The mesophases of the fresh films were decoded as  $\#(Ni(II)+Co(II))/C_{12}E_{10}$  where # is the sum of the mole of Ni(II) and Co(II) per  $C_{12}E_{10}$  (e. g.  $2Ni(II)+4Co(II)/C_{12}E_{10}$  for 6 mole ratio).

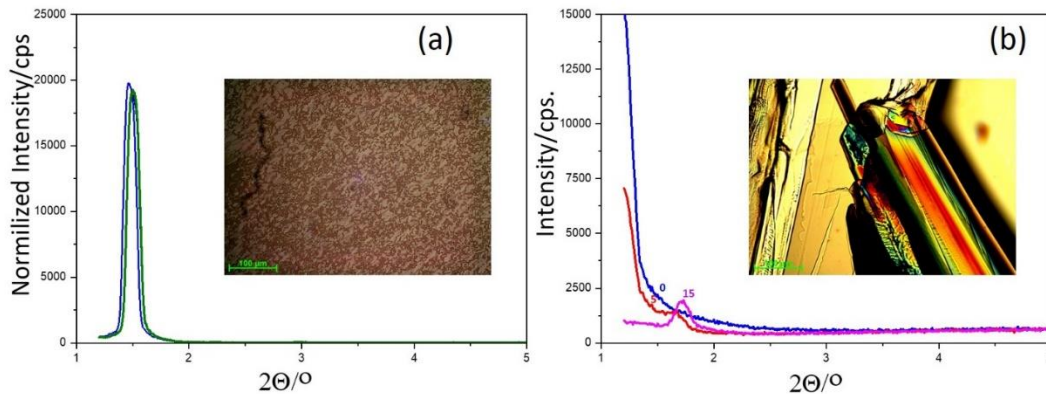


**Figure 43.** XRD patterns of (a)  $6(Ni(II)+Co(II))/C_{12}E_{10}$  mole ratio mesophase over time, immediately after coating, 10 and 30 minutes and (b)  $25(Ni(II)+Co(II))/C_{12}E_{10}$  mole ratio mesophase immediately after coating, 5 and 15 minutes. Insets are POM images of (a) fresh (b) 15 minutes aged samples.

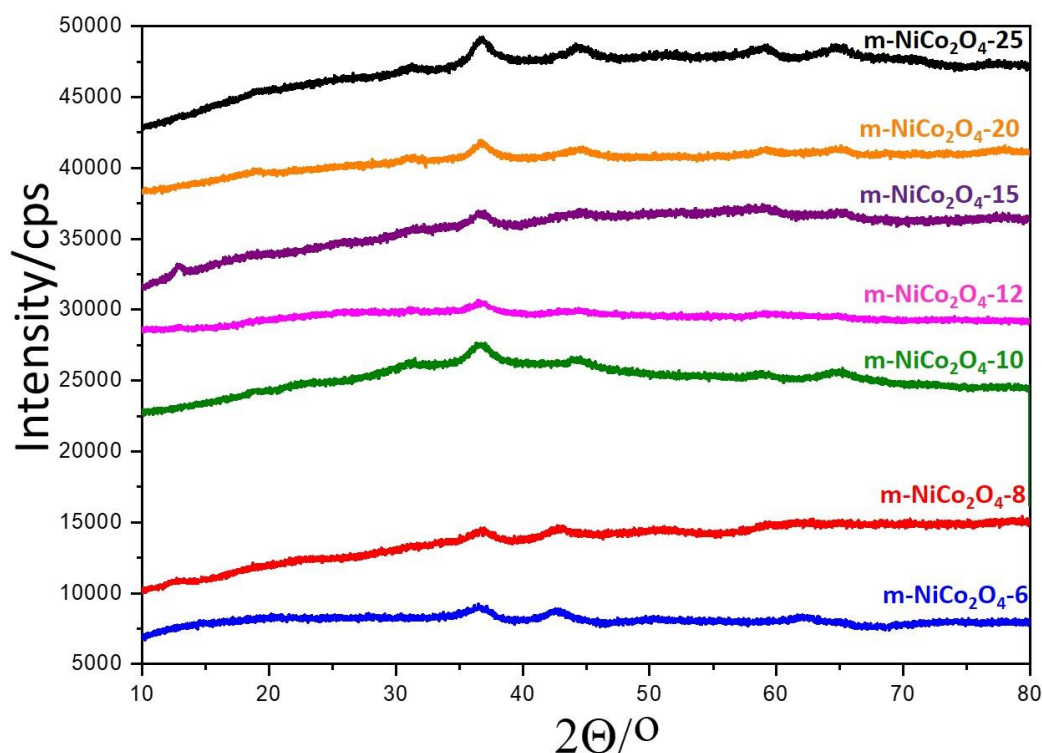
Figure 43 shows a set small angle XRD pattern of the samples, prepared using  $(Ni(II)+Co(II))/C_{12}E_{10}$  mole ratio of two extremes lowest salt to surfactant ratio of 6 and highest salt to surfactant ratio of 25 over time. In Figure 43(a), the diffraction

lines shift towards higher angles with aging the samples, indicating a shrinking of the mesophase due to further solvent evaporation (ethanol and extra water). It is difficult to identify the structure of the mesophase from a single XRD line, but the POM images clearly show that fresh samples have a 2D hexagonal phase. The POM image displays a fan-texture that is characteristic for the hexagonal mesophase. As salt to surfactant ratio is small, the mesophase is stable, and no salt crystals were observed under the POM after 30 minutes. However, if one looks at another extreme (see Figure 43(b)), the highest salt to surfactant ratio, no diffraction was observed immediately after coating, however after 5 minutes of aging the sample, a diffraction line appears, indicating that a cubic mesophase is formed. This assumption comes from the fact that the sample appears dark between the cross polarizers under POM. If the salt concentration is high, the mesophase is not stable over time. After 5 min of aging, it leaches out salt that is visible under the POM. So, the stability of these samples was confirmed by those observations under the optical microscope.

### 3.12. Optimization of Salt to Surfactant Ratio

To perform further characterization, optimization of the salt ratio is needed to determine the most suitable sample. Each sample, starting from 6 to 25 salt to surfactant ratio, was calcined at 250 °C for 1 hour and analyzed separately using XRD and N<sub>2</sub>-adsorption desorption techniques. The calcined films were labelled as *m*-NiCo<sub>2</sub>O<sub>4</sub> -#-XXX, where *m* stands for mesoporous, # is (Ni(II)+Co(II))/C<sub>12</sub>E<sub>10</sub> mole ratio in the precursor solutions, and XXX is the calcination temperature in Celsius.

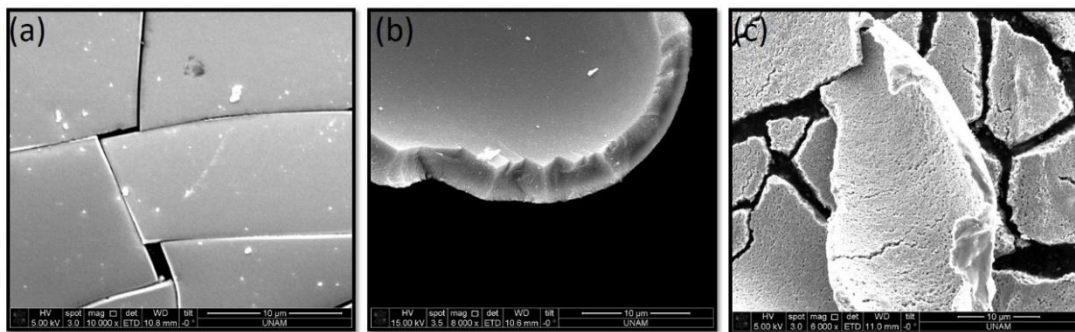
The calcined samples were first analyzed by using PXRD to determine the composition and crystal structure of the product. The XRD patterns of the samples are shown in Figure 44.



**Figure 44.** XRD patterns (bottom to top) of  $m\text{-NiCo}_2\text{O}_4\text{-}\#\text{-}250$ , where # is 6, 8, 10, 12, 15, 20, and 25.

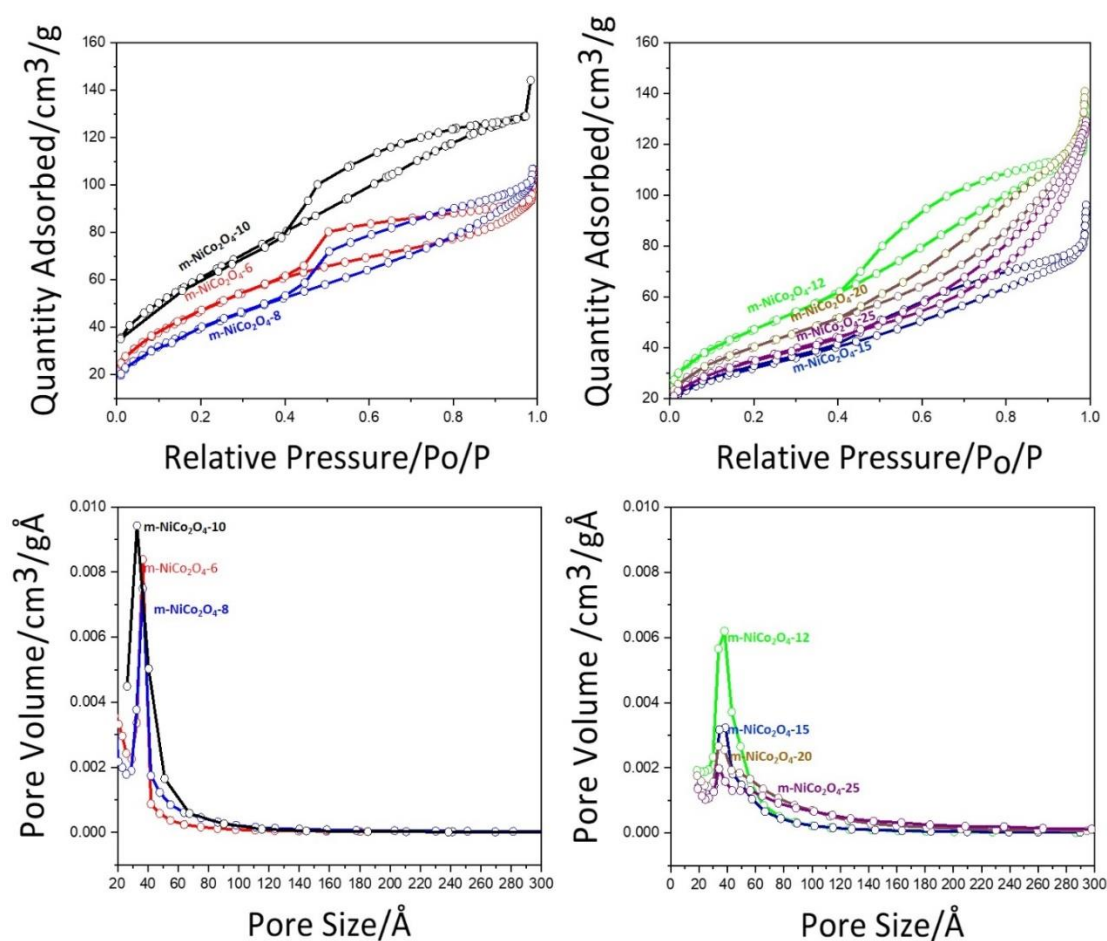
The XRD patterns show that some samples like  $m\text{-NiCo}_2\text{O}_4\text{-}6$  and  $m\text{-NiCo}_2\text{O}_4\text{-}8$  didn't burn effectively at 250 °C (see Figure 44). Even though majority of diffraction lines are indexed to a spinel structured  $\text{NiCo}_2\text{O}_4$  (PDF card – 00-020-0781), the diffraction lines at  $15^\circ$  belong to cobalt hydroxide or nickel hydroxide, which is understandable as temperature is not that high to react the precursor completely to form nickel cobalt oxide, and in that temperature nickel oxide cannot be formed.

Figure 45 shows the SEM images obtained from the mesoporous films upon calcination of the  $m\text{-NiCo}_2\text{O}_4\text{-}6$ ,  $m\text{-NiCo}_2\text{O}_4\text{-}15$ , and  $m\text{-NiCo}_2\text{O}_4\text{-}25$ . In terms of morphology, all compositions showed uniform film formation. As the salt concentration varies in these samples, the thickness of the samples is also different.



**Figure 45.** SEM images of (a) m-NiCo<sub>2</sub>O<sub>4</sub>-6, (b) m-NiCo<sub>2</sub>O<sub>4</sub>-15 (c) and m-NiCo<sub>2</sub>O<sub>4</sub>-25, scale bars are 10 μm.

The surface area of all samples calcined at 250 °C was measured using N<sub>2</sub> adsorption-desorption technique. The N<sub>2</sub>-adsorption desorption isotherms and pore size distribution plots are given in Figures 46.



**Figure 46.** N<sub>2</sub>(77 K) adsorption-desorption isotherms of (a) m-NiCo<sub>2</sub>O<sub>4</sub>-6-250, m-NiCo<sub>2</sub>O<sub>4</sub>-8-250, and m-NiCo<sub>2</sub>O<sub>4</sub>-10-250 and (b) m-NiCo<sub>2</sub>O<sub>4</sub>-12-250, m-NiCo<sub>2</sub>O<sub>4</sub>-15-250, m-NiCo<sub>2</sub>O<sub>4</sub>-20-250, and m-NiCo<sub>2</sub>O<sub>4</sub>-25-250, and pore size distribution plots (obtained from the desorption branches) of (c) m-NiCo<sub>2</sub>O<sub>4</sub>-6-250, m-NiCo<sub>2</sub>O<sub>4</sub>-8-250, and m-NiCo<sub>2</sub>O<sub>4</sub>-10-250 and (d) m-NiCo<sub>2</sub>O<sub>4</sub>-12-250, m-NiCo<sub>2</sub>O<sub>4</sub>-15-250, m-NiCo<sub>2</sub>O<sub>4</sub>-20-250, and m-NiCo<sub>2</sub>O<sub>4</sub>-25-250.

Figure 46 shows the N<sub>2</sub> adsorption-desorption isotherms and pore-size distribution plots of m-NiCo<sub>2</sub>O<sub>4</sub>-6-250, m-NiCo<sub>2</sub>O<sub>4</sub>-8-250, m-NiCo<sub>2</sub>O<sub>4</sub>-10-250, m-NiCo<sub>2</sub>O<sub>4</sub>-12-250, m-NiCo<sub>2</sub>O<sub>4</sub>-15-250, m-NiCo<sub>2</sub>O<sub>4</sub>-20-250, and m-NiCo<sub>2</sub>O<sub>4</sub>-25-250. The isotherms are type IV and characteristic for mesoporous materials.

Among all analyzed samples, the m-NiCo<sub>2</sub>O<sub>4</sub>-25-250 showed least uniform pore size distribution. Also, m-NiCo<sub>2</sub>O<sub>4</sub>-25-250 has the lowest surface area of 128 m<sup>2</sup>/g among all analyzed samples, and pore size of 6 nm. It can be explained by high salt concentration, as pores can be collapsed and quite disordered because of significant

salt content. Most uniform pore size distribution was observed in m-NiCo<sub>2</sub>O<sub>4</sub>-10-250, as in the case of nickel oxide, this sample has a surface area of 223 m<sup>2</sup>/g, pore size of 3.9 nm, and pore volume of 0.191 cm<sup>3</sup>/g. Therefore, it is the optimum salt content for further characterization. All the surface area, pore size, and pore volume data are listed in Table 8.

Compare to nickel oxide, mixed nickel cobalt oxide formed at quite low temperature however it didn't show clear trend and surface areas and pore sizes. The reason for that may be the calcination temperature, as it is quite low at some sample's pores might be still blocked by surfactant or hydroxide species.

**Table 8.** N<sub>2</sub> (77K) adsorption-desorption data of m-NiCo<sub>2</sub>O<sub>4</sub>-XXX samples (# is Ni+Co/C<sub>12</sub>E<sub>10</sub> mole ratio and XXX is calcination/annealing temperature in Celsius).

Sample	BET Surface Area (m <sup>2</sup> /g)	BJH Pore Volume (cm <sup>3</sup> /g)	BJH Pore Size (nm)
m-NiCo <sub>2</sub> O <sub>4</sub> -6-250	175	0.145	3.5
m-NiCo <sub>2</sub> O <sub>4</sub> -8-250	148	0.161	3.9
m-NiCo <sub>2</sub> O <sub>4</sub> -10-250	223	0.191	3.9
m-NiCo <sub>2</sub> O <sub>4</sub> -12-250	172	0.198	4.5
m-NiCo <sub>2</sub> O <sub>4</sub> -15-250	115	0.139	4.5
m-NiCo <sub>2</sub> O <sub>4</sub> -20-250	142	0.205	5.6
m-NiCo <sub>2</sub> O <sub>4</sub> -25-250	128	0.187	6.0

### 3.13. Optimization of Calcination Temperature

As the salt concentration is optimized, the effect of calcination temperature on the composition, surface area, and particle size of mesoporous nickel cobalt oxide must be investigated. The temperature dependent PXRD data is shown in Figure 47.

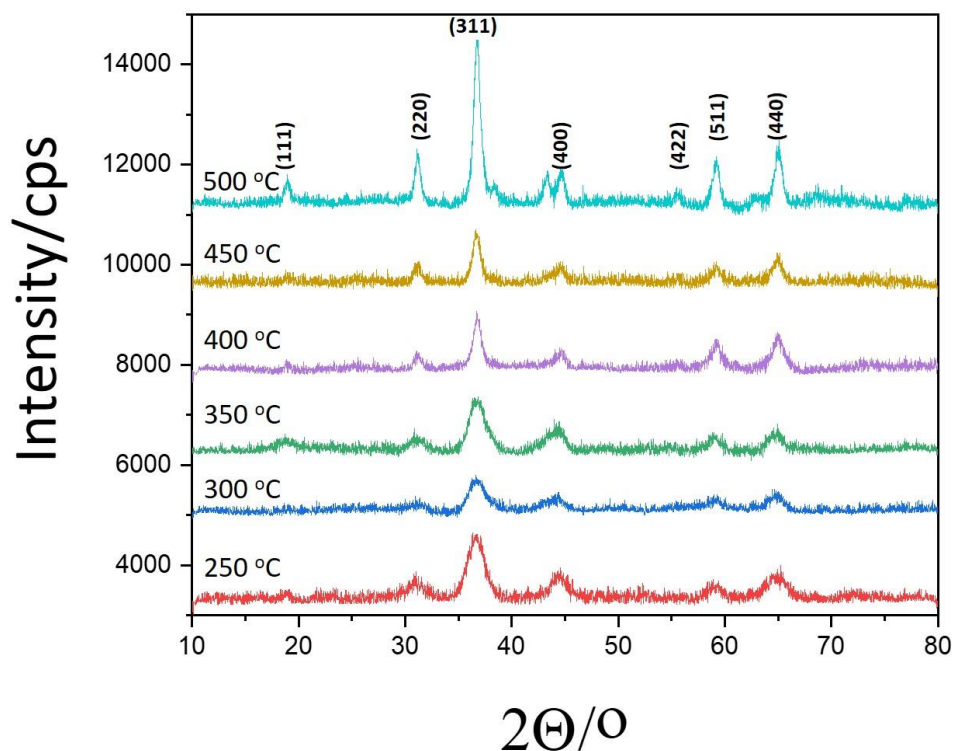


**Figure 47.** XRD patterns (subtracted background) of the m-NiCo<sub>2</sub>O<sub>4</sub>-10-250, m-NiCo<sub>2</sub>O<sub>4</sub>-10-300, m-NiCo<sub>2</sub>O<sub>4</sub>-10-350, m-NiCo<sub>2</sub>O<sub>4</sub>-10-400, m-NiCo<sub>2</sub>O<sub>4</sub>-10-450, and m-NiCo<sub>2</sub>O<sub>4</sub>-10-500 (bottom to top).

As shown in the figure above, the calcination product is NiCo<sub>2</sub>O<sub>4</sub> spinel structure. All lines can be indexed accordingly. (PDF card – 00-020-0781). With increasing calcination temperature, diffraction lines get sharper, indicating growth or crystallization of the nanocrystalline pore-walls.

To investigate the changes in the surface area and pore size, N<sub>2</sub>-adsorption desorption data was also collected. The adsorption desorption isotherms and pore size distribution plots for m-NiCo<sub>2</sub>O<sub>4</sub>-10 are shown in Figure 48. The surface area and pore size information are presented in Table 9.

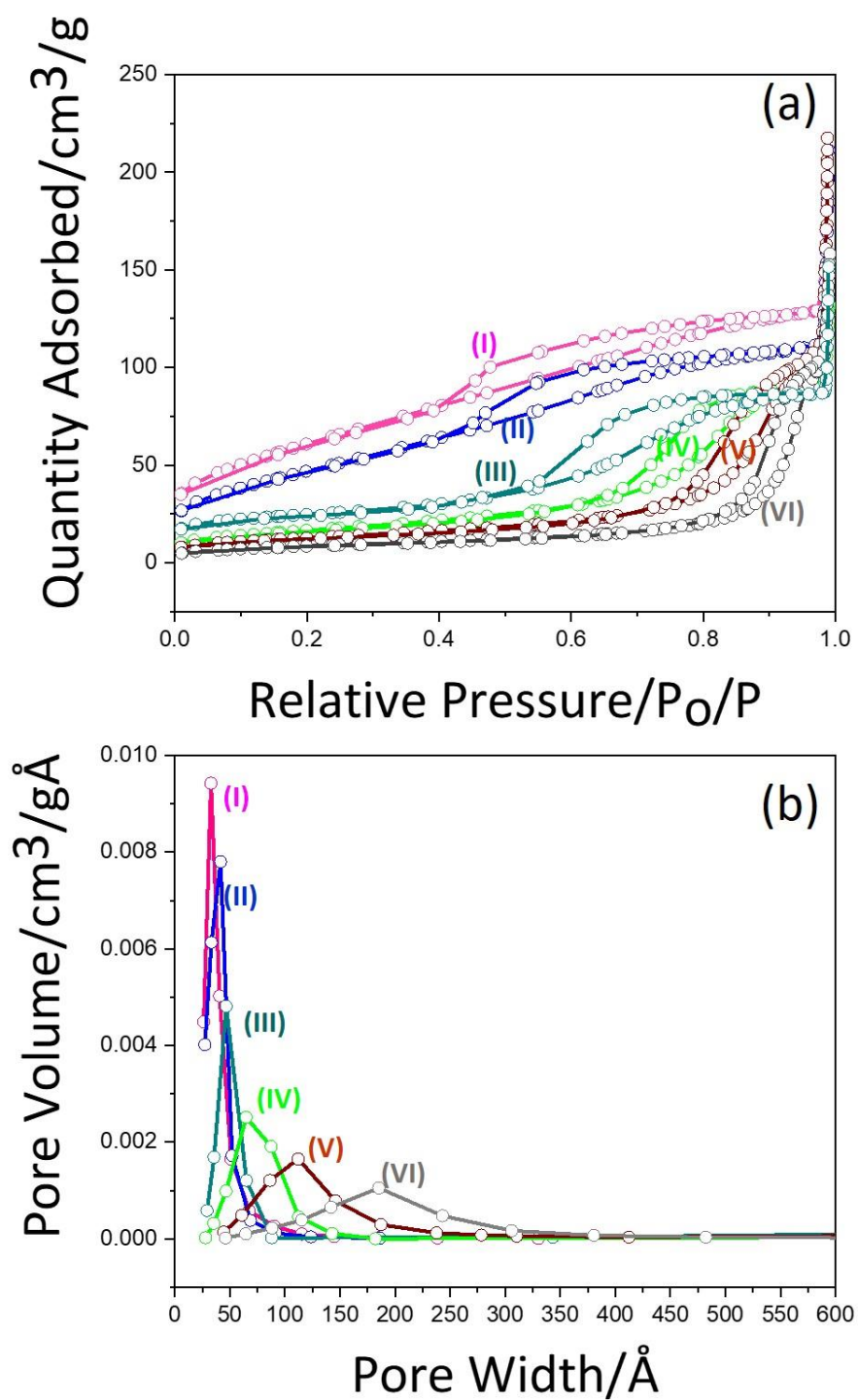
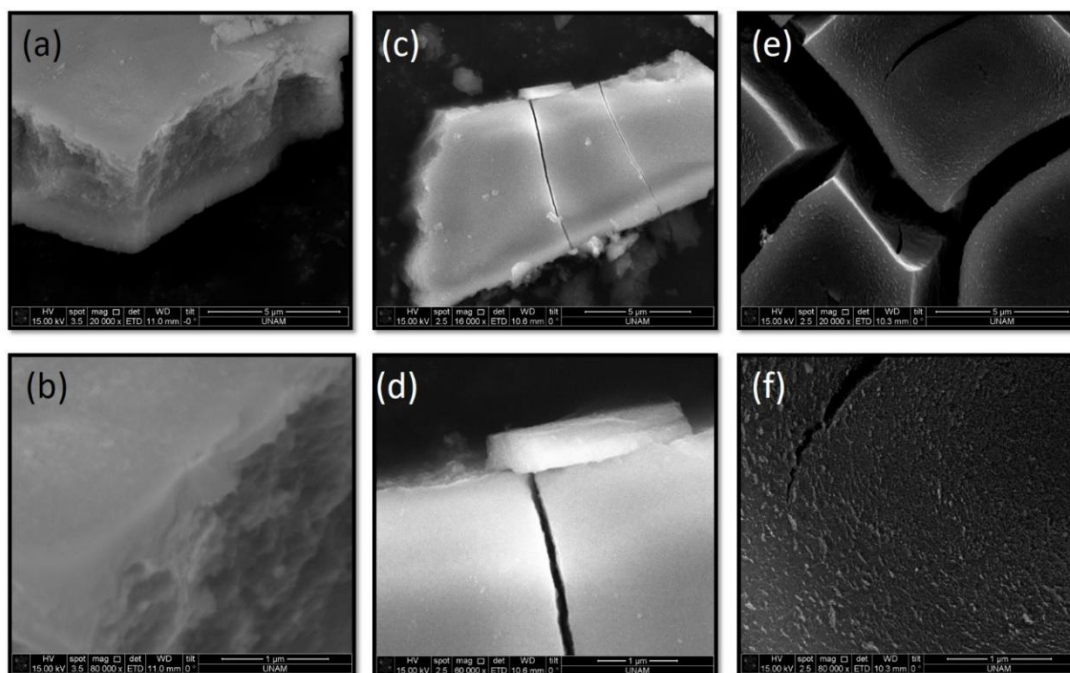


**Figure 48.** (a)  $\text{N}_2(77\text{ K})$  adsorption-desorption isotherms and (b) pore size distribution of (I)  $m\text{-NiCo}_2\text{O}_4\text{-10-250}$ , (II)  $m\text{-NiCo}_2\text{O}_4\text{-10-300}$ , (III)  $m\text{-NiCo}_2\text{O}_4\text{-10-350}$ , (IV)  $m\text{-NiCo}_2\text{O}_4\text{-10-400}$ , (V)  $m\text{-NiCo}_2\text{O}_4\text{-10-450}$ , and (VI)  $m\text{-NiCo}_2\text{O}_4\text{-10-500}$ .

**Table 9.** N<sub>2</sub> (77K) adsorption-desorption data of m-NiCo<sub>2</sub>O<sub>4</sub>-10-XXX samples (XXX is calcination/annealing temperature in Celsius).

Sample	BET Surface Area (m <sup>2</sup> /g)	BJH Pore Volume (cm <sup>3</sup> /g)	BJH Pore Size (nm)
m-NiCo <sub>2</sub> O <sub>4</sub> -10-250	223	0.191	3.9
m-NiCo <sub>2</sub> O <sub>4</sub> -10-300	172	0.322	6.9
m-NiCo <sub>2</sub> O <sub>4</sub> -10-350	86	0.211	7.4
m-NiCo <sub>2</sub> O <sub>4</sub> -10-400	60	0.197	10
m-NiCo <sub>2</sub> O <sub>4</sub> -10-450	46	0.327	21.5
m-NiCo <sub>2</sub> O <sub>4</sub> -10-500	31	0.236	25.6

The N<sub>2</sub> adsorption-desorption isotherms are type-IV at all temperatures and characteristic for the mesoporous materials. It is clear from the pore size distribution plots that as the pore size expands due to temperature increase, the pores become less uniform. The surface area drops from 223 m<sup>2</sup>/g at 250 °C to 31 m<sup>2</sup>/g at 500 °C. The pore size also changes accordingly from 3.9 nm at lowest calcination temperature to 25.6 nm at highest calcination temperature. Figure 49 shows a series as SEM images of the m-NiCo<sub>2</sub>O<sub>4</sub> calcined at different temperatures and display a uniform film morphology. The samples calcined over 450 °C also show uniform pores in the films at high magnifications.



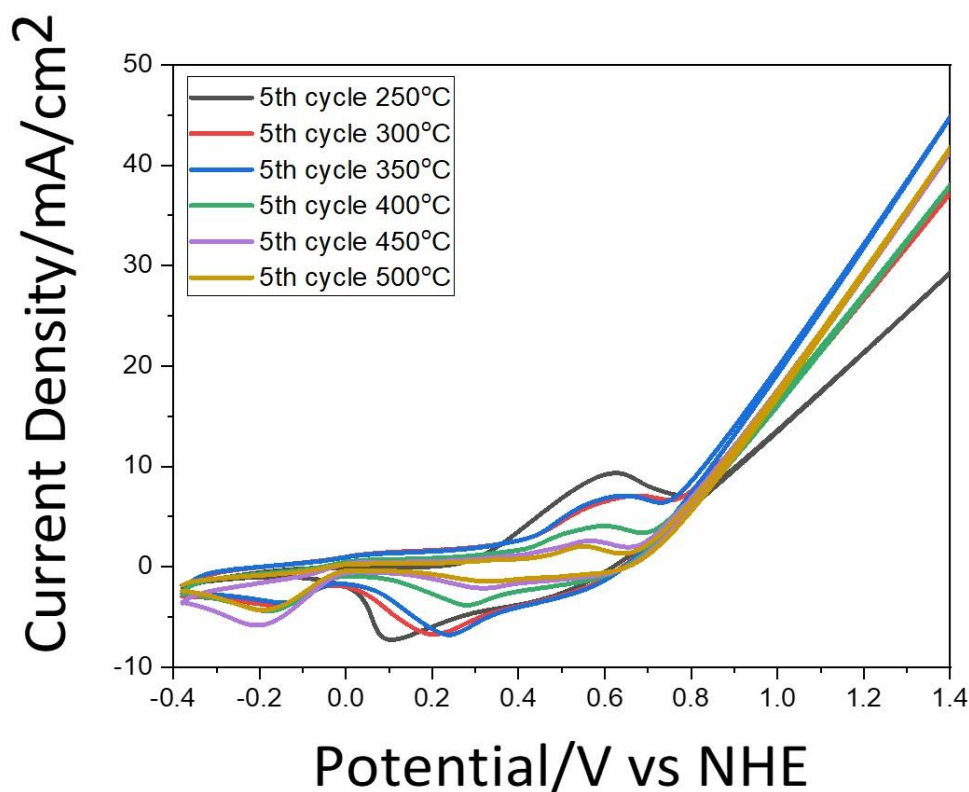
**Figure 49.** SEM images of (a) m-NiCo<sub>2</sub>O<sub>4</sub>-10-250 at 5 μm, (b) m-NiCo<sub>2</sub>O<sub>4</sub>-10-250 at 1 μm; (c) m-NiCo<sub>2</sub>O<sub>4</sub>-10-350 at 5 μm, (d) m-NiCo<sub>2</sub>O<sub>4</sub>-10-350 at 1 μm; (e) m-NiCo<sub>2</sub>O<sub>4</sub>-10-450 at 5 μm, (f) m-NiCo<sub>2</sub>O<sub>4</sub>-10-450 at 1 μm.

Figure 49 shows the SEM images of m-NiCo<sub>2</sub>O<sub>4</sub>-10-250, m-NiCo<sub>2</sub>O<sub>4</sub>-10-350, and m-NiCo<sub>2</sub>O<sub>4</sub>-10-450 at different magnifications. Uniform film morphology is preserved at low (250 °C) as well as at high calcination temperatures (450 °C). At a scale bar of 1 μm some porosity can be observed at 450 °C. It supports the BET data as pore size at this temperature is 21 nm, which makes it possible to image it by SEM.

### 3.14. Electrochemical Characterization of NiCo<sub>2</sub>O<sub>4</sub> Thin Films

To better understand properties of the mesoporous nickel cobaltite, electrochemical characterization was conducted using m-NiCo<sub>2</sub>O<sub>4</sub>-10 thin films coated over FTO coated glass using cyclic voltammetry (CV) technique in an alkali media (1M KOH aqueous solution). Initially, 5 CVs was taken at a sweep rate of 50 mV/s, in a potential window from -400 mV to 1400 mV.

The CVs of 5<sup>th</sup> cycle of each electrode calcined at 250, 300, 350, 400, 450, and 500 °C are shown in the Figure 50.



**Figure 50.** 5<sup>th</sup> CV of m-NiCo<sub>2</sub>O<sub>4</sub>-10 electrodes calcined at 250, 300, 350, 400, 450, and 500 °C.

Like nickel oxide electrodes, nickel cobalt oxides show electrochemical behavior according to surface area and crystallinity, as the current density of Ni<sup>+2</sup>/Ni<sup>3+</sup> is decreasing with increasing calcination temperature. It was also established that the oxidation peak around 500 mV belongs to Ni(II) species. The electrode prepared at 250 °C (surface area 223 m<sup>2</sup>/g) showed peak current density of around 10 mA/cm<sup>2</sup>, while the electrode calcined at 500 °C (surface area 32 m<sup>2</sup>/g) showed peak current density around 2 mA/cm<sup>2</sup>. However, if one looks at water oxidation side, more crystalline samples (350 °C, and 500 °C) show high current densities.

To better understand water oxidation process, a Tafel slope was obtained from chronoamperometry measurement that was performed after 5 CVs to each electrode by applying an input voltage and recording the output current. Data was displayed as over potential versus logarithm of the current density. The slopes are provided in the Figure 51.

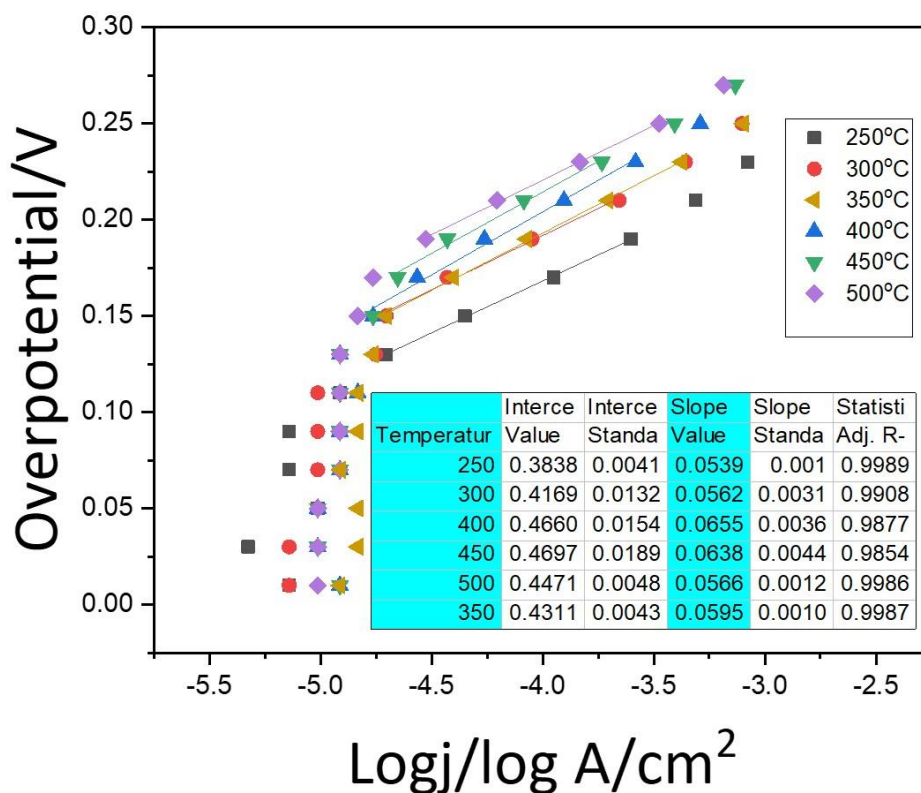


**Figure 51.** Tafel slope of m-NiCo<sub>2</sub>O<sub>4</sub>-10 electrodes, calcined at 250, 300, 350, 400, 450, and 500 °C.

The lowest slope indicates that this sample is the most efficient for water oxidation, in other words, one needs less potential to oxidize water. In Figure 51, it is clear that the electrodes prepared at 250 and 350 °C have the lowest Tafel slopes of 53.9 and 59.5 mV/dec, respectively. So, these electrodes were picked for further analysis.

These two electrodes were cycled 100 more times, to check the stability of these electrodes and effect on water oxidation. Then, the Tafel analysis was performed again, in the same way as after 5 cycles. The 5<sup>th</sup> and 100<sup>th</sup> CVs of electrodes prepared at 250 and 350 °C, and Tafel slope are provided in the Figure 52.

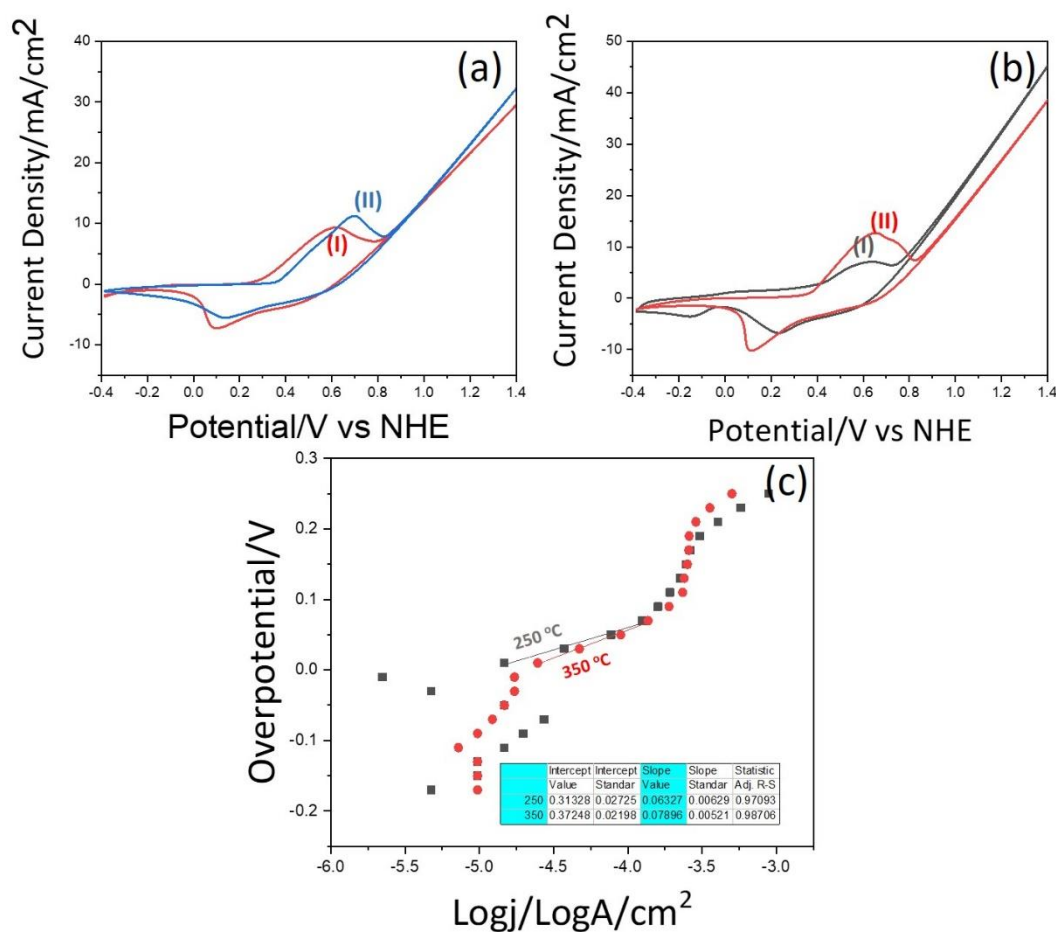


**Figure 52.** (a) (I) 5<sup>th</sup> and (II) 100<sup>th</sup> CVs of m-NiCo<sub>2</sub>O<sub>4</sub>-10-250; (b) (I) 5<sup>th</sup> and (II) 100<sup>th</sup> CVs of m-NiCo<sub>2</sub>O<sub>4</sub>-10-350 electrodes. (c) Tafel slopes of m-NiCo<sub>2</sub>O<sub>4</sub>-10 electrodes calcined at 250 and 350 °C after 100 cycles.

As shown in Figure 52(a) and 52(b), the peak current densities of both 250 and 300 °C electrodes are increased, which tells that electrodes are stable upon cycling. After chronoamperometry experiment, the Tafel slope was obtained and it was noticed that the slope of m-NiCo<sub>2</sub>O<sub>4</sub>-10-250 was 63 mV/dec while, the slope of m-NiCo<sub>2</sub>O<sub>4</sub>-10-350 was constituted 79 mV/dec. Generally, water oxidation performance of both samples decreased after 100 CVs, however, 250 °C, having high surface area is the best for water oxidation among all analyzed samples. The purpose of this section was to show how the LLC systems can be expanded to produce mixed oxides, the characterization of these electrodes can be further carried to show their superior properties, such as electrocatalysis and supercapacitor applications. As shown in the CV curves, the area in the full CV cycle (from -0.4 to 0.8 V, a large potential

window and quite high current density) is quite large, indicating the pseudosupercapacity of the  $m\text{-NiCo}_2\text{O}_4$  electrodes. Note also that the typical weight of these electrodes is around 0.1 mg. Therefore, the specific capacities must be quite high and needs to be investigated further.

# CHAPTER 4

## 4.CONCLUSION

In this thesis work, the molten-salt assisted self-assembly (MASA) approach was adopted to synthesize mesoporous nickel oxide and nickel cobaltite thin films. The main difference of MASA method from EISA method mentioned in the introduction is the presence of charged surfactant CTAB and two solvents: primary and secondary. Presence of an ionic surfactant allows accommodating more salt species into a mesophase that significantly increases uniformity and porosity of the obtained material after calcination. The salt species, nickel nitrate hexahydrate and cobalt nitrate hexahydrate act as secondary solvent and metal ion precursor. The primary solvent, ethanol, ensures a homogeneous precursor solution before spreading the solution over a substrate. For large amount of samples, required for  $N_2$  adsorption-desorption isotherms and XRD patterns, the coating method should be drop casting that produces thicker films. However, for electrode preparation, spin coated method is a better method to fabricate thin films. Freshly coated thin films diffract at small angles, indicating the formation of a mesophase. Simply, the films coated from clear solutions are in LLC mesophase that are stable up to 10 salt/surfactant mole ratio but leach out salt crystals at higher salt concentrations. Those compositions need to be calcined immediately after the formation of the mesophase to produce mesoporous metal oxides.

Mesoporous nickel oxide and nickel cobaltite obtained after calcination have a high specific surface areas and uniform pore size distributions. The pore size and surfaces area can be easily controlled by changing precursor salt to surfactant ratio and calcination temperature. NiO and  $NiCo_2O_4$  possesses a high specific surface area at low calcination temperatures (such as 300 °C) and it significantly drops with increasing annealing temperature High quality films can be obtained by using intermediate compositions (6-12 mole ratio), but relatively lower quality films (very fragile) can also be obtained by using higher salt to surfactant ratios. While the crystalline NiO and  $NiCo_2O_4$  pore-walls grow, the pores expand by annealing the

films at elevated temperatures. The method MASA, introduced in this work, allows one to control surface area, pore size, crystalline pore wall size and the thickness of the films that may be desired for various applications.

Due to unique optical properties of mesoporous nickel oxide thin films, the prepared electrodes showed electrochromic behavior, which could be controlled by playing with, applied potential window, annealing temperature and thickness of the film. In this process top few layer of NiO is converted into Ni(OH)<sub>2</sub> creating a surface skin/shell over the nanocrystalline NiO pore-walls. Further oxidation/reduction cycles in the CVs or switching the color of the electrode in the electrochromic process take place between Ni(OH)<sub>2</sub> and NiOOH species. During the use of the electrode, it is likely that the surface morphology is changing by further conversion of NiO core into Ni(OH)<sub>2</sub> shell; Ni(OH)<sub>2</sub> shell slowly grows over the use and creates more active surface species. So, the electrochromic switching occurs between Ni<sup>3+</sup> (dark) and Ni<sup>2+</sup> (clear) species, where the surface area is more critical unless fast switching is required.

Mesoporous NiCo<sub>2</sub>O<sub>4</sub> has similar surface area and pore size distribution at low calcination temperatures. The m-NiCo<sub>2</sub>O<sub>4</sub> thin films electrodes characterized using cyclic voltammetry. The electrochemical behavior and the shape of the CVs were changed upon the calcination temperature, which allows to control the electrochemical performance of m-NiCo<sub>2</sub>O<sub>4</sub> thin films. Analyzing of Tafel slopes showed that these electrodes showed low overpotentials, which tells that mesoporous nickel cobaltite is promising water oxidation catalyst.

To conclude, in this thesis work shows that the MASA method could be used to produce both mesoporous metal oxides (NiO) and mixed metal oxide (NiCo<sub>2</sub>O<sub>4</sub>) thin films with high specific surface area and excellent performance on electrochromic and catalytic performance, respectively.

# CHAPTER 5

## 5.FUTURE WORK

### 5.1 Synthesis and Characterization of Mesoporous Nickel Oxide on Silica Template

To better understand the properties of mesoporous nickel oxide, another synthesis route was employed to produce m-NiO. In the new method tetramethyl orthosilicate (TMOS) was added to the clear precursor solution of Ni(II)/C<sub>12</sub>E<sub>10</sub> mesophase.

The composition of precursor solution is given in Table 10.

**Table 10.** Composition of the clear solutions used for the preparations of mesoporous NiO/SiO<sub>2</sub> films.

Amount of TMOS (g)	Amount of [Ni(OH <sub>2</sub> ) <sub>6</sub> ](NO <sub>3</sub> ) <sub>2</sub> (g)	Amount of CTAB (g)	Amount of P123 (g)	Amount of HNO <sub>3</sub> (drops)	Amount of Water (ml)
0.262 g 20 mole ratio	1.504 g 60 mole ratio	0.157 g 5 mole ratio	0.5 g 1 mole ratio	3	10

Compared to composition of precursor solution that was used in previous chapters, non-ionic surfactant 10 lauryl ether was replaced with P123, instead of ethanol, water was used and to enhance the polymerization of silica 3 drops of nitric acid were added. The salt to P123 ratio was kept as 60 to 1; it is a comparable composition to 10 Ni(II)/C<sub>12</sub>E<sub>10</sub> ratio in the 10 lauryl ether.

The clear precursor solution was coated on the glass substrate using drop casting and kept in laboratory conditions for 10 minutes to ensure solvent evaporation and mesophase formation. Then fresh samples were calcined for three hours at 450 °C. Samples were scratched and analyzed using powder XRD technique. The XRD pattern is shown in Figure 53.

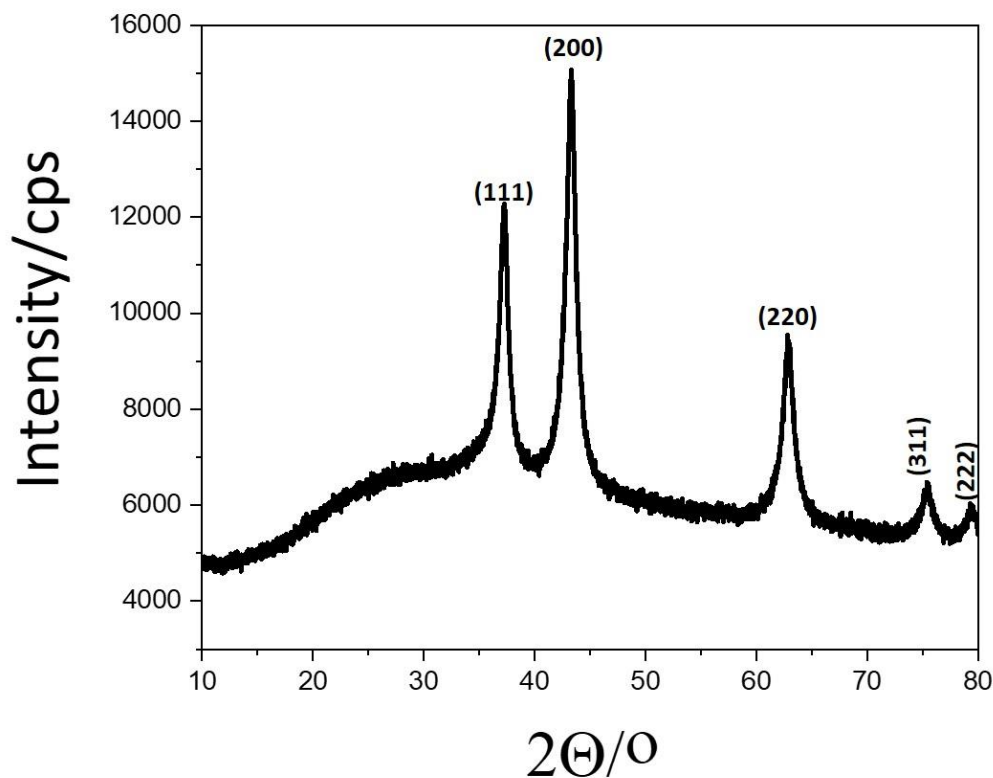


**Figure 53.** XRD pattern of m-NiO on silica template at 450 °C.

The pattern is indexed using ICDD data base to PDF card number - 00-044-1159. Accordingly, the lines at 37, 43, 63, 75. And 79°, 2θ, have been indexed to (111), (200), (220), (311), and (222) planes, respectively, of face centered cubic rock-salt structure of NiO. No silica lines were visible in the pattern, indicating that silica layer is amorphous and the NiO is coating the silica surface. The diffraction lines are quite broad, indicating that the NiO particles are small. The particles size calculated from Scherrer equation along 200 plane is around 9 nm[101].

The same sample was analyzed further using N<sub>2</sub>-adsorption-desorption technique. Specific surface area comprised 104 m<sup>2</sup>/g. To compare, the surface area of m-NiO without silica constituted 28 m<sup>2</sup>/g, almost four times less. So adding silica to the Ni(II)/surfactant system significantly improved the surface area. To support the XRD

data, the  $N_2$  adsorption-desorption isotherms and pore size distribution plots are shown in Figure 54.

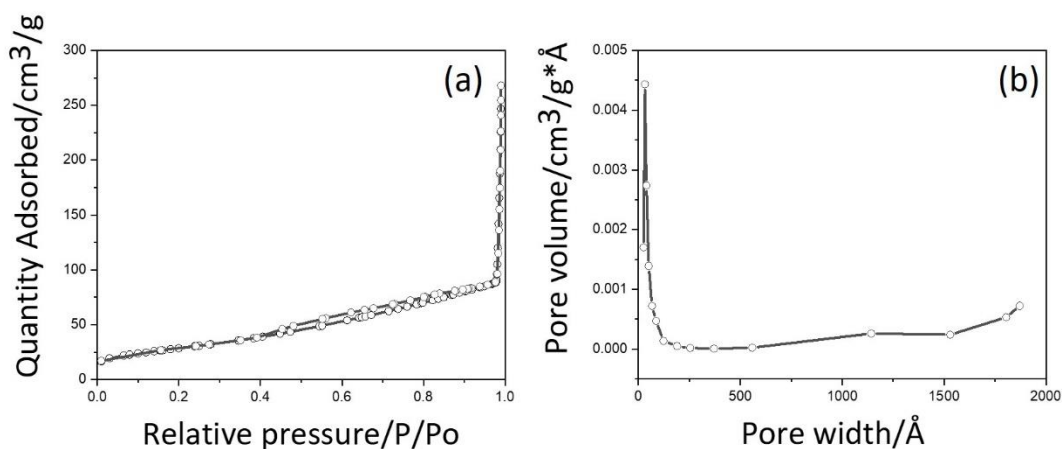


**Figure 54.** (a)  $N_2$ (77 K) adsorption-desorption isotherms and (b) pore size distribution of m-NiO on silica at 450 °C.

The isotherm shown in the Figure 54 (a) is type IV and characteristic for mesoporous materials, confirming that formed NiO/SiO<sub>2</sub> is mesoporous. Pore size distribution plot (see Figure 54 (b)) shows a dominant pore diameter of 3.2 nm and broad size distribution of 90-110 nm. It constitutes double pore system (small for large surface area and large for accessibility) and could be beneficial in electrochemical applications. To confirm the presence of macropores (large pores), SEM images are shown in Figure 55.

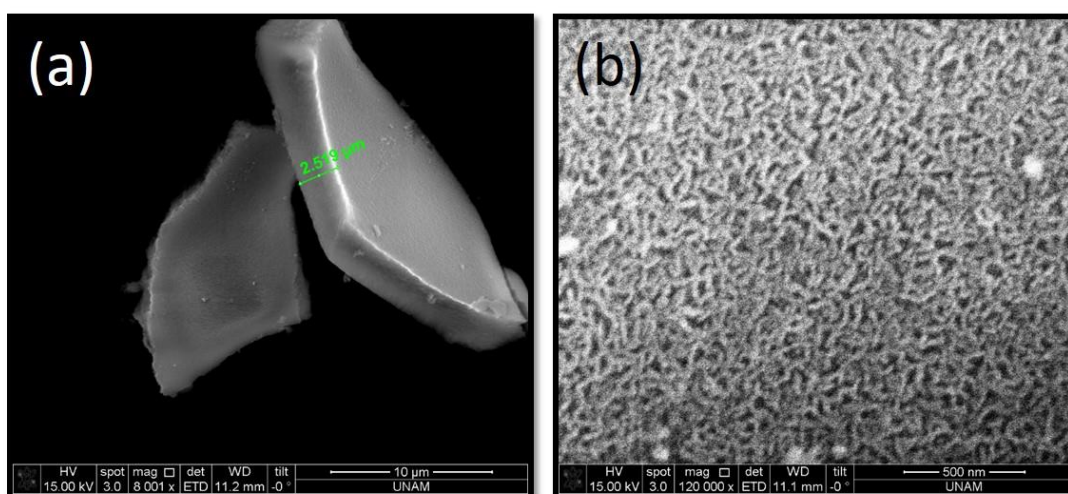


**Figure 55.** SEM images of (a) m-NiO-350 (scale bar is 10  $\mu m$ ) and (b) m-NiO/SiO<sub>2</sub>-350 (scale bar is 500 nm).

From the Figure 55, it is clearly shown that, m-NiO/SiO<sub>2</sub> formed a very uniform film, even though coating method was drop casting. At higher magnifications, large macro pores are clearly shown in the SEM image (Figure 55(b)).

As silica-templated nickel oxide has a larger surface area than nickel oxide without silica, the electrochemical properties and electrochromic measurements are needed to be performed on the silica-templated nickel oxide electrodes.

# BIBLIOGRAPHY

- [1] M. E. Davis, "Ordered porous materials for emerging applications," *Nature*. pp. 813–821, 2002.
- [2] IUPAC, "Manuals of symbols and terminology for physicochemical quantities and units. Appendix II. Definitions, terminology, and symbols in colloid and surface chemistry.," *Pure Appl. Chem.*, vol. 31, no. 577, pp. 74–86, 1972.
- [3] C. T. Kresge, M. E. Leonowicz, W. J. Roth, J. C. Vartuli, and J. S. Beck, "Ordered mesoporous molecular sieves synthesized by a liquid-crystal template mechanism," *Nature*, vol. 359, pp. 710–712, 1992.
- [4] P. Selvam, S. K. Bhatia, and C. G. Sonwane, "Recent advances in processing and characterization of periodic mesoporous MCM-41 silicate molecular sieves," *Industrial and Engineering Chemistry Research*. pp. 3237–3261, 2001.
- [5] S. A. Bagshaw, E. Prouzet, and T. J. Pinnavaia, "Templating of mesoporous molecular sieves by nonionic polyethylene oxide surfactants," *Science (80-. )*, vol. 269, no. 5228, pp. 1242–1244, 1995.
- [6] G. S. Attard, J. C. Glyde, and C. G. Göltner, "Liquid-crystalline phases as templates for the synthesis of mesoporous silica," *Nature*, vol. 378, pp. 366–368, 1995.
- [7] W. Yue and W. Zhou, "Crystalline mesoporous metal oxide," *Progress in Natural Science*. pp. 1329–1338, 2008.
- [8] Y. Ren, Z. Ma, and P. G. Bruce, "Ordered mesoporous metal oxides: Synthesis and applications," *Chemical Society Reviews*. pp. 4909–4927, 2012.
- [9] P. Yang, D. Zhao, D. I. Margolese, B. F. Chmelka, and G. D. Stucky, "Generalized syntheses of large-pore mesoporous metal oxides with semicrystalline frameworks," *Nature*, vol. 396, pp. 152–155, 1998.
- [10] P. Yang, D. Zhao, D. I. Margolese, B. F. Chmelka, and G. D. Stucky, "Block copolymer templating syntheses of mesoporous metal oxides with large ordering lengths and semicrystalline framework," *Chem. Mater.*, vol. 11, no. 10, pp. 2813–2826, 1999.
- [11] L. Guo, H. Arafune, and N. Teramae, "Synthesis of mesoporous metal oxide by the thermal decomposition of oxalate precursor," *Langmuir*, vol. 29, no. 13, pp. 4404–4412, 2013.
- [12] Q. Huo *et al.*, "Generalized synthesis of periodic surfactant/inorganic composite materials," *Nature*, vol. 368, pp. 317–321, 1994.
- [13] A. DM, A. Nakahira, and Y. JY, "Ligand-assisted liquid crystal templating in mesoporous niobium oxide molecular sieves," *Inorg. Chem.*, vol. 35, no. 11, pp. 3126–3136, 1996.
- [14] D. M. Antonelli and J. Y. Ying, "Synthesis of Hexagonally Packed

- Mesoporous TiO<sub>2</sub> by a Modified Sol–Gel Method,” *Angew. Chemie Int. Ed. English*, vol. 34, no. 18, pp. 2014–2017, 1995.
- [15] M. S. Wong, D. M. Antonelli, and J. Y. Ying, “Synthesis and characterization of phosphated mesoporous zirconium oxide,” *Nanostructured Mater.*, vol. 9, no. 1–8, pp. 165–168, 1997.
- [16] D. M. Antonelli, “Synthesis of macro-mesoporous niobium oxide molecular sieves by a ligand-assisted vesicle templating strategy,” *Microporous Mesoporous Mater.*, vol. 33, no. 1–3, pp. 209–214, 1999.
- [17] C. J. Brinker, Y. Lu, A. Sellinger, and H. Fan, “Evaporation-induced self-assembly: Nanostructures made easy,” *Adv. Mater.*, vol. 11, no. 7, pp. 579–585, 1999.
- [18] Y. Deng *et al.*, “Ordered mesoporous silicas and carbons with large accessible pores templated from amphiphilic diblock copolymer poly(ethylene oxide)-b-polystyrene,” *J. Am. Chem. Soc.*, vol. 129, no. 6, pp. 1690–1697, 2007.
- [19] Y. Lu, H. Fan, A. Stump, T. L. Ward, T. Rieker, and C. J. Brinker, “Aerosol-assisted self-assembly of mesostructured spherical nanoparticles,” *Nature*, vol. 398, pp. 223–226, 1999.
- [20] D. Grosso, A. R. Balkenende, P. A. Albouy, A. Ayral, H. Amenitsch, and F. Babonneau, “Two-dimensional hexagonal mesoporous silica thin films prepared from block copolymers: Detailed characterization and formation mechanism,” *Chem. Mater.*, vol. 13, no. 5, pp. 1848–1856, 2001.
- [21] N. A. Melosh *et al.*, “Molecular and mesoscopic structures of transparent block copolymer-silica monoliths,” *Macromolecules*, vol. 32, no. 13, pp. 4332–4342, 1999.
- [22] N. A. Melosh, P. Davidson, and B. F. Chmelka, “Monolithic mesophase silica with large ordering domains,” *J. Am. Chem. Soc.*, vol. 122, no. 5, pp. 823–829, 2000.
- [23] M. Mamak, N. Coombs, and G. Ozin, “Self-assembling solid oxide fuel cell materials: Mesoporous yttria-zirconia and metal-yttria-zirconia solid solutions,” *J. Am. Chem. Soc.*, vol. 122, no. 37, pp. 8932–8939, 2000.
- [24] B. Sun, J. Horvat, H. S. Kim, W. S. Kim, J. Ahn, and G. Wang, “Synthesis of mesoporous  $\alpha$ -Fe<sub>2</sub>O<sub>3</sub> nanostructures for highly sensitive gas sensors and high capacity anode materials in lithium ion batteries,” *J. Phys. Chem. C*, vol. 114, no. 44, pp. 18753–18761, 2010.
- [25] H. Yang and D. Zhao, “Synthesis of replica mesostructures by the nanocasting strategy,” *Journal of Materials Chemistry*, pp. 1217–1231, 2005.
- [26] A. H. Lu and F. Schüth, “Nanocasting: A versatile strategy for creating nanostructured porous materials,” *Advanced Materials*, pp. 1793–1805, 2006.
- [27] R. Ryoo, S. H. Joo, and S. Jun, “Synthesis of Highly Ordered Carbon Molecular Sieves via Template-Mediated Structural Transformation,” *J. Phys. Chem. B*, vol. 103, no. 37, pp. 7743–7746, 1999.

- [28] Z. Yang, Y. Zhang, and Z. Schnepf, "Soft and hard templating of graphitic carbon nitride," *Journal of Materials Chemistry A*, pp. 14081–14092, 2015.
- [29] W. C. Yoo and J. K. Lee, "Field-dependent growth patterns of metals electroplated in nanoporous alumina membranes," *Adv. Mater.*, vol. 16, no. 13, pp. 1097–1101, 2004.
- [30] S. H. Joo, S. Jun, and R. Ryoo, "Synthesis of ordered mesoporous carbon molecular sieves CMK-1," *Microporous Mesoporous Mater.*, vol. 44–45, pp. 153–158, 2001.
- [31] S. Che *et al.*, "Direct observation of 3D mesoporous structure by scanning electron microscopy (SEM): SBA-15 silica and CMK-5 carbon," *Angew. Chemie - Int. Ed.*, vol. 42, no. 19, pp. 2182–2185, 2003.
- [32] K. Zhu, B. Yue, W. Zhou, and H. He, "Preparation of three-dimensional chromium oxide porous single crystals templated by SBA-15," *Chem. Commun.*, vol. 8, no. 1, pp. 98–99, 2003.
- [33] B. Yue *et al.*, "Preparation and characterization of three-dimensional mesoporous crystals of tungsten oxide," *Chem. Phys. Lett.*, vol. 407, no. 1, pp. 83–86, 2005.
- [34] W. C. Li, A. H. Lu, C. Weidenthaler, and F. Schüth, "Hard-templating pathway to create mesoporous magnesium oxide," *Chem. Mater.*, vol. 16, no. 26, pp. 5676–5681, 2004.
- [35] F. Hao, Z. Zhang, and L. Yin, "Co<sub>3</sub>O<sub>4</sub>/carbon aerogel hybrids as anode materials for lithium-ion batteries with enhanced electrochemical properties," *ACS Appl. Mater. Interfaces*, vol. 5, no. 17, pp. 8337–8344, 2013.
- [36] G. R. Li, Z. P. Feng, Y. N. Ou, D. Wu, R. Fu, and Y. X. Tong, "Mesoporous MnO<sub>2</sub>/Carbon aerogel composites as promising electrode materials for high-performance supercapacitors," *Langmuir*, vol. 26, no. 4, pp. 2209–2213, 2010.
- [37] H. Kim and J. Cho, "Hard templating synthesis of mesoporous and nanowire SnO<sub>2</sub> lithium battery anode materials," *J. Mater. Chem.*, vol. 18, pp. 771–775, 2008.
- [38] A. Ruplecker, F. Kleitz, E. L. Salabas, and F. Schüth, "Hard templating pathways for the synthesis of nanostructured porous Co<sub>3</sub>O<sub>4</sub>," *Chem. Mater.*, vol. 19, no. 3, pp. 485–496, 2007.
- [39] K. E. Shopsowitz, A. Stahl, W. Y. Hamad, and M. J. MacLachlan, "Hard templating of nanocrystalline titanium dioxide with chiral nematic ordering," *Angew. Chemie - Int. Ed.*, vol. 51, no. 28, pp. 6886–6890, 2012.
- [40] I. Dierking, *Textures of Liquid Crystals*. 2004.
- [41] S. Chandrasekhar and G. S. Ranganath, "Discotic liquid crystals," *Reports Prog. Phys.*, vol. 116, no. 3, pp. 1139–1241, 1990.
- [42] Q. Liang, P. Liu, C. Liu, X. Jian, D. Hong, and Y. Li, "Synthesis and properties of lyotropic liquid crystalline copolyamides containing

- phthalazinone moiety and ether linkages,” *Polymer (Guildf.)*, vol. 46, no. 16, pp. 6258–6265, 2005.
- [43] M. U. Araos and G. G. Warr, “Self-assembly of nonionic surfactants into lyotropic liquid crystals in ethylammonium nitrate, a room-temperature ionic liquid,” *J. Phys. Chem. B*, vol. 109, no. 30, pp. 14275–14277, 2005.
- [44] C. Seguin, J. Eastoe, R. Clapperton, R. K. Heenan, and I. Grillo, “Alternative non-aqueous water-miscible solvents for surfactants,” *Colloids Surfaces A Physicochem. Eng. Asp.*, vol. 282–283, pp. 134–142, 2006.
- [45] G. S. Attard, P. N. Bartlett, N. R. B. Coleman, J. M. Elliott, J. R. Owen, and J. H. Wang, “Mesoporous platinum films from lyotropic liquid crystalline phases,” *Science (80-. )*, vol. 278, no. 5339, pp. 838–840, 1997.
- [46] A. H. Whitehead, J. M. Elliott, J. R. Owen, and G. S. Attard, “Electrodeposition of mesoporous tin films,” *Chem. Commun.*, pp. 331–332, 1999.
- [47] P. V. Braun, P. Osenar, and S. I. Stupp, “Semiconducting superlattices templated by molecular assemblies,” *Nature*, vol. 380, pp. 325–328, 1996.
- [48] P. V. Braun, P. Osenar, V. Tohver, S. B. Kennedy, and S. I. Stupp, “Nanostructure templating in inorganic solids with organic lyotropic liquid crystals,” *J. Am. Chem. Soc.*, vol. 121, no. 32, pp. 7302–7309, 1999.
- [49] Ö. Çelik and Ö. Dag, “A New Lyotropic Liquid Crystalline System: Oligo(ethylene oxide) Surfactants with  $[M(H_2O)_n]X_m$  Transition Metal Complexes,” *Angew. Chemie Int. Ed.*, vol. 40, no. 20, pp. 3799–3803, 2002.
- [50] A. Faik Demirörs, B. E. Eser, and Ö. Dag, “Liquid crystalline mesophases of pluronics (L64, P65, and P123) and transition metal nitrate salts ( $[M(H_2O)_6](NO_3)_2$ ),” *Langmuir*, vol. 21, no. 9, pp. 4156–4162, 2005.
- [51] Ö. Dag, S. Alayoğlu, and I. Uysal, “Effects of ions on the liquid crystalline mesophase of transition-metal salt: Surfactant (CnEom),” *J. Phys. Chem. B*, vol. 108, no. 24, pp. 8439–8446, 2004.
- [52] Ö. Dag, O. Samarskaya, C. Tura, A. Günay, and Ö. Çelik, “Spectroscopic Investigation of Nitrate–Metal and Metal–Surfactant Interactions in the Solid  $AgNO_3C_{12}EO_{10}$  and Liquid-Crystalline  $[M(H_2O)_n](NO_3)_2/C_{12}EO_{10}$  Systems,” *Langmuir*, vol. 19, no. 9, pp. 3671–3676, 2003.
- [53] C. Albayrak, A. M. Soylu, and Ö. Dag, “The role of charged surfactants in the thermal and structural properties of lyotropic liquid crystalline mesophases of  $[Zn(H_2O)_6](NO_3)_2$ -CnEom-H<sub>2</sub>O,” *J. Colloid Interface Sci.*, vol. 341, no. 1, pp. 109–116, 2010.
- [54] C. Karakaya, Y. Türker, C. Albayrak, and Ö. Dag, “Assembly of molten transition metal salt-surfactant in a confined space for the synthesis of mesoporous metal oxide-rich metal oxide-silica thin films,” *Chem. Mater.*, vol. 23, no. 12, pp. 3062–3071, 2011.
- [55] C. Karakaya, Y. Türker, and Ö. Dag, “Molten-salt-assisted self-assembly

- (MASA)-synthesis of mesoporous metal titanate-titania, metal sulfide-titania, and metal selenide-titania thin films,” *Adv. Funct. Mater.*, vol. 23, no. 32, pp. 4002–4010, 2013.
- [56] C. Avci *et al.*, “Molten salt assisted self assembly (MASA): Synthesis of mesoporous metal titanate ( $\text{CoTiO}_3$ ,  $\text{MnTiO}_3$ , and  $\text{Li}_4\text{Ti}_5\text{O}_{12}$ ) thin films and monoliths,” *Chem. Mater.*, vol. 26, no. 20, pp. 6050–6057, 2014.
- [57] G. Saat, F. M. Balci, E. P. Alsaç, F. Karadas, and Ö. Dag, “Molten Salt Assisted Self-Assembly: Synthesis of Mesoporous  $\text{LiCoO}_2$  and  $\text{LiMn}_2\text{O}_4$  Thin Films and Investigation of Electrocatalytic Water Oxidation Performance of Lithium Cobaltate,” *Small*, vol. 14, no. 1, pp. 1701913-1701913–11, 2018.
- [58] Q. Zhang, E. Uchaker, S. L. Candelaria, and G. Cao, “Nanomaterials for energy conversion and storage,” *Chem. Soc. Rev.*, vol. 42, pp. 3127–3171, 2013.
- [59] D. Ganguly *et al.*, “All-amorphous CNT- $\text{MnO}_2$  nanoflaky hybrid for improved supercapacitor applications,” *J. Electroanal. Chem.*, vol. 778, pp. 12–22, 2016.
- [60] Y. Wang, J. Zhu, X. Yang, L. Lu, and X. Wang, “Preparation of NiO nanoparticles and their catalytic activity in the thermal decomposition of ammonium perchlorate,” *Thermochim. Acta*, vol. 437, no. 1–2, pp. 106–109, 2005.
- [61] F. F. Ferreira and E. Avendaño, “Reversible electronic charge transfer between Au nanoparticles and electrochromic NiO matrices upon electrochemical cycling,” *J. Phys. Chem. C*, vol. 111, no. 44, pp. 16608–16612, 2007.
- [62] M. Jlassi, I. Sta, M. Hajji, and H. Ezzaouia, “Synthesis and characterization of nickel oxide thin films deposited on glass substrates using spray pyrolysis,” *Appl. Surf. Sci.*, vol. 308, pp. 199–205, 2014.
- [63] P. Jeevanandam and V. R. R. Pulimi, “Synthesis of nanocrystalline NiO by sol-gel and homogeneous precipitation methods,” *Indian J. Chem. - Sect. A Inorganic, Phys. Theor. Anal. Chem.*, vol. 51A, pp. 586–590, 2012.
- [64] A. Rahdar, M. Aliahmad, and Y. Azizi, “Synthesis of Cu Doped NiO Nanoparticles by Chemical Method,” *J. Nanostructures*, vol. 4, pp. 145–152, 2014.
- [65] C. Li and S. Liu, “Preparation and characterization of  $\text{Ni}(\text{OH})_2$  and nio mesoporous nanosheets,” *J. Nanomater.*, vol. 2012, pp. 1–6, 2012.
- [66] L. Wang, Y. Hao, Y. Zhao, Q. Lai, and X. Xu, “Hydrothermal synthesis and electrochemical performance of NiO microspheres with different nanoscale building blocks,” *J. Solid State Chem.*, vol. 183, no. 11, pp. 2576–2581, 2010.
- [67] K. Byrappa and T. Adschiri, “Hydrothermal technology for nanotechnology,” *Progress in Crystal Growth and Characterization of Materials*. 2007.
- [68] S. K. Meher, P. Justin, and G. R. Rao, “Microwave-mediated synthesis for

- improved morphology and pseudocapacitance performance of nickel oxide,” *ACS Appl. Mater. Interfaces*, vol. 3, no. 6, pp. 2063–2073, 2011.
- [69] A. Venter and J. R. Botha, “Optical and electrical properties of NiO for possible dielectric applications,” *S. Afr. J. Sci.*, vol. 107, no. 1–2, pp. 1–6, 2011.
- [70] H. Yang, Q. Tao, X. Zhang, A. Tang, and J. Ouyang, “Solid-state synthesis and electrochemical property of SnO<sub>2</sub>/NiO nanomaterials,” *J. Alloys Compd.*, vol. 459, no. 1–2, pp. 98–102, 2008.
- [71] R. Eder, “Electronic structure of NiO: Antiferromagnetic transition and photoelectron spectra in the ordered phase,” *Phys. Rev. B - Condens. Matter Mater. Phys.*, vol. 91, no. 24, pp. 1–20, 2015.
- [72] S. A. Mahmoud, A. Shereen, and M. A. Tarawnh, “Structural and Optical Dispersion Characterisation of Sprayed Nickel Oxide Thin Films,” *J. Mod. Phys.*, vol. 2, pp. 1178–1186, 2011.
- [73] N. Aristov and A. Habekost, “Cyclic Voltammetry - A Versatile Electrochemical Method Investigating Electron Transfer Processes,” *World J. Chem. Educ. Vol. 3, 2015, Pages 115-119*, vol. 3, no. 5, pp. 115–119, 2015.
- [74] V. S. R. Channu, R. Holze, and B. Rambabu, “Synthesis and characterization of NiO nanoparticles for electrochemical applications,” *Colloids Surfaces A Physicochem. Eng. Asp.*, vol. 414, pp. 204–208, 2012.
- [75] K. Wang, L. Li, and T. Zhang, “Synthesis of nickel hydroxide and its electrochemical performances,” *Int. J. Electrochem. Sci.*, vol. 8, pp. 6252–6257, 2013.
- [76] W. Xing, F. Li, Z. F. Yan, and G. Q. Lu, “Synthesis and electrochemical properties of mesoporous nickel oxide,” *J. Power Sources*, vol. 134, no. 2, pp. 324–330, 2004.
- [77] X. Xu, J. Liang, H. Zhou, S. Ding, and D. Yu, “The preparation of hierarchical tubular structures comprised of NiO nanosheets with enhanced supercapacitive performance,” *RSC Adv.*, vol. 4, pp. 3181–3187, 2014.
- [78] M. P. Browne, H. Nolan, N. C. Berner, G. S. Duesberg, P. E. Colavita, and M. E. G. Lyons, “Electrochromic nickel oxide films for smart window applications,” *Int. J. Electrochem. Sci.*, vol. 11, 2016.
- [79] S. Pilban Jahromi, N. M. Huang, A. Kamalianfar, H. N. Lim, M. R. Muhamad, and R. Yousefi, “Facile synthesis of porous-structured nickel oxide thin film by pulsed laser deposition,” *J. Nanomater.*, vol. 2012, pp. 1–4, 2012.
- [80] S. Zhang *et al.*, “High-performance electrochromic device based on nanocellulose/polyaniline and nanocellulose/poly(3,4-ethylenedioxythiophene) composite thin films,” *Opt. Eng.*, vol. 56, no. 7, p. 077101, 2017.
- [81] M. K. Carpenter, R. S. Conell, and D. A. Corrigan, “The electrochromic properties of hydrous nickel oxide,” *Sol. Energy Mater.*, vol. 16, no. 4, pp.

333–346, 1987.

- [82] J. L. Garcia-Miquel *et al.*, “Nickel oxide sol-gel films from nickel diacetate for electrochromic applications,” *Thin Solid Films*, vol. 424, no. 2, pp. 165–170, 2003.
- [83] M. Z. Sialvi *et al.*, “Electrochromic and colorimetric properties of nickel(II) oxide thin films prepared by aerosol-assisted chemical vapor deposition,” *ACS Appl. Mater. Interfaces*, vol. 5, no. 12, pp. 5675–5682, 2013.
- [84] R. T. Wen, G. A. Niklasson, and C. G. Granqvist, “Electrochromic nickel oxide films and their compatibility with potassium hydroxide and lithium perchlorate in propylene carbonate: Optical, electrochemical and stress-related properties,” *Thin Solid Films*, vol. 565, pp. 128–135, 2014.
- [85] Y. Li, X. Han, T. Yi, Y. He, and X. Li, “Review and prospect of NiCo<sub>2</sub>O<sub>4</sub> - based composite materials for supercapacitor electrodes,” *Journal of Energy Chemistry*. pp. 17276–17283, 2019.
- [86] Y. Q. Wu, X. Y. Chen, P. T. Ji, and Q. Q. Zhou, “Sol-gel approach for controllable synthesis and electrochemical properties of NiCo<sub>2</sub>O<sub>4</sub> crystals as electrode materials for application in supercapacitors,” *Electrochim. Acta*, vol. 56, no. 22, pp. 7517–7522, 2011.
- [87] C. Yuan *et al.*, “Template-engaged synthesis of uniform mesoporous hollow NiCo<sub>2</sub>O<sub>4</sub> sub-microspheres towards high-performance electrochemical capacitors,” *RSC Adv.*, vol. 3, pp. 18573–18578, 2013.
- [88] J. Wu *et al.*, “Ultrathin NiCo<sub>2</sub> O<sub>4</sub> nanosheets grown on three-dimensional interwoven nitrogen-doped carbon nanotubes as binder-free electrodes for high-performance supercapacitors,” *J. Mater. Chem. A*, vol. 3, pp. 15331–15338, 2015.
- [89] J. Wang *et al.*, “Facile synthesis of three-dimensional NiCo<sub>2</sub>O<sub>4</sub> with different morphology for supercapacitors,” *RSC Adv.*, vol. 6, pp. 70077–70084, 2016.
- [90] T. Y. Wei, C. H. Chen, H. C. Chien, S. Y. Lu, and C. C. Hu, “A cost-effective supercapacitor material of ultrahigh specific capacitances: spinel nickel cobaltite aerogels from an epoxide-driven sol-gel process,” *Adv. Mater.*, vol. 22, no. 3, pp. 347–351, 2010.
- [91] M.-C. Liu *et al.*, “A Sol-Gel Process for the Synthesis of NiCo<sub>2</sub>O<sub>4</sub> Having Improved Specific Capacitance and Cycle Stability for Electrochemical Capacitors,” *J. Electrochem. Soc.*, vol. 159, no. 8, pp. 1262–1266, 2012.
- [92] W. Xiong *et al.*, “Composite of macroporous carbon with honeycomb-like structure from mollusc shell and NiCo<sub>2</sub>O<sub>4</sub> nanowires for high-performance supercapacitor,” *ACS Appl. Mater. Interfaces*, vol. 6, no. 21, pp. 19416–19423, 2014.
- [93] L. Shen, L. Yu, X. Y. Yu, X. Zhang, and X. W. D. Lou, “Self-templated formation of uniform NiCo<sub>2</sub>O<sub>4</sub> hollow spheres with complex interior structures for lithium-Ion batteries and supercapacitors,” *Angew. Chemie - Int.*

*Ed.*, vol. 54, no. 6, pp. 1868–1872, 2015.

- [94] L. Li *et al.*, “Electrospun porous NiCo<sub>2</sub>O<sub>4</sub> nanotubes as advanced electrodes for electrochemical capacitors,” *Chem. - A Eur. J.*, vol. 19, no. 19, pp. 5892–5898, 2013.
- [95] Y. Yang, D. Zeng, S. Yang, L. Gu, B. Liu, and S. Hao, “Nickel cobaltite nanosheets coated on metal-organic framework-derived mesoporous carbon nanofibers for high-performance pseudocapacitors,” *J. Colloid Interface Sci.*, vol. 534, pp. 312–321, 2019.
- [96] C. Zhang, L. Deng, P. Zhang, X. Ren, Y. Li, and T. He, “Mesoporous NiCo<sub>2</sub>O<sub>4</sub> networks with enhanced performance as counter electrodes for dye-sensitized solar cells,” *Dalt. Trans.*, vol. 46, pp. 4403–4411, 2017.
- [97] H. Shi and G. Zhao, “Water Oxidation on Spinel NiCo<sub>2</sub>O<sub>4</sub> Nanoneedles Anode: Microstructures, Specific Surface Character, and the Enhanced Electrocatalytic Performance,” *J. Phys. Chem. C*, vol. 118, no. 45, pp. 25939–25946, 2014.
- [98] Y. Li *et al.*, “Closed Pore Structured NiCo<sub>2</sub>O<sub>4</sub>-Coated Nickel Foams for Stable and Effective Oil/Water Separation,” *ACS Appl. Mater. Interfaces*, vol. 9, no. 34, pp. 29177–29184, 2017.
- [99] J. Li, S. Xiong, Y. Liu, Z. Ju, and Y. Qian, “High electrochemical performance of monodisperse NiCo<sub>2</sub>O<sub>4</sub> mesoporous microspheres as an anode material for Li-ion batteries,” *ACS Appl. Mater. Interfaces*, vol. 5, no. 3, pp. 981–988, 2013.
- [100] M. U. Anu Prathap and R. Srivastava, “Synthesis of NiCo<sub>2</sub>O<sub>4</sub> and its application in the electrocatalytic oxidation of methanol,” *Nano Energy*, vol. 2, no. 5, pp. 1046–1053, 2013.
- [101] M. Alagar, T. Theivasanthi, and A. Kubera Raja, “Chemical synthesis of nano-sized particles of lead oxide and their characterization studies,” *J. Appl. Sci.*, vol. 12, no. 4, pp. 398–401, 2012.
- [102] Y. E. Chen, Z. N. Yu, Y. G. Chen, L. Q. Luo, and X. Wang, “Preparation of NiO nanoparticles as supercapacitor electrode by precipitation using carbon black powder,” in *ICMREE2011 - Proceedings 2011 International Conference on Materials for Renewable Energy and Environment*, 2011, pp. 640–643.
- [103] H. Wang and M. Yoshio, “Graphite, a suitable positive electrode material for high-energy electrochemical capacitors,” *Electrochem. commun.*, vol. 8, no. 9, pp. 1481–1486, 2006.
- [104] D. S. Hall, D. J. Lockwood, C. Bock, and B. R. MacDougall, “Nickel hydroxides and related materials: A review of their structures, synthesis and properties,” *Proceedings of the Royal Society A: Mathematical, Physical and Engineering Sciences*. pp. 1–65, 2015.